

Numerical simulations of an exceptional dust event in the Eastern Mediterranean including the mineral dust radiative feedback

**Numerische Simulation eines außergewöhnlichen Staubereignisses im
östlichen Mittelmeerraum unter Berücksichtigung der
Mineralstaub-Strahlungswechselwirkung**

Masterarbeit im Fach Meteorologie
von

Philipp Gasch

September 2016



INSTITUT FÜR METEOROLOGIE UND KLIMAFORSCHUNG
KARLSRUHER INSTITUT FÜR TECHNOLOGIE (KIT)

Referent:

Prof. Dr. Christoph Kottmeier

Korreferent:

Prof. Dr. Peter Knippertz

Zusammenfassung

Im September 2015 ereignete sich eines der schwersten jemals beobachteten Staubereignisse im Nahen Osten. Das Auftreten des Staubsturms im September und die Transportrichtung des Staubes von Osten in den östlichen Mittelmeerraum sind sehr ungewöhnlich. Erstaunlicherweise wurde der Staubsturm von keinem der modernen Wettervorhersagemodelle, welche in der Lage sind Staubprozesse zu simulieren, korrekt vorhergesagt. Die vorliegende Studie erklärt das Scheitern der Modelle und präsentiert die erste Simulation des Ereignisses mit konvektionserlaubender Auflösung und unter Berücksichtigung der Mineralstaub-Strahlungswechselwirkung mit ICON-ART (ICOSahedrisches Nichthydrostatisches Modell - Aerosols and Reactive Trace gases). Hierzu wurde im Zuge dieser Arbeit die Mineralstaub-Strahlungswechselwirkung in ICON-ART implementiert. Dabei wird eine neue, größenabhängige Parametrisierung der optischen Eigenschaften von Mineralstaubpartikeln eingeführt. Ein Vergleich der Ergebnisse der konvektionserlaubenden Simulation mit Satellitenbeobachtungen zeigt, dass ICON-ART eine deutliche Verbesserung der bisher existierenden Vorhersagen erlaubt. Sowohl die horizontale und vertikale Struktur als auch die zeitliche Entwicklung der Staubverteilung werden in ICON-ART realistisch erfasst und Werte der optischen Dicke von mehr als 6 werden über Syrien erreicht. Daher können alle für Staubemission und Staubtransport in den östlichen Mittelmeerraum verantwortlichen Prozesse identifiziert und eingehend analysiert werden. Dabei zeigt sich ein systematischer Effekt der Mineralstaub-Strahlungswechselwirkung auf konvektive Kaltluftausflüsse.

Die Simulationsergebnisse erlauben eine eingehende Analyse des Einflusses der synoptischen Situation, der treibenden meteorologischen Systeme und der Mineralstaub-Strahlungswechselwirkung auf das Ereignis. Die synoptische Lage wird als sogenannte *active Red Sea Trough*-Situation identifiziert. Diese tritt außergewöhnlich früh im Jahr auf und ist damit für den besonderen Charakter des Staubereignisses verantwortlich. Die Situation ist bestimmt durch einen ausgedehnten niedertroposphärischen Trog, welcher sich mit einer östlichen Achse vom Roten Meer nordwärts erstreckt. Dieser Trog advehiert feuchte und warme Luftmassen vom Persischen Golf entlang seiner östlichen Flanke. Zusätzlich existiert ein obertroposphärischer Trog, welcher sich über Mesopotamien südwärts erstreckt. In Verbindung mit orographischen Effekten in der Region wird somit die Entstehung mehrerer meso-skaliger konvektiver Systeme im Norden und Osten von Mesopotamien ermöglicht. Des weiteren wird die Entwicklung eines ausgeprägten Hitzetiefs über Syrien unterstützt. Die meso-skaligen konvektiven Systeme produzieren mehrere aufeinanderfolgende Kaltluftausflüsse, welche in der Folge die zyklonale Strömung um das Hitzetief beeinflussen und verstärken. Außerdem erfolgt eine Interaktion der Strömung mit der landeinwärts strömenden

Seewind Zirkulation des östlichen Mittelmeers. Alle genannten meteorologischen System sind mit signifikanten Staubemissionen verbunden. Der Transport der Staubfahne erfolgt entlang der westlichen Flanke des Roten Meer Trog in Richtung des östlichen Mittelmeerraumes. Dabei wechselwirkt die Strömung mit der Orographie des Toten Meer Grabenbruchs, was zur verbreiteten Entstehung von super-kritischen Strömungsbedingungen und damit in Verbindung stehenden hydraulischen Sprüngen führt. Die damit verbundenen Staubemissionen sorgen für extreme Staubkonzentrationen im südlichen Teil des östlichen Mittelmeerraumes. Das Strömungsphänomen wird von ICON-ART simuliert, allerdings nicht mit der korrekten Magnitude und Zeitlichkeit wie ein Vergleich mit Stationsmessungen in Israel zeigt. Dies führt zu einer Unterschätzung der Staubkonzentrationen um eine Größenordnung im Modell. Ein Vergleich mit charakteristischen PM10-Stationsmessungen in Israel belegt, dass die mit der Staubfahne in Verbindung stehenden Transport- und Depositionsprozesse dennoch korrekt dargestellt werden.

Der Einfluss der Mineralstaub-Strahlungswechselwirkung zeigt im Modellgebiet außerhalb der Kaltluftausflüsse das zu erwartende Verhalten. Mineralstaub führt tagsüber zu einer Reduktion der solaren Einstrahlung am Boden was zu einer Stabilisierung Grenzschicht führt. Damit verbunden ist eine Reduktion der Staubemissionen. Nachts führt Mineralstaub zu einer Erhöhung langwelliger atmosphärischer Gegenstrahlung und als Resultat einer Erwärmung der bodennahen Luftschichten. Mit der einhergehenden Destabilisierung ist eine Erhöhung der Staubemissionen verbunden. Die neu eingeführte, größenabhängige Parametrisierung der optischen Eigenschaften von Mineralstaubpartikeln verstärkt die Effekte in Quellgebieten systematisch, jedoch mit geringer Magnitude. Die Größenabhängigkeit wirkt sich aufgrund des reduzierten Mediandurchmessers der zwei größten Moden in ICON-ART aus, während die kleinste Mode keinen Einfluss zeigt.

Einen unerwarteten Effekt zeigt die Mineralstaub-Strahlungswechselwirkung im Bereich der konvektiven Kaltluftausflüsse. Obwohl der Strahlungseffekt des Mineralstaubs das gewöhnliche Verhalten aufweist, führt die Berücksichtigung der Strahlungswechselwirkung nachts zu einer stärkeren bodennahe Abkühlung und größeren Staubemissionen. Es wird gezeigt, dass dies im Zusammenhang mit systematisch kräftigeren und schnelleren konvektiven Kaltluftausflüssen im Strahlungswechselwirkungslauf steht.

In der Zusammenfassung stellt diese Studie einen Schritt, hin zu einem besseren Verständnis und einer besseren Vorhersage von schweren und komplexen Staubereignissen, dar. Die Ergebnisse betonen die Notwendigkeit von konvektionserlaubenden Auflösungen bei der Modellierung von Staubereignissen in Verbindung mit organisierter meso-skaliiger Konvektion. Zusätzlich werden neue Erkenntnisse über den Strahlungseffekt von Mineralstaub in Verbindung mit konvektiven Kaltluftausflüssen gewonnen.

Abschließend kann festgestellt werden, dass ICON-ART aufgrund der Möglichkeiten zur nahtlosen Gebietsverfeinerung die Fähigkeit besitzt atmosphärische Prozesse mit hoher Genauigkeit zu modellieren. Dadurch kann ICON-ART das Verständnis für vorher nicht darstellbare Ereignisse in der Atmosphäre fördern, dies gilt insbesondere in Bezug auf Staubstürme und die beteiligten Prozesse.

Contents

1	Introduction	5
2	Mineral dust - a key aerosol	9
2.1	Mineral dust in the environmental system	9
2.2	Modelling mineral dust	12
2.2.1	Dust emission	12
2.2.2	Influence on radiative transfer	13
2.2.3	Dust events caused by convective cold-pool outflows	17
2.3	Mineral dust in the Eastern Mediterranean	21
2.3.1	Mesopotamia	24
2.3.2	The Dead Sea Rift Valley	26
3	Methods and data	29
3.1	The ICON-ART model system	29
3.1.1	ICON	29
3.1.2	The ART module	33
3.2	Model set-up	39
3.3	Observations	41
4	Implementation of the mineral dust radiative effect in ICON-ART	45
4.1	Radiative transfer	45
4.2	Mineral dust radiative effect in ICON-ART	48
4.3	Radiative properties of mineral dust	50
4.3.1	Mie calculations	52
4.3.2	Refractive index	54
4.3.3	Results of Mie calculations	59
5	Simulation of a severe dust event in the Eastern Mediterranean	65
5.1	Synoptic situation	65
5.2	Analysis of the driving atmospheric systems	69
5.2.1	First cold-pool outflow, heat low and Eastern Mediterranean sea-breeze	69
5.2.2	Meso-scale convective system development and cold-pool outflows	74
5.2.3	Mature stage of third cold-pool outflow	78

5.2.4	Aged dust plume in the Eastern Mediterranean	83
5.3	Influence of the mineral dust-radiation interaction	86
5.3.1	Mineral dust night-time radiative effect	86
5.3.2	Mineral dust day-time radiative effect	89
5.3.3	Mineral dust radiative effect on atmospheric stratification	90
5.3.4	Influence of the varying mineral dust median diameter	94
5.4	Long-range transport to Israel	96
5.4.1	Hydraulic jump upstream the Dead Sea Rift Valley	96
5.4.2	Comparison to surface observations	100
6	Conclusions	105
	Appendix	111
	Bibliography	111

1. Introduction

In September 2015 one of the severest dust events on record occurred in the Middle East. Surprisingly, state-of-the-art dust transport models were unable to forecast the event. This study details the reasons for the failure of the models to forecast the dust storm and presents the first simulations of the event with convection permitting resolution. The results allow for an in-depth analysis of the influence of the synoptic situation, the interaction of the driving atmospheric systems and the mineral dust radiative effect on the dust event.

The event developed over the course of three days, it was caused by dust which was uplifted over Syria and Iraq and subsequently transported west towards the Eastern Mediterranean (EM). In figure 1.1 satellite images for the visible part of the electromagnetic spectrum (VIS) from the Moderate Resolution Imaging Spectroradiometer (MODIS) instrument are depicted showing the evolution of the dust storm. Starting from 06 September 2015 high dust concentrations were observed over Syria. On 07 September the full Mesopotamia region and the northern part of the EM was covered by a thick dust layer. The dust plume was transported into the southern EM region during the following night, consequently covering the complete EM on 08 September 2015. The dust plume remained detectable in the region over the course of the next seven days.

The impact of the event on the EM region was severe, with five people reported to have died and hundreds hospitalized. Traffic in the region was severely affected, with air traffic shut down, ports in the Suez canal closed and normal daily activities suspended (NASA Earth Observatory, 2015; The Weather Channel, 2015; Times Of Israel, 2015). The Israeli Meteorological Service reported record dust concentrations of more than 100 times the normal. For the first time in 75 years a dust storm which reached Israel in September lasted longer than one day (Alpert et al., 2016).

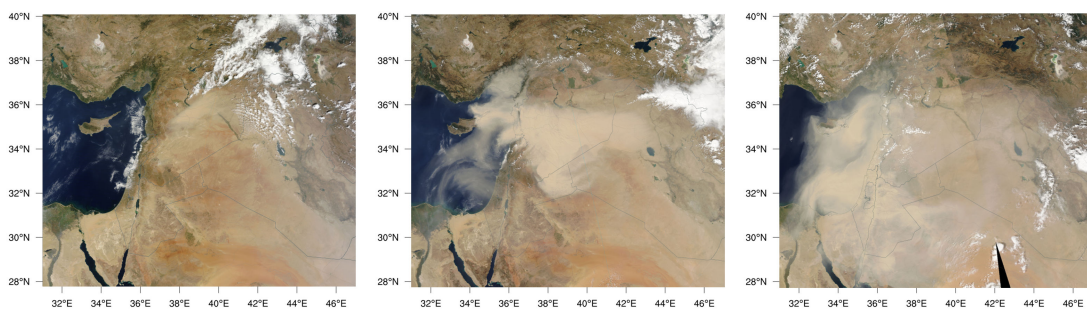


Figure 1.1: MODIS VIS satellite images of the EM region, from left to right for 06, 07 and 08 September 2015 (NASA Worldview, 2016).

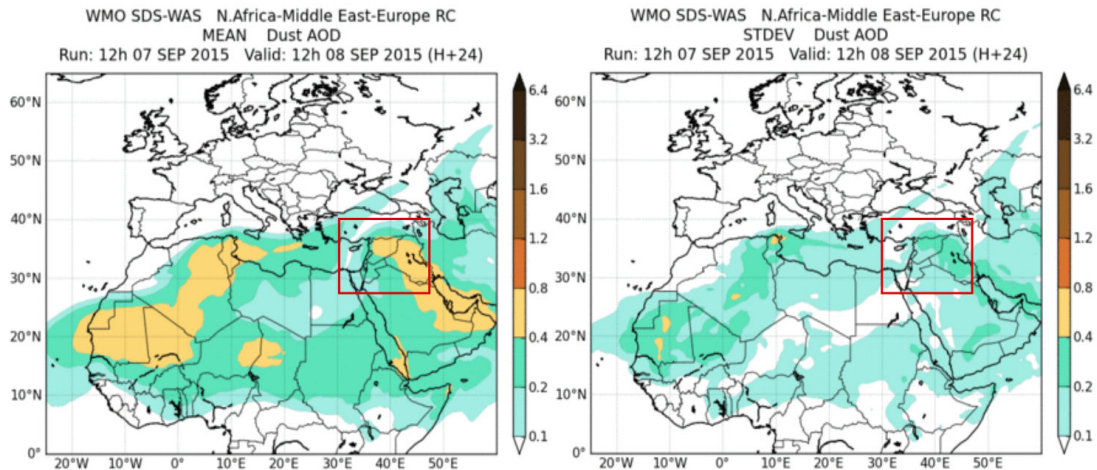


Figure 1.2: Multi-model mean forecast of dust optical depth on the left side and standard deviation of model forecasts on the right side. Forecast from 12 UTC 07 September, valid at 12 UTC 08 September. Image obtained from the WMO SDS-WAS NA-ME-E Regional Center (<http://sds-was.aemet.es>). Marked by a red box is the MODIS VIS satellite image region.

As stated above and also noted by Mamouri et al. (2016), state-of-the-art dust transport models were unable to forecast the dust distribution and concentrations for the event presented here. In figure 1.2 a multi-model mean forecast for the dust optical depth from 9 models (BSC-DREAM8b, MACC, DREAM8-NMME-MACC, NMMB/BSC-Dust, MetUM, NASA GEOS-5, NCEP NGAC, EMA RegCM4 and DREAMABOL) is presented. In the runs started at 12 UTC 07 September none of the models is able to forecast a significant dust concentration in the EM region for 12 UTC 08 September. This is despite the fact that some of the models use data assimilation of satellite aerosol optical depth data. The simulated values of the dust optical depth in the EM are between 0.1 – 0.4 in the multi-model mean with a standard deviation of 0.1 – 0.2. The models producing the highest dust optical depth, over a small part of the Mediterranean Sea close to Syria, are the MACC-ECMWF and DREAMABOL with values between 0.4 – 0.8 (not shown). None of the models is able to produce a dust optical depth higher than 0.4 over Israel. An analysis of the forecasts started at 12 UTC 06 September yields even worse results at 48 hours forecast time.

From EUMETSAT (European Organisation for the Exploitation of Meteorological Satellites) SE-VIRI (Spinning Enhanced Visual and Infrared Imager) satellite observations the development of organized meso-scale convective systems (MCS) which produced cold-pool outflows (CPO) over Mesopotamia is detectable. The CPOs and their interaction with a heat low have been suggested as important drivers for the observed dust emissions by Kerkmann et al. (2015). However, so far a detailed analysis of the driving atmospheric systems and their interaction has not been published. A number of studies have shown that the inability to represent organized meso-scale convection and the related CPOs in models with parametrized convection can lead to a substantial underestimation of dust emissions (Marsham et al., 2011; Heinold et al., 2013). Therefore, the existence of CPOs detectable in satellite observations is suspected as the main reason for the failure of state-of-the-art dust transport models, as all of them operate at resolutions with fully parametrized convection.

In order to overcome this problem the ICON-ART (ICOsahedral Nonhydrostatic - Aerosol and Reactive Trace gases) global modelling system (Zängl et al., 2015) is used in this study. It is capable of local grid refinements, in this study the finest nest has a convection permitting grid spacing of 2.5 km. The ART extension (Rieger et al., 2015) allows for on-line simulation of aerosol processes in ICON. The mineral dust radiation interaction has been implemented in ICON-ART as a part of this work. It allows for consideration of the on-line feedback of mineral dust concentrations on atmospheric parameters, which in turn can influence mineral dust processes again.

Consequently, an in-depth analysis of the influence of the synoptic situation, the interaction of the driving atmospheric systems and the mineral dust radiative effect on the dust event can be presented in this study. Specifically, the research questions addressed are as follows:

1. Is the forecast of the dust event improved by running convection permitting simulations?
2. Which synoptic situation enables this extreme event and how does it relate to its exceptional character?
3. What are the meteorological drivers responsible for pick-up and long-range transport of mineral dust?
4. How does the mineral dust radiative effect influence the dust event in general and the evolution of the CPOs in particular?

The case investigated here presents a complex dust event influenced by a variety of different meteorological systems. An analysis of the synoptic situation is conducted based on studies by Krichak et al. (2012) and Vries et al. (2013), who propose criteria according to which active Red Sea Trough situations can be identified. This work suggests the unusual occurrence of an active Red Sea Trough (RST) situation in early September which enables dust emission over Mesopotamia and subsequent dust transport towards the EM. The RST synoptic situation and dust transport from Syria and Iraq have previously not been linked to severe dust events in the EM and the exceptional character of this event is emphasized by a comparison with climatological studies (Singer et al., 2003; Alpert et al., 2004; Dayan et al., 2008; Kishcha et al., 2016, and references therein).

The contribution and interaction of different atmospheric drivers with respect to dust emission and transport is often observed and can lead to prolonged dust events lasting several days and reaching continental scale (Knippertz, 2014, and references therein). For the event investigated, the most dominant drivers are MCSs producing CPOs. The occurrence of CPOs has been documented for all major dust source regions worldwide (Knippertz, 2014) and they have been identified as important systems contributing to dust emission (Knippertz et al., 2007; Marsham et al., 2011; Heinold et al., 2013). To my knowledge this work presents the first simulation of CPOs at convection permitting resolution in the Middle East. In addition, the interaction of a variety of atmospheric drivers over the course of three days emphasizes a high level of complexity in the generation of dust events.

For atmospheric modelling, the inclusion of the mineral dust radiative feedback is of great importance (Pérez et al., 2006; Bangert et al., 2012; Rémy et al., 2015). Through the modification of the atmospheric radiation budget, dust influences atmospheric processes which in turn feed back on dust processes again. The effects commonly demonstrated are a decrease in incoming short-wave radiation and an increase in down-welling atmospheric long-wave radiation at the surface due to mineral dust (Highwood and Ryder, 2014, and references therein). As a result, surface temperatures are expected to decrease during daytime and increase during night-time because of the mineral dust radiative effect (Tegen et al., 2006). Due to this feedback on atmospheric stratification, a decrease in dust emissions during daytime and an increase in dust emissions during night-time has been documented Pérez et al. (2006); Heinold et al. (2008); Rémy et al. (2015). As a part of this work, the mineral dust radiation interaction has been implemented as a new module in ICON-ART. The implementation of the mineral dust radiative effect in ICON-ART is based on Mie scattering calculations and done in analogy to the aerosol radiation interaction in the COSMO-ART (COnsortium for Small scale MOdelling) model (Stanelle, 2008; Lundgren, 2011). However, the Mie scattering calculations conducted use a new code developed by Bond et al. (2006) and Mätzler (2002). Furthermore a new, size dependent parametrization of the optical parameters is developed.

Combining the above topics of CPOs and their interaction with radiation and dust emission, in a recent study Redl et al. (2016) investigate the influence of the radiative effect of moisture contained in CPOs on boundary layer dynamics. However, a shortcoming of their study is the missing radiative effect of mineral dust, which is often emitted by CPOs in desert regions. This is also a shortcoming in the study of Heinold et al. (2013) who simulate dust emission due to CPOs. Kalenderski and Stenchikov (2016) include and investigate the mineral dust radiative effect in their convection permitting simulation of a CPO. However, they do not publish systematic findings on its feedback on the CPO. To my knowledge this work presents the first study in which the influence of the mineral dust radiative feedback on CPO structure, propagation speed and dust emission is investigated systematically.

In the work presented here, an overview of the importance of mineral dust for the atmospheric system is given in the second chapter. A focus is put on the radiative effect of mineral dust and its feedback on atmospheric state. Furthermore, the modelling of dust emissions in connection with CPOs is discussed and insight into the characteristics of dust events in the EM is provided. In the third chapter the ICON-ART model system is introduced and the model set-up used for this study is detailed. In addition, the observational systems used for validation of model results are briefly presented. The fourth chapter explains the implementation of the mineral dust radiative effect in ICON-ART. In the fifth chapter ICON-ART simulation results for the severe dust event in the EM are discussed and compared to observations. Furthermore, the above stated research questions are investigated in detail. In the conclusions the main achievements and findings of this work are summarized and a short answer to each research question is provided.

2. Mineral dust - a key aerosol

2.1 Mineral dust in the environmental system

Mineral dust aerosol plays an important role for the environment. The transport of mineral dust within the atmosphere has an effect on physical processes, chemical composition and biological systems on various temporal and spatial scales. A schematic overview of the global dust cycle and its interaction and feedback mechanisms with the energy and carbon cycle is given in figure 2.1.

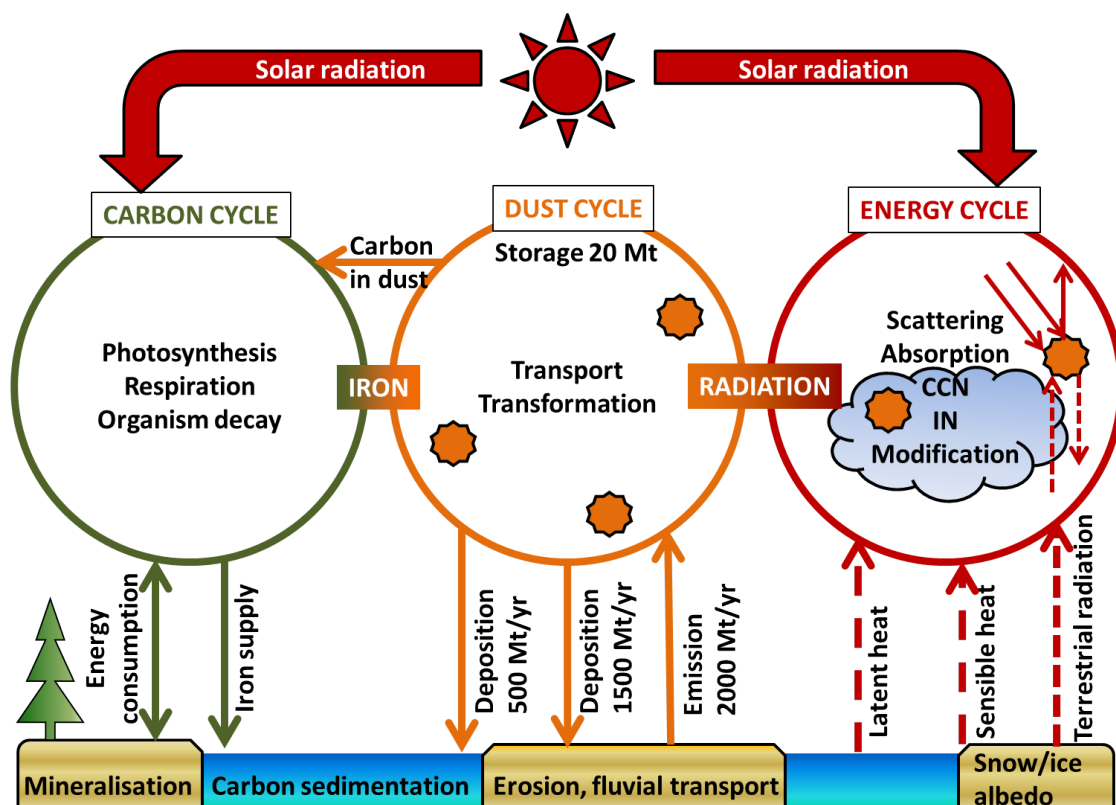


Figure 2.1: A schematic depiction of the carbon, dust and energy cycle. Labelled are feedback processes through which interaction can occur. Based on figures by Shao et al. (2011a).

On a physical level mineral dust influences the energy cycle as it alters the radiative transfer within the atmosphere by absorption and scattering of short- and long-wave radiation. Furthermore min-

eral dust can act as a cloud condensation nuclei (CCN), thereby influencing cloud formation and distribution. Besides this, mineral dust can act as an effective ice nuclei (IN) enabling heterogeneous ice nucleation in cirrus clouds (Hoose and Möhler, 2012), its wide abundance makes it the major aerosol component contributing to this mechanism (Cziczo et al., 2013). In addition, mineral dust can alter the albedo of snow and ice surfaces. On a chemical and biological level mineral dust is closely connected to the carbon cycle as it transports large quantities of iron, which serves as a fertilizer for flora and fauna.

Shao et al. (2011a) provide an overview of the global dust cycle, combining values from multiple studies they estimate the annual global emission of mineral dust to be in the range of 1000 Mt to 5000 Mt with many studies converging at values around 2000 Mt. Approximately 75% of this amount is deposited on continents and 25% in oceans. However, both Shao et al. (2011a) as well as the 5th IPCC assessment report (Boucher et al., 2013) state that uncertainties in the estimates of global dust emission still span a factor of approximately five. In an analysis of MODIS satellite data Ginoux et al. (2012) attribute 20 – 25% of dust emissions to be of anthropogenic origin, an important factor being mineral dust emissions due to human land use change and ephemeral water bodies.

The main global dust source region is the Sahara, therein especially the Bodele depression as well as a larger area in the western Sahara. The Sahara has an estimated contribution to the annual global dust budget of 400 Mt to 2200 Mt (Huneeus et al., 2011), representing about 55% of global emissions (Ginoux et al., 2012). Due to the great extent of the region as well as diverse geographical and meteorological conditions a variety of atmospheric systems are of relevance to dust mobilization processes. Among them are Saharan heat lows, African easterly waves, cyclones, convective cold-pool outflows, nocturnal low level boundary layer jets and dry convective mixing (Knippertz et al., 2009). A number of field experiments have been conducted in this region to study dust related processes, among them the Bodele Dust Experiment (BoDEx) (Washington et al., 2006) and the Saharan Mineral Dust Experiment (SAMUM) (Heintzenberg, 2009) which are referred to frequently for the theoretical background throughout this work.

The second most important global dust source regions are the Asian deserts in Mongolia and China (Shao et al., 2011a). In this area dust emission crucially depends on the surface temperature, as the ground is frozen frequently due to the high altitude of the deserts. Australia represents the most important source for dust in the southern hemisphere, in this region anthropogenic degradation of soil crust due to land-use change over the last 200 years is assumed to have had an important influence. Dust emissions in Australia peak during El Niño years when wind erosion is most active (Ginoux et al., 2012).

When looking at specific events instead of annual global averages other regions can show high dust emissions as well. Important dust source regions for this study are situated in the Middle East, namely the Tigris-Euphrates alluvial plain in Iraq, regions in north-western Syria and the Dead Sea Rift Valley. Further insight into Eastern Mediterranean dust emission characteristics is given in section 2.3.

The wide range of spatial and temporal scales on which mineral dust influences environmental processes in general and atmospheric processes in particular lead to a variety of effects which

have been investigated, a few of which are highlighted in the following. Naturally the separation of scales can not be held up strictly for all effects as constant changes on short term or local scales lead to changes on long term or global scales and vice versa. Therefore this short compilation serves descriptive purposes to demonstrate the multitude of effects for which mineral dust is responsible due to its interaction with the energy and carbon cycle, which in turn feed back on the dust cycle again.

On a global and long-term scale the amount of mineral dust suspended in the atmosphere influences climatic conditions. This occurs by means of different mechanisms, first of all through the direct and indirect radiative effect (Boucher et al., 2013). Second mineral dust can alter global CO₂ concentrations and related processes through its coupling to the carbon-cycle by means of iron fertilization of the ocean (Martínez-García et al., 2011). Through its link with biological systems mineral dust regulates ocean productivity in High-Nitrate and Low Chlorophyll limited oceans which influences ocean-atmosphere CO₂ exchange.

On a global, short term scale three examples show that strong mineral dust outbreaks can have severe effects even in distant regions. In Europe, large Saharan dust outbreaks cause reductions in visibility, changes in radiation and cloud cover and by that have a non-negligible impact on energy production, especially photo-voltaic, and air traffic. For the western Atlantic, mineral dust outbreaks from the Sahara are linked to tropical cyclone activity. Again, through its interaction with radiation and subsequent change of the vertical temperature profile, mineral dust can alter atmospheric stability which is a crucial precondition for the formation of tropical cyclones west of Africa. As Dunion and Velden (2004) and Evan et al. (2006) demonstrate, a robust link between dust transport over the Atlantic and cyclone activity exists although the direct causal relationship is yet to be established due to the complexity of cyclone formation processes. Last but not least, Saharan dust presents a large source for fertilisation of the Amazon rain-forest ecosystem, with an estimated 28 Mt of dust being deposited in the Amazon river basin every year (Yu et al., 2015). This once again emphasizes the direct link of the dust and carbon cycle.

On a regional, long term scale the drying of ephemeral lakes can cause distinct changes in local climate which in turn can lead to a change in dust emissions. Prominent examples for this are ephemeral lakes in Australia as well as the Aral Sea (Ginoux et al., 2012), where an increase in erodible soil has led to dramatic changes in meteorological circulations and dust emissions with both players interacting with each other as well (Darmenova and Sokolik, 2007). Another very prominent example is the Dead Sea, where local climate change is also accelerated due to the diminishing lake surface area. As the second part of this work focuses on the region further insight into this topic is provided in chapter 2.3.2. A change in ambient PM₁₀ concentrations due to increasing mineral dust concentrations can cause health problems, as high levels of PM₁₀ have been linked to higher mortality rates. Pope III et al. (2002) state that "each 10 μg m⁻³ elevation in fine particulate air pollution was associated with approximately a 4%, 6%, and 8% increased risk of all-cause, cardiopulmonary, and lung cancer mortality, respectively."

On a regional short term scale mineral dust has a variety of effects which makes it an important aerosol to be included in weather forecasting. Dust storms are relevant to many aspects of society, the most direct consequences are the adverse effects of peak mineral dust concentrations on human

health. In this connection not only the impact of the mineral dust particles itself is of importance but also the substances which are emitted along with the dust such as anthropogenic pollutants, pathogens and biological material. Goudie (2014) shows that a number of effects on the human system such as "respiratory disorders, cardiovascular disorders, conjunctivitis, skin irritations, meningococcal meningitis, valley fever as well as diseases associated with toxic algal blooms" can be attributed to dust storms. During the dust storm investigated in the second part of this work at least eight people were reported to have died due to respiratory problems and hundreds were hospitalized. Another important impact of mineral dust is on energy production. Due to the increasing amounts of photo-voltaic power being installed around the globe it is important to provide accurate forecasts of solar radiation for the next day's energy market prediction. It is thus crucial to implement the radiative effect of mineral dust in numerical weather prediction models particularly in dust prone desert regions. As severe dust events come along with drastic reductions in visibility an accurate forecast is also necessary for traffic management, especially in aviation where the spacing between approaching aircraft at airports depend on visibility criteria. A last, but highly influential effect is the regional scale and short term impact of mineral dust on synoptic scale weather forecasting itself due to its interaction with meteorology. The change in radiative transfer throughout the atmosphere due to mineral dust has a non-negligible influence on the state of the atmosphere for weather forecasts (Pérez et al., 2006; Bangert et al., 2012; Rémy et al., 2015). Due to its severe effects and strong influence on atmospheric state, an accurate forecast capability of mineral dust and its related processes in numerical weather models is desirable, this work presents a step towards achieving this goal for ICON-ART.

2.2 Modelling mineral dust

Modelling mineral dust remains a challenge, as most effects related to the numerical description of mineral dust in the atmosphere involve subgrid-scale processes. Acting on scales smaller than the grid point distance these processes remain unresolved in numerical weather prediction and climate models. Therefore the processes need to be parametrized in order to include their non-negligible effect on large scale dynamics. A critical feature requiring parametrization are dust emission processes, a short outline is given in the next section. Focusing on the atmospheric short-term effects of mineral dust, its influence on radiative transfer and cloud formation is important. However, under the header of these two categories a variety of involved processes become apparent which are discussed further in section 2.2.2. A third focus is put on mineral dust events caused by convective cold-pool outflows, because the event studied in the second part of this work belongs to this category.

2.2.1 Dust emission

Dust emission itself is highly parametrized due to the micro-physical processes involved. Even some of the most important atmospheric driving systems involved are parametrized in coarse resolution global circulations models. Dust emission is explained by a physical process called

saltation which depends on wind speed in a highly non-linear way, other important factors are soil type and soil moisture content. Saltation describes the emission of smaller dust particles, which are bound in soil crust more tightly by cohesive forces, through the impaction of larger particles. Large uncertainties exist for dust emission, both in measurements and numerical emission schemes (Shao et al., 2011b) and recent studies suggest that the emitted size distribution of mineral dust particles does not depend on wind speed challenging previous theories (Kok, 2011). Modelling the size distribution correctly is of crucial importance to the radiative effect of mineral dust (Marticorena, 2014) and therefore a large source of uncertainty as is elaborated in chapter 4.3.3. A more detailed description of the mineral dust emission scheme used in ART is given in chapter 3.1.2.

Heinold et al. (2013) estimate the contribution of different meteorological systems to dust emission in summertime West Africa. They state that approximately 40% of dust emissions can be linked to nocturnal low level jets (NLLJs), 40% to cold pool outflows from convective systems and 20% to unidentified processes such as dry convection, land-sea and mountain circulations. Although a direct transfer of their results to the Eastern Mediterranean is not feasible the study still provides valuable insight into the mechanisms and characteristics of dust emission driving systems. Corroborating work done by Marsham et al. (2011), Heinold et al. (2013) highlight the need for convection permitting resolution modelling in order to represent moist convective processes driving dust emission correctly.

In another in-depth study of the problems regarding emission associated with convective cold pool outflows Pantillon et al. (2016) perform a year-long convection permitting simulation in the Sahara region. They conclude that in this region the contribution of convective cold pool outflows to dust uplift potential is in the order of one fifth of the annual budget, with substantially higher proportions up to one third over the summer months. Furthermore they develop a parametrization to overcome the problem of missing emissions due to unresolved moist convection and thereby lack of cold pool outflows in coarse resolution atmospheric circulation models.

As dust emission by convective cold-pool outflows is especially difficult to model and important to this study further insight into this topic is provided in section 2.2.3.

2.2.2 Influence on radiative transfer

In the following the short-term local radiative effect of mineral dust is discussed in more detail as the implementation of the mineral dust radiative feedback in ICON-ART is the first part of this work. The means by which aerosols can influence atmospheric state is depicted in figure 2.2. The effects caused by the direct interaction of mineral dust with radiation, which are important for this study, can be split into two categories again. The first category is called direct effect of mineral dust, the second semi-direct effect. The former is shown on the far left side of figure 2.2, the latter on the far right side and an introduction to both is provided in the following.

The direct radiative effect of mineral dust is caused by two phenomena. The first is scattering and absorption of incoming solar shortwave radiation, the second absorption and re-emission of longwave solar and terrestrial radiation. Because mineral dust causes scattering in the shortwave

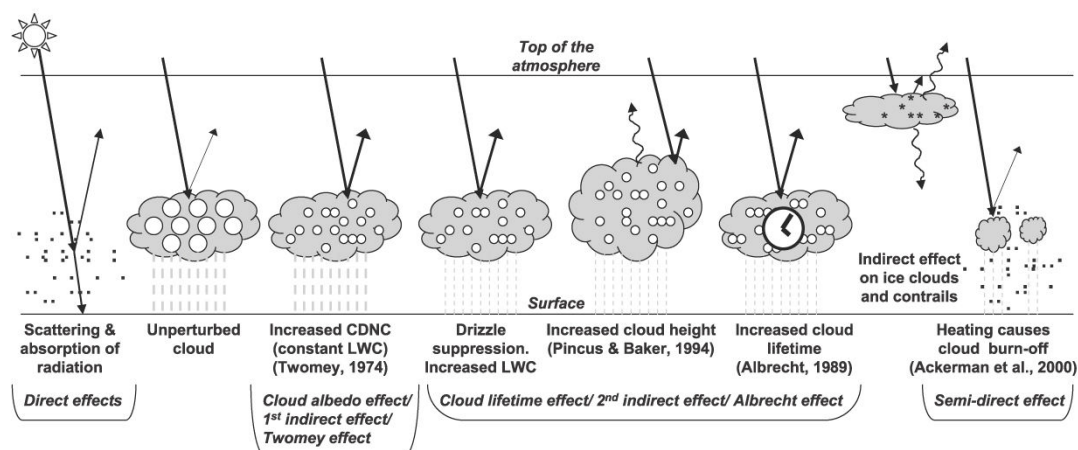


Figure 2.2: "Schematic diagram showing the various radiative mechanisms associated with cloud effects that have been identified as significant in relation to aerosols (modified from Haywood and Boucher, 2000). The small black dots represent aerosol particles; the larger open circles cloud droplets. Straight lines represent the incident and reflected solar radiation, and wavy lines represent terrestrial radiation. The filled white circles indicate cloud droplet number concentration (CDNC). The unperturbed cloud contains larger cloud drops as only natural aerosols are available as cloud condensation nuclei, while the perturbed cloud contains a greater number of smaller cloud drops as both natural and anthropogenic aerosols are available as cloud condensation nuclei (CCN). The vertical grey dashes represent rainfall, and LWC refers to the liquid water content." Figure and caption from Forster et al. (2007).

part of the spectrum its presence leads to reductions in incoming shortwave radiation. This in turn influences the amount of energy available at the surface. Furthermore, absorption of radiation in the shortwave part of the spectrum causes a warming of the mineral dust layer. Similarly, absorption of longwave radiation reduces the amount of energy being radiated into space at the top of the atmosphere in the longwave part of the spectrum. This causes a warming of the dust layer, which in turn increases the amount of down-welling atmospheric longwave radiation reducing night-time cooling at the surface.

The radiative forcing of mineral dust can be quantified as a change in radiative flux due to the presence of mineral dust compared to a dust-free atmosphere. Although the radiative effects can be diverse, many studies nevertheless try to quantify changes in radiative fluxes due to aerosol optical thickness τ in a measure called forcing efficiency which gives the change in radiative flux per unit of aerosol optical depth. A short overview of results from different studies is given by Highwood and Ryder (2014, table 11.2).

A comparison between studies is complicated as several factors influence the mineral dust radiative forcing. Firstly, the height of the dust layer and the atmospheric state influence the strength and even sign of the mineral dust radiative effect because of differences in dust layer temperature and thereby emission characteristics in the longwave part of the spectrum. Secondly, another influential factor on overall mineral dust radiative forcing is the earth's surface characteristics. A dust layer over dark ocean contributes more to radiation being reflected back into space at top

of the atmosphere (TOA) than a dust layer over a bright desert surface where a significant part of radiation is reflected back even under dust free conditions. Therefore the surface albedo is an important factor when investigating radiative flux changes due to mineral dust. Thirdly, the presence of other, optically thicker absorbers such as clouds complicates the radiative impact of mineral dust even further. As Choi and Chung (2014) show, differences in aerosol radiative forcing on the order of one magnitude are induced by the fact whether an aerosol is located above or below clouds. Last but not least, the contribution of different parts of the radiation spectrum varies during the day, further complicating the quantification of an overall mineral dust radiative forcing.

Keeping in mind all of the above facts, most studies find a direct shortwave radiative forcing efficiency at the bottom of the atmosphere in the range of -38 W m^{-2} to -140 W m^{-2} per unit aerosol optical depth τ over land for regional averages. However, in dust source regions and below optically thick dust plumes forcing efficiency reaches higher values, with Rémy et al. (2015) reporting up to $-200 \text{ W m}^{-2}\tau^{-1}$ and Helmert et al. (2007) reporting up to $-220 \text{ W m}^{-2}\tau^{-1}$. In the longwave part of the spectrum, where less studies are available, the radiative forcing at the top as well as bottom of the atmosphere is consistently estimated to be in the range of $2 \text{ W m}^{-2}\tau^{-1}$ to $35 \text{ W m}^{-2}\tau^{-1}$. Recent studies from both modelling and measurements show that the radiative forcing of mineral dust from Asia is comparable to that of Saharan dust (Shao et al., 2011a, and references therein).

Naturally the mineral dust radiative forcing has an impact on surface temperature which results in cooling during the day and warming during the night.

In a study conducted by Helmert et al. (2007) study, mineral dust forcing showed an effect on 2m-temperature of up to -6 K in dust source regions during daytime, with an average of -3 K . They were also able to obtain forcing efficiencies of mineral dust on 2m-temperature, these are around $-2.1 \text{ K } \tau^{-1}$. Their mean values are comparable to those of Heinold et al. (2008) who report an average temperature effect of -1.3 K to -5.7 K of mineral dust during daytime. However the peak temperature reductions in the Heinold et al. (2008) study reach higher values of up to -17 K . A similarly magnitude is reported by Tegen et al. (2006), with decreases in daytime 2m-temperature down to -11 K . The part of radiation which does not reach the surface and is not scattered back into space heats the dust layers where it is absorbed. Concluding, the day-time mineral dust radiative effect can be summarized to redistribute energy away from the surface to dust layers which are heated, thereby increasing atmospheric stability. The implications of this effect on boundary layer dynamics is discussed at the end of this section.

Most studies state that the night-time warming effect due to dust is of lesser magnitude than the day-time cooling and confined to a very thin layer at the bottom of the planetary boundary layer. Tegen et al. (2006) generalizes that an optical thickness above 0.5 does not lead to a further increase in night-time surface temperatures, whereas decreases in surface temperature during day-time still scale linearly. Quantifying the night-time increase in surface 2m-temperature due to increased down-welling longwave radiation is more difficult. Less studies report specific values and not all models are able to develop a well defined boundary layer according to Tegen et al. (2006), who themselves report an increase in surface temperature of 1 K . Rémy et al. (2015)

states an increase of surface temperatures during night of 2.5 K in regions where the dust load exceeds an AOD of 2. Nevertheless, this seemingly small increase can have an important impact on the diurnal dust emission cycle.

A feedback of the aerosol direct effect which is intensively studied is the influence of dust layers on boundary layer dynamics and dust emission. Besides the previously discussed influence on surface temperature the change in surface energy budget feeds back on the partitioning of sensible and latent heat fluxes, this in turn causes differences in boundary layer characteristics and development (Heinold et al., 2008).

On the one hand, night-time destabilization of the boundary layer due to warming caused by a near surface dust layer can lead to increased surface wind speeds and thereby higher dust emissions as more momentum is mixed downwards. Heinold et al. (2008) found an increase in night-time surface wind speeds of 14% in the Bodele depression due to mineral dust radiative feedback. On the other hand, the less stable stratification weakens the development of a NLLJ whose break-up in the morning hour is responsible for a peak in dust emissions during the morning hours (Heinold et al., 2013).

During daytime, mineral dust shows two counteracting effects as well. Stabilization of the boundary layer leads to a negative feedback of the dust concentration on dust emission due to increased thermal stability. A reduction of incoming solar radiation at the surface and an increase in upper-boundary layer heating due to absorption increase stable stratification of the boundary layer and thereby weaken surface wind speeds due to reduced turbulent downward mixing of momentum. However, during daytime the increased stability and decreased vertical extent of the mixing layer favours a delayed break-up of the nocturnal low-level jet. It can thereby result in a strengthening of the NLLJ in the early morning hours and consequently higher emissions (Heinold et al., 2008). The multitude of different effects discussed here highlight the importance of modelling the radiative effect of mineral dust within a well-developed boundary layer. It is further underlined by the study of Heinold et al. (2013) who estimate that NLLJs contribute about 40% to dust emission in West Africa and who also suggest the existence of wide-spread NLLJs in aged cold pool outflows from convective events which are discussed in the following section.

In addition, Rémy et al. (2015) find a secondary effect of mineral dust radiative forcing on horizontal wind fields. During daytime, due to increased horizontal gradients of surface temperature at the edge of the dust plume thermal wind systems are strengthened leading to increased surface wind speeds. The opposite secondary mineral dust radiative forcing effect is found during the night-time, meaning decreased horizontal temperature gradients and thereby decreased wind speeds and lowered dust emissions. Summarizing, it can be said that mineral dust reduces the daily cycle of surface temperature, this results in stabilization of the boundary layer during daytime and destabilization during night-time which in turn feeds back on the diurnal dust emission cycle.

The semi-direct effect of mineral dust describes the feedback of mineral dust-radiation interaction on atmospheric state. Variations in atmospheric energy fluxes cause changes in temperature and other parameters and thereby in vertical stability which can alter cloud characteristics. Due to the larger optical depth of clouds compared to that of aerosols even small changes in cloud cover

can cause distinct changes in atmospheric circulation. The semi-direct effect of mineral-dust is included in the model through feedback of the radiation routine on meteorological parameters. It can not be easily separated from the aerosol direct effect in numerical weather prediction models, therefore when investigating the aerosol radiative effect it always refers to both the aerosol direct radiative effect and the aerosol semi-direct radiative effect.

As depicted in figure 2.2 there are other important mechanism by means of which aerosols can influence atmospheric state, the so called indirect effects. Aerosols can serve as cloud condensation nuclei and ice nuclei for heterogeneous freezing and thereby affect cloud micro-physical processes. As previously stated mineral dust is an excellent ice nuclei for heterogeneous freezing processes (Hoose and Möhler, 2012) and its wide abundance makes it the most important ice nuclei (Cziczo et al., 2013). Through altering cloud properties such as the cloud droplet and cloud ice number concentration, cloud appearance can be changed, for example by increasing cloud albedo due to an increased number of smaller droplets. This effect is the so called 1st indirect effect or Twomey effect (Twomey, 1974). These changes on cloud micro-physical properties can again have an effect on other cloud characteristics such as precipitation generation, cloud height and lifetime. The influence of this mechanism on atmospheric state is named 2nd indirect effect or Albrecht effect (Albrecht, 1989). The 1st and 2nd aerosol indirect effects are not investigated as a part of this work because they require extensive treatment of cloud micro-physical processes in combination with mineral dust in the model. The cloud micro-physical processes and aerosol interactions are implemented in ICON-ART, however, investigation of these effects is beyond the scope of this work.

2.2.3 Dust events caused by convective cold-pool outflows

An important source for mineral dust in the atmosphere are cold pool outflows generated by strong convective events. An important aspect of the severe dust event simulated in the second part of this work is dust generation by such a convective cold pool outflow (CPO), some insight into their characteristics is provided here.

The occurrence of CPOs has been documented for all major dust source regions worldwide (Knippertz, 2014). The scale of events responsible for convective cold-pool outflows ranges from micro-bursts to storms spanning several hundred kilometres in the form of organized moist convection, causing the so-called haboobs. Characteristic features which can be observed in connection with density currents are displayed in figure 2.3. A main CPO generating mechanism are hydro-meteors falling into sub-saturated air masses of the dry boundary layer, which can exceed heights of 5 km in lower latitudes creating substantial potential for latent cooling. According to Knippertz et al. (2007) typical temperature decreases are in the order of 10°C, thereby causing density differences of 4%. The difference in air-density can induce high vertical wind-speeds and thereby create organized down-drafts which are transformed into horizontally spreading air-masses when approaching the surface. Another important energy source is created by the drag of the falling water droplets, creating strong downward vertical motion. Additional intensification of the CPO can be caused by downward mixing of momentum from upper levels in the course of the

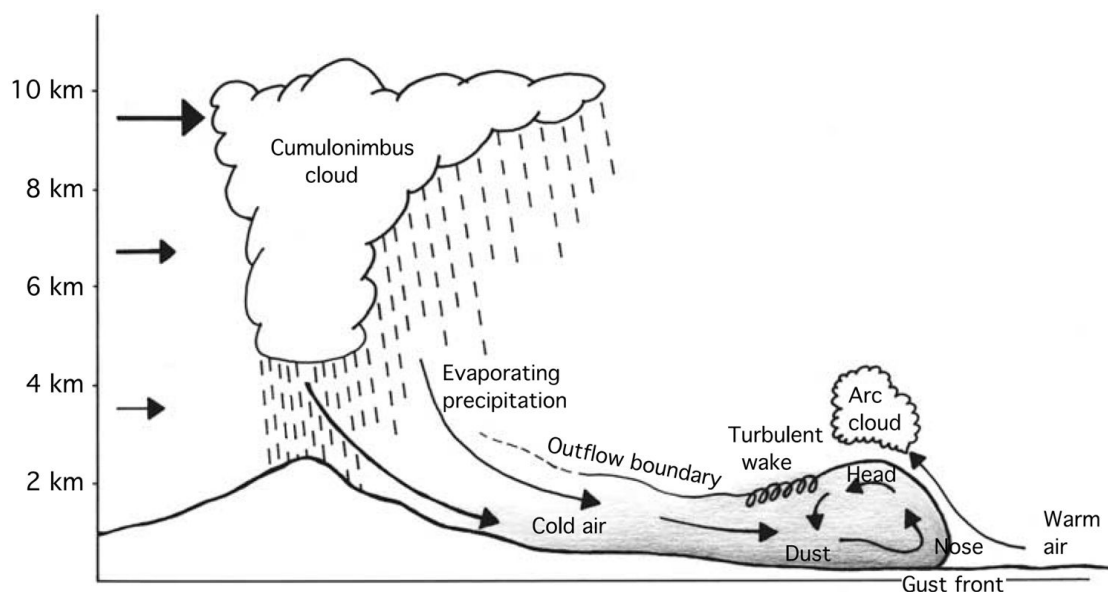


Figure 2.3: Schematic depiction of cold-pool outflow from convective event with associated characteristic flow structures, adapted from Knippertz et al. (2007).

convective event. A down-slope gradient of the terrain can further aid the propagation of density currents.

Typical CPO propagation speeds are in the order of 10 m s^{-1} , although wind speeds behind the leading edge can be substantially higher, thereby enabling strong dust emission. The leading edge of a CPO shows distinct features. These are gusty and strong turbulent winds, an increase in dew point temperature due to the higher relative humidity of the outflow air mass and a drop in visibility. An arc cloud forming above the leading edge is often detectable on satellite images. Even though surface conditions in desert regions are usually very dry, the great height of the boundary layer with a dry-adiabatic lapse rate and constant mixing ratio leads to high relative humidities in the upper boundary layer, as explained by Knippertz et al. (2007). Thereby, lifting motions in front of an approaching density current can result in cloud formation even in a dry environment.

Modelling mineral dust emissions due to CPOs still poses a challenge due to the high spatial resolution needed to enable an explicit treatment of moist convection. In coarse-grid models with parametrized convection the related up- and downdrafts occur within a the same grid cell, preventing the observed organisation and spread over larger areas. This presents a major short-come of all global models for dust emission processes and attempts have been undertaken to overcome it with the help of parametrizations (Pantillon et al., 2015). However, only the explicit treatment of convection in the model allows for meso-scale formation and organisation of the same, which in turn enables cold-pool outflows and dust emission intensities as observed. This is illustrated in figure 2.4 which is extracted from Marsham et al. (2011). They find a clear influence of model resolution on a parameter termed 'uplift potential', which describes the cube of the 10 m-wind speed above a threshold of 7 m s^{-1} . The uplift potential is thereby closely related to dust emission

which scales with the cube of the friction-velocity above a certain threshold (see section 3.1.2). It is apparent that only convection permitting model runs (solid lines) are able to resolve the afternoon peak in dust emission during convective days, which is responsible for approximately half the total uplift potential. Furthermore, these runs show a markedly higher overall daily dust uplift potential. During a longer period of ten days the models with parametrized convection show an increase in dust uplift potential due to NLLJs (not shown). This equalizes the daily uplift potential between different model set-ups, but leads to differing diurnal cycles. The models with parametrized convection still fail to reproduce the afternoon peak in dust uplift potential. According to Marsham et al. (2011) the increase in night-time emissions is assumed to be due to lacking ventilation of the Saharan heat low by CPOs and thereby underestimation of the pressure at centre resulting in stronger NLLJs. This assumption is further investigated and shown to be accurate by Redl et al. (2016).

The findings of Marsham et al. (2011) are confirmed by a subsequent study of Heinold et al. (2013) who directly model dust emission due to CPOs and are able to further group the diurnal cycle of dust generating events, results from this work were already discussed in section 2.2.1. In addition, Heinold et al. (2013) propose a mechanism by which a NLLJ can form in aged CPOs, showing characteristics of both systems and leading to high dust emissions in the morning hours after a convective event. According to them, aged cold pools can decouple from the land surface through a radiatively formed stable nocturnal boundary layer and locally induced pressure gradients can trigger NLLJ formation. In their study this process is responsible for 23% of dust emissions. However, they state the limitation that their study did not include the mineral dust radiative effect which can alter boundary layer characteristics as discussed above.

Furthermore Heinold et al. (2013) state that CPOs result in more intense dust emissions than NLLJs, giving stronger dust events. This is illustrated in figure 2.5, where the integral over the simulated dust emission per active grid cell (red curve) shows a value of 1.3 t of emitted dust per active grid cell in the hours from 15 – 02 local time compared to 0.8 t in the hours from 03 – 14 local time, with the maximum also being distinctively higher. The black line shows the mean hourly dust emissions over the whole domain, which confirms the approximately equal overall contribution of CPOs and NLLJs to dust emission.

Even when explicitly allowing moist convection and assuming correct initiation timing the model set-up can still influence CPO characteristics. Knippertz et al. (2009) found an important impact of the cloud-microphysical scheme used and even greater effect of the prescribed turbulent

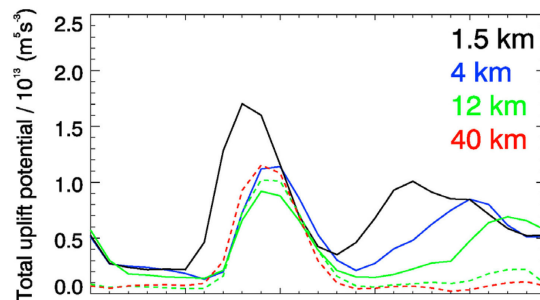


Figure 2.4: Importance of model resolution for correctly modelling emissions from CPOs, extracted from Marsham et al. (2011). Domain integrated diurnal uplift potential for different grid spacings for a convectively active 2-day period in western Africa. Dashed lines represent models with fully parametrized convection.

length scale for vertical mixing. According to their study, usage of the Seifert and Beheng two-moment cloud micro-physics scheme (Seifert and Beheng, 2006) results in a changed timing of the density current evolution, with more intense winds during the early stages but also a faster decay. Decreasing the turbulent length scale for vertical mixing leads to a more widespread and faster propagating cold pool with higher wind speeds. They attribute this to a more widespread precipitation due to an easier initiation of convection, resulting in more evaporational cooling and therefore a stronger density current. Furthermore, the decreased mixing of surrounding air masses into the cold-pool outflow increases its lifetime and the decreased mixing in the boundary layer enables the maintenance of larger vertical temperature gradients during daytime.

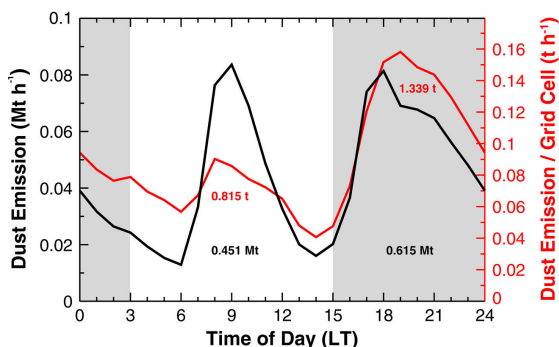


Figure 2.5: Diurnal emission characteristics due to CPOs and NLLJs for a 40 day period in western Africa from 4 km-resolution convection permitting simulations, extracted from Heinold et al. (2013). The black line shows domain averaged hourly dust emission, the red line mean hourly dust emission per active grid cell. Displayed as numbers are integrated values from 03 – 14 LT and 15 – 02 LT.

the order of 5 W m^{-2} and thereby warming of the lowest layer. They state that this effect becomes increasingly important in the later stages of a cold pool development after the dynamical effects diminish. The hereby reduced stratification of the cold-pool in the lowest layers can result in increased vertical mixing, turbulence and drag, leading to a faster decay of the cold-pool. The third effect, which is not included in the model of Redl et al. (2016), is the emission of mineral dust due to the high wind speeds which can reduce incoming shortwave radiation during daytime. This can weaken radiative heating of the cold-pool and thereby increase lifetime. During night-time, increased longwave down-welling radiation can lead to a decreased decoupling from the surface in analogy to the effect of water vapour. It should be noted however, that this effect could also lead to increased emissions of mineral dust during night-time, especially in vertically mighty CPOs where only the lowest layers are affected. Keeping in mind the findings from the previous chapter, namely that the day-time cooling due to mineral dust is of larger magnitude than

Besides the atmospheric flow conditions of the surrounding region there are three mechanisms which can influence the evolution and lifetime of a CPO. The first is intensively studied by Redl et al. (2016), demonstrating that sometimes the cold pool can show higher surface temperatures than the surrounding air masses at night. This counter-intuitive behaviour is due to the dynamical breakup of the extremely stable night-time inversion in the surface layers by increased turbulent mixing. The result is transport of energy towards the surface and reduced cooling of the same, which in turn radiates this energy into to space. The overall effect is a loss of energy from the lower boundary layer in the initial stages of cold-pool development. Redl et al. (2016) also investigate the second effect of higher humidity within the cold air-mass leading to increased down-welling longwave radiation in

the shallow nocturnal warming, it can be assumed that the daytime stabilizing effect of mineral dust is of greater importance to the evolution of the CPO, this is investigated in chapter 5.

Simulation and forecast of mineral dust events from convective cold pool outflows on regional scales such as the Dead-Sea requires a model capable of simulating all relevant processes with sufficient spatial and temporal resolution. The four most important processes which need to be included are:

1. non-parametrized convection allowing for organized cold-pool outflow,
2. an adequate treatment of moist processes capable of representing the evaporating hydrometeors (two-moment scheme),
3. treatment of aerosols to allow for dust emission, transport and deposition and
4. its influence on radiation and thereby atmospheric stability.

The ICON-ART model system allows for a seamless simulation of all involved processes, section 3.1 provides a short introduction.

2.3 Mineral dust in the Eastern Mediterranean

This section deals with characteristics of dust events in the Eastern Mediterranean in general and the Dead-Sea Rift Valley in particular. The topography as used by the finest ICON-ART model domain with 2.5 km effective grid-spacing is depicted in figure 2.6. The dominant features visible are the Zagros mountain range stretching from Iran towards Turkey with an elevation of up to 4500 m, converting into the Taurus mountain range in southern Turkey. Situated at the foothills of this mountain range are the Euphrat-Tigris low lands. In the south-western part of the ICON-ART domain the Dead Sea Rift Valley is visible, which is bordered by the eastern part of the Mediterranean Sea. This region is termed Eastern Mediterranean (EM) in the following. The dust event simulated in the second part of this work originates in two consecutive stages from the Euphrat-Tigris low lands (referred to as Mesopotamia in the following). The first stage is a combination of a convective cold pool outflow with an intense heat low occurring over northern Syria which is marked with a red ellipse numbered one. The second stage is caused by two subsequent cold-pool outflows from a meso-scale convective system over the Syria-Turkey-Iraq-Iran border region denoted by the red ellipse numbered two. The event causes long range transport of mineral dust towards the EM and the Dead-Sea Rift Valley therein (red ellipse numbered three). Features of the EM which are relevant to understanding dust events in this region are outlined and a special focus is put on the Dead Sea Rift Valley due to its unique orographic setting and importance to this study.

The EM is an interesting study region due to frequently occurring dust events which affect a large number of people which is not necessarily the case in all dust prone desert regions. Dust events in the EM are usually associated with strong south-westerly and southern flows in the region. As a result the most important remote dust source regions for the EM are situated in north-western

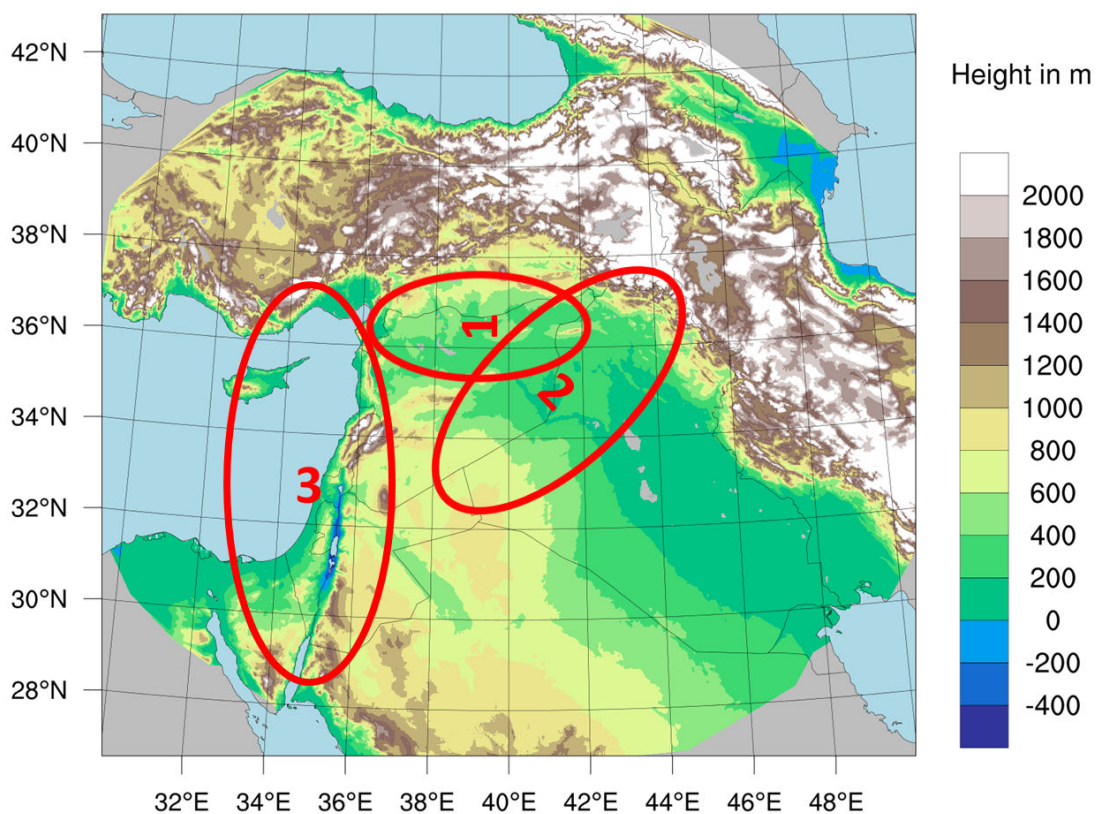


Figure 2.6: Topography in the study region as used in the ICON-ART 2.5 km domain. Marked as red ellipses are (1) northern Syria dust source region, (2) Mesopotamia dust source region and (3) the Dead Sea Rift Valley in the Eastern Mediterranean as the long-range dust transport target area. Areas outside the finest domain are displayed in grey.

Africa and the southern Arabian peninsula (Ganor, 1991). According to a subjective synoptic classification conducted by Dayan et al. (2008), the synoptic scale systems associated with dust transport towards the EM are with a frequency of 60% Cyprus Lows, Sharav cyclones with 12% and Red Sea troughs with 12% as well. Consequently, the number of dust events in the EM is correlated with cyclone activity in the region. Long-range mineral dust transport towards the EM peaks during the transitional seasons in spring and autumn, when these low pressure systems and their associated fronts occur most frequently in the region (Singer et al., 2003, and references therein; Dayan et al., 2008).

The strong seasonality of dust events based on observations of daytime visibility for Beersheva in Israel is depicted in figure 2.7. A clear maximum of dust events in February, March and April is visible and a minimum in the summer season. Figure 2.8 shows the monthly mean values of aerosol optical depth for Sede Boker in Israel, measured by AERONET and retrieved from MODIS Deep-Blue as presented by Ginoux et al. (2012). The values from AERONET show a clear maximum in April and May. Highlighting the difficulties in retrieving AOD values using inverse methods, the values retrieved from MODIS Deep-Blue show large differences compared to those from AERONET. Nevertheless they show a clear peak in late spring, the same is true for the values of mineral dust optical depth (DOD).

When comparing the dust observations from Beersheva with those from Sede Boker, which is located only 40 km away, again large differences become apparent. Especially the high values of dust optical depth in June, July and August from AERONET and MODIS are not detectable in the observations from Beersheva. This could be due to the fact that the observations in Beersheva were based on daytime horizontal visibility estimates from human observers, whereas those in Sede Boker are based on full-time extinction profiles from automated physical instruments, however a detailed analysis is beyond the scope of this work.

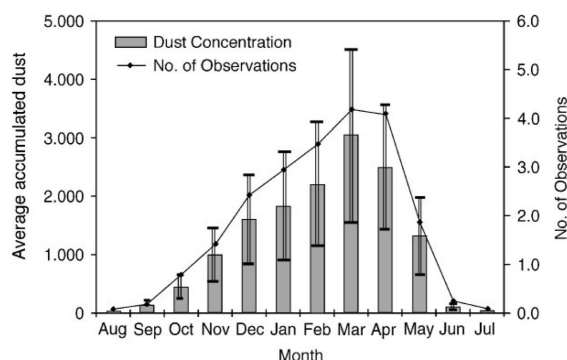


Figure 2.7: Monthly values of dust occurrence from visibility measurements in Beersheva, extracted from Dayan et al. (2008).

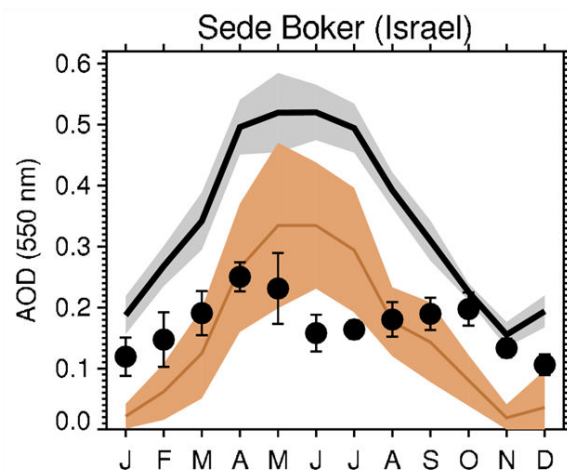


Figure 2.8: Monthly values of mean aerosol optical depth at Sde Boker from AERONET (black dots), MODIS-DB2 (black line) and dust optical depth from MODIS-DB2 (brown line). Bars and shadings represent the standard deviation. Adapted from Ginoux et al. (2012).

Resulting from the climatology of dust events in the EM, many studies investigate and simulate dust events in connection with low pressure systems and long-range transport of mineral dust from the Sahara towards the EM (Vogel et al., 2006; Spyrou et al., 2013; Rémy et al., 2015; Kishcha et al., 2016). This study is the first to simulate long-range transport of mineral dust towards the EM in connection with convective cold-pool outflows from Mesopotamia. The timing and synoptic situation of the severe dust event are unusual as it occurs in September and thereby not in a transitional season when most dust is transported towards the EM, but it is nevertheless of great importance due to the magnitude of the event.

2.3.1 Mesopotamia

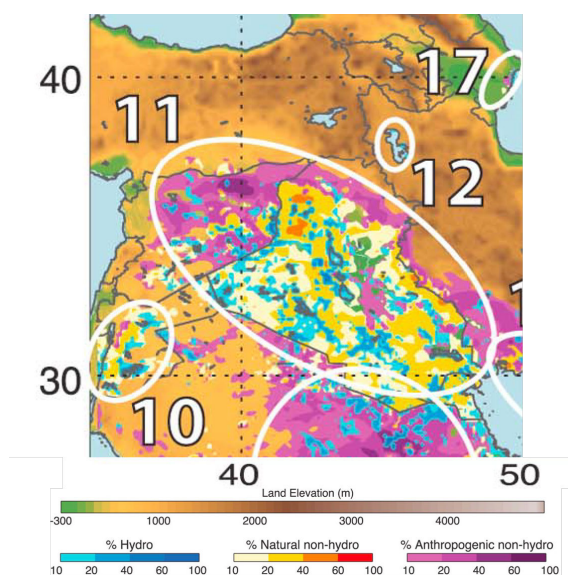


Figure 2.9: Dust emission regions in the Middle East for the main season March, April, May, adapted from Ginoux et al. (2012). Colour-coded is the frequency of days with a DOD > 0.2 in percent. Different colour scales refer to emission attributed to ephemeral water bodies (hydro), without ephemeral water bodies (non-hydro) and more than 30% land use (anthropogenic). Main source regions are (10) the Jordan River Basin, (11) Mesopotamia, (12) Urumia Lake of Iran and (17) Qobustan in Azerbaijan.

CPO events from the Zagros Mountain range towards the north-west. In further attributing dust sources to specific source mechanism, they state that dust sources over Syria are mostly anthropogenic whereas they are mostly natural over Iraq.

Analyses of mineral dust distribution from satellite data are problematic, as shown in the previous section, and often inherit a systematic bias due to under-representation of dust below clouds for example in CPOs (Heinold et al., 2013). Nevertheless, the study by Ginoux et al. (2012) provides a good overview of the most important dust source regions in the Middle East by analysing the MODIS Deep-Blue dust optical depth climatology. Results of their study are depicted in figure 2.9. The frequency of occurrence of days with a dust optical depth greater than 0.2 is higher than 20% in most of Mesopotamia (denoted as region 11), with a maximum of occurrence in summer. This is also the region where dust pick-up from the CPO happens in this study. According to Ginoux et al. (2012), the maximum frequency of occurrence is located in the north-west of region 11 in Syria and along the Syrian-Iraqi border where several salt flats are situated. This is exactly where the CPO in this study reaches its highest intensity. Possibly, a connection exists between the maximum in dust occurrence detected by Ginoux et al. (2012) and the frequent occurrence of

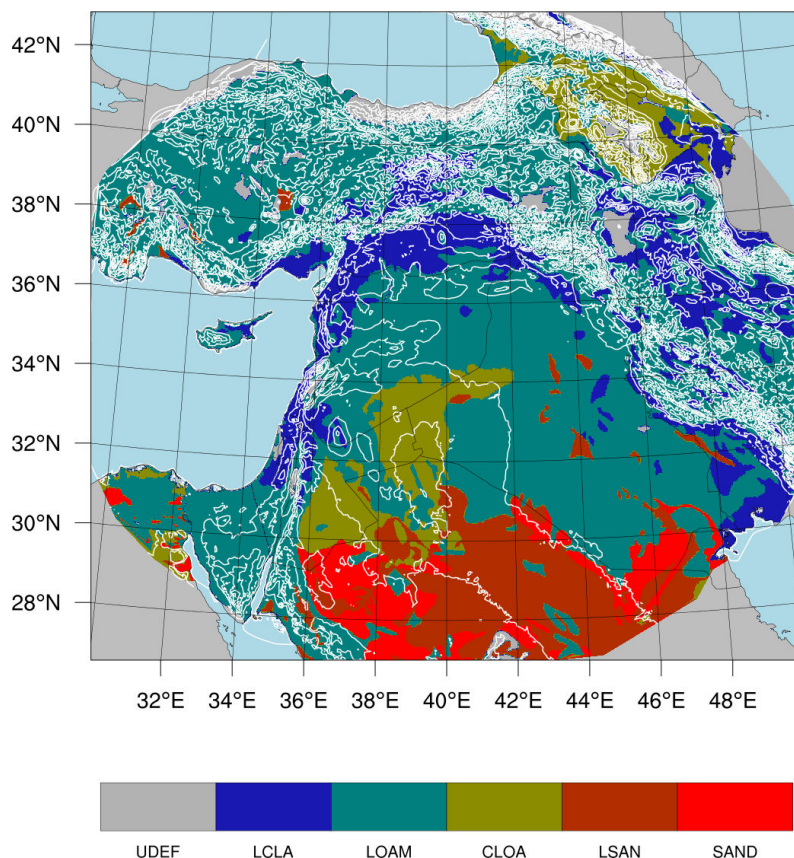


Figure 2.10: Dominant soil types in study region colour coded from HWSD soil data set. Abbreviations are UDEF - Undefined; LCLA - Light clay; LOAM - Loam; CLOA - Clay loam; LSAN - Loamy sand and SAND - Sand. White lines show topography height from -400 m to 2000 m in 400 m intervals.

A map of the dominant soil type from the Harmonized World Soil Database (HWSD) (Nachtergaele and Batjes, 2012), which is used for the dust emission scheme in ICON-ART simulations is displayed in figure 2.10. Further insight into the emission scheme used in ICON-ART is given in chapter 3.1.2. The differences in soil types lead to differences in saltating particle size distribution according to Shao et al. (2010). Another difference between soil types which is crucial for the dust emission scheme is the percentage of clay contained within the soil, as this determines the minimum soil moisture content. The regions where Ginoux et al. (2012) find highest dust emissions are well represented in their spatial distribution by loam soil in the HWSD soil data, this is the strongest emitting soil type above a friction velocity of 0.9 m s^{-1} under idealized conditions, in addition it has a low minimal soil water content. Notably, a change in soil characteristics and thereby dust emission with rising terrain towards Jordan and northern Saudi-Arabia (clay loam) and along the Syrian and Lebanese coast (light clay) can be found in both datasets, Ginoux et al. (2012) and the HWSD soil data.

The word "haboob" is derived from the Arabic word "habb" meaning "wind" or "to blow". The coining of the term in Mesopotamia might be linked to the frequent occurrence of such dust events. Dust events caused by haboobs in Mesopotamia have been investigated, however their

usual extent and path of dust transport is assumed to be limited to Mesopotamia and the Persian Gulf region although no climatology exists yet.

Miller et al. (2008) investigate haboob dust storm characteristics over the Arabian peninsula with an extensive meteorological station network. They document haboobs travelling as far as 800 km from Syria towards the Persian Gulf and regularly more than 100 km. Furthermore, they report that whereas in the beginning the dust fronts coincide with the cold-pool fronts, they tend to advance faster and travel ahead of the cold-pool fronts with growing distance from the source. Conducting a frequency analysis of convectively active days, Miller et al. (2008) find that active days tend to cluster into periods of adjacent days, with 3-7 days of separation without activity. Towards August and September the periods of convectively active days tend to grow longer. They explain this behaviour with a quasi-stationary upper air ridge over the Arabian Peninsula and Persian Gulf during the south-west monsoon season causing strong mid-level subsidence of warm air which suppresses convection. However, small shifts in the ridge structure due to passing weather systems enable periodic moisture intrusions and increased instability. Using a highly idealized model of haboob generation, Miller et al. (2008) estimate that haboobs may contribute as much as 30% to the dust emission budget in the region, especially on days with weak synoptic forcing.

The event portrayed in this study consists of a period of convectively active days as well. However, its dust transport paths in connection with CPOs travelling towards the EM are rather unusual, due to multiple geographic facts. Firstly, the terrain in the region is rising from the Euphrat-Tigris region towards west, which hinders the spreading of density currents as they are gravity driven. Secondly, in order for the CPO to be reinforced during the next day, the timing of convection causing the outflow and propagation speed of the CPO has to enable transport towards a favourable region for re-intensification during the next day. Thirdly, the convective system responsible for the cold-pool outflow has to persist long enough to produce enough cold air in order to allow for a substantial momentum and lifetime of the cold pool. Convection driven solely by the orography of the Zagros Mountain range can be assumed not to fulfil these criteria. However, due to this special character of the event higher than usual dust emissions can occur as less frequent dust events can lead to higher intensity of dust events because the soil is not depleted of dust-sized particles suitable for emission (Marticorena, 2014).

2.3.2 The Dead Sea Rift Valley

For any transport of mineral dust from Mesopotamia towards the EM the Dead Sea Rift Valley poses an orographic barrier which greatly influences circulations systems and thereby dust transport processes. The Dead Sea Rift Valley is an approximately 600 km long and 20 km wide active tectonic zone (see figure 2.6, ellipse number three). On the western side it is bordered by the Judean Mountains, reaching an elevation of up to 1000 msl, on the eastern side by the Moab Mountains reaching up to 1300 msl. In the north the Dead Sea Rift Valley transforms into the Mounts of Lebanon with their highest mountain being the Mount Hermon with an altitude of 2800 msl. Between the Mount Hermon and the Moab Mountains exists a gap termed the Golan

Heights at an average altitude of 1000 msl. This gap is important to dust transport into the region from eastern directions which has to surmount the mountain ridges.

The Dead Sea (DS) is situated at the bottom of the Dead Sea Rift Valley, which is currently 429 m below sea level. The DS is a unique terminal lake with a salinity of 235 kg m^{-3} (Gertman and Hecht, 2002), however it faces severe environmental threats. Over the past 50 years mismanagement and overexploitation of water resources in the Jordan watershed have almost completely stopped the inflow of water into the DS and caused a decline of sea level of over 20 m with no signs of natural improvement (Gavrieli and Oren, 2004). This reduction in water body has led to a rapid local climate change Shafir and Alpert (2011), with severe implications for the unique environmental habitat and ecosystem. To gain a better understanding of the environmental processes influenced by the rapid local climate change in the region, an international research venue termed DESERVE (DEad SEa Research VENue) has been established in the region (Kottmeier et al., 2016). As a part of DESERVE an extensive field measurement campaign was conducted in the region recently to obtain a representative dataset describing the current atmospheric conditions.

The rapidly declining sea level has led to a split of the DS into two parts, the northern, natural water body and a southern artificially maintained one. Under natural circumstances the southern basin would have dried up in 1976 because of the declining water level (Steinhorn et al., 1979). However, companies pump water up from the DS to the industrial ponds to maintain their operations, thereby increasing evaporation from the DS by about 30% (Gavrieli et al., 2005). In addition, most of the touristic infrastructure at the DS on the Israeli side is located at these artificial ponds in Ein Bokek. From a tourist point of view, the atmospheric composition and conditions are of great importance because the DS is known as a centre for health cure due to its unique environmental setting. The rate of evaporation from the DS is of great importance because it directly influences the water level of the DS as a terminal lake as well as various chemical processes (Stanhill, 1994). Furthermore it is of importance to the industrial operations by the Dead Sea Works and Arab Potash Company which extract valuable components from the DS water by means of evaporation in large artificial ponds in the southern basin of the DS. Therefore, many studies have been conducted in order to give a more accurate forecast of evaporation (Ilotoviz et al., 2015, and references therein).

When investigating atmospheric processes including evaporation in the Dead Sea Valley mineral dust is an important and abundant player (Singer et al., 2003, 2004). As discussed in section 2.2.2, mineral dust directly influences atmospheric circulation and evaporation through modifying incoming solar radiation and altering atmospheric stability which is a key driver of local atmospheric circulation systems.

The main local meteorological circulation systems in the region are the EM land-sea breeze and the DS lake breeze, both being heavily influenced by the steep orography. Alpert et al. (1997) and Shafir and Alpert (2011) have shown that evaporation of the DS has increased in recent times due to local as well as global climate change affecting the region. On a local scale, a weakening DS lake breeze due to reduced water surface area leads to higher temperatures and reduced relative humidity in the area, providing a positive feedback mechanism to increased evaporation. The weakened DS lake breeze also leads to the Mediterranean Sea breeze penetrating the valley with

higher intensity, thereby increasing evaporation even more. These phenomena can be expected to increase with the further drying of the DS and their interaction with mineral dust concentrations in the regions are of great importance. The greater availability of erodible soil together with a strengthened penetration of the Mediterranean Sea breeze can increase local mineral dust emission. This has also been noted by Ginoux et al. (2012), who note a cluster of anthropogenic and hydrological sources along the Jordan River (denoted as ellipse 10 in fig. 2.9). With reference to other studies they attribute it to wind erosion of desiccated sediments induced by the diversion of water (Ginoux et al., 2012, and references therein). However, the feedback of the higher mineral dust concentrations on meteorological systems in the region is yet unknown, highlighting the need for high-resolution models such as ICON-ART capable of simulating all involved processes.

Dust transport processes within the Dead-Sea Rift Valley have been of interest in previous studies. In a first attempt for small scale modelling of mineral dust transport processes Vogel et al. (2006) apply a regional model system with high horizontal resolution to the DS area. They find an effect of the local circulation system on mineral dust concentrations within the valley. The results show that eastward transport of mineral dust is hindered by the high orography and thermal stratification in the valley, furthermore a channelling effect of the valley is visible. A size dependent sedimentation velocity alters the size distribution of number and mass densities within the valley in their study. Vogel et al. (2006) already highlight the importance of a varying size distribution throughout the valley for the radiative effect of mineral dust although they do not investigate it directly.

Kishcha et al. (2016) conduct a regional scale study of a dust event affecting the Dead Sea Valley in connection with a synoptic scale passing frontal system. They run convection permitting COSMO simulations with 2.8 km grid spacing and by that are able to resolve local circulation systems in the Dead Sea Valley. However, Kishcha et al. (2016) do not investigate the radiative effect of mineral dust in their simulations. In comparing the simulation results with measurements they find that the model simulates local circulation systems reasonably well. Kishcha et al. (2016) are able to reproduce the measured concentrations within and outside the Dead Sea Valley satisfactorily. Separating between local dust emissions and long-range dust transport, they find that in their case local emission due to strong down-slope winds are responsible for high dust concentrations and that long-range transport from the Sahara is negligible.

To my knowledge this work presents the first study investigating the local effect of mineral dust in the Dead Sea Valley including interaction with radiation. It also presents the first study investigating long-range transport of mineral dust towards the Dead Sea Valley from convective cold pool outflows in Mesopotamia.

3. Methods and data

In this chapter, the methods and data used for this study are described in detail. In the first section the atmospheric modelling system ICON-ART is introduced. The second section describes the convection permitting model set-up used for the simulation of the severe dust event. The third section provides a description of the observational systems used for validation of the model results.

3.1 The ICON-ART model system

This section gives a short introduction to the ICON-ART modelling system. ICON is a coupled numerical global circulation model which can be used for both weather prediction and climate projections. ART is a modular extension which allows for the treatment of aerosol and reactive trace gas physics in ICON. First an overview of the ICON modelling system and its physics is given, second an overview of the ART module and its capabilities.

3.1.1 ICON

ICON (ICOsahedral Nonhydrostatic) is a non-hydrostatic modelling system developed jointly by the German Weather Service (DWD) and the Max Planck Institute for Meteorology (Zängl et al., 2015). Solving the full three-dimensional non-hydrostatic and compressible Navier-Stokes equations for the global domain already, it can serve as a unified global numerical weather prediction (NWP) model and climate modelling system, enabling seamless prediction from the global to local scale with a unified set of model physics. Its major advantages over previous model generations used at DWD and especially important for atmospheric tracer studies are

1. the exact local mass conservation achieved by solving a prognostic equation for density and
2. the mass-consistent tracer transport achieved by transporting time-averaged mass fluxes computed from the dynamical core and diagnostic reintegration of the mass continuity equation.

ICON allows for flexible local grid refinements (nests) with two-way interactions between the respective grids. Furthermore, it features a better scalability on massively parallel computer architectures. Since January 2015 ICON is used for operational weather forecasting at DWD with a global grid spacing of 13 km.

The basic set of equations which are solved in ICON is given by Zängl et al. (2015) as follows:

$$\frac{\partial v_n}{\partial t} + \frac{\partial K_h}{\partial n} + (\zeta + f)v_t + w \frac{\partial v_n}{\partial z} = -c_p \Theta_v \frac{\partial \Pi}{\partial n} + F(v_n), \quad (3.1)$$

$$\frac{\partial w}{\partial t} + \vec{v}_H \nabla w + w \frac{\partial w}{\partial z} = -c_p \Theta_v \frac{\partial \Pi}{\partial z} - g, \quad (3.2)$$

$$\frac{\partial \rho}{\partial t} + \nabla \cdot (\vec{v} \rho) = 0, \quad (3.3)$$

$$\frac{\partial \Pi}{\partial t} + \frac{R_d}{c_v} \frac{\Pi}{\rho \Theta_v} \nabla \cdot (\vec{v} \rho \Theta_v) = \tilde{Q}, \quad (3.4)$$

$$\text{with } \Pi = \left(\frac{R_d}{p_{00}} \rho \Theta_v \right)^{R_d/c_v}. \quad (3.5)$$

The prognostic variables in ICON are the horizontal wind velocity component normal to the triangle edges v_n , the vertical wind component w , the density ρ and the virtual potential temperature Θ_v . The wind constituents used are the three dimensional wind vector \vec{v} , the horizontal component of the wind vector \vec{v}_H and the tangential wind velocity component v_t , with v_t, v_n, w forming a right-handed coordinate system. Further quantities are the time t , height z , the vertical component of the vorticity ζ , the Coriolis parameter f , the horizontal part of the kinetic energy $K_h = \frac{1}{2}(v_n^2 + v_t^2)$, the Exner function Π , the specific heat capacity of air at constant pressure c_p and at constant volume c_v , the gas constant of dry air R_d , the gravitational acceleration g and the reference pressure p_{00} at 1000 hPa. $\frac{\partial}{\partial n}$ indicates a horizontal, edge-normal derivative, $F(v_n)$ denotes source terms for horizontal momentum and \tilde{Q} diabatic heat-source terms.

ICON uses an unstructured icosahedral-triangular Arakawa C grid on which the physical equations are discretised. For the global domain the initial grid is a spherical icosahedron with 20 faces which is then subsequently refined through so-called root division step, dividing each edge into n equal sections. The sections are then further refined by k bisection steps, each time dividing the edges by two and thereby creating four new triangles within each previous one. The result is a so-called $RnBk$ grid, where the number of cells n_{cell} contained is given by

$$n_{cell} = 20n^2 \cdot 4^k. \quad (3.6)$$

The effective grid spacing $\overline{\Delta x}$ is calculated from the average triangular area of the cells according to

$$\overline{\Delta x} = \sqrt{A_{cell}} = \sqrt{\frac{\pi}{5} \frac{r_e}{n2^k}}, \quad (3.7)$$

where r_e denotes the Earth's radius.

For the physical processes within the model, ICON utilizes a time splitting approach between the dynamical core and tracer advection, as well as physical parametrizations because different numerical stability criteria apply. This is due to the fact that the maximum allowable time step for the air continuity equation solved in the dynamical core is determined by the speed of sound for non-hydrostatical models. In contrast, the maximum time step for the tracer continuity equations is determined by the wind speed. Therefore, a longer time step is used for tracer transport and fast physics parametrizations than for the dynamical core. A third even longer time step can

be used for slow physics parametrizations, which pass tendencies to the dynamical core instead of updating the atmospheric state directly. These are the parametrizations for convection, cloud cover, radiation, non-orographic wave drag and sub-grid scale orographic drag, each of them can be assigned with an individual time step.

For the cloud-microphysics processes a parametrization developed by Seifert and Beheng (2001) is implemented in ICON (Dipankar et al., 2015). The two-moment scheme predicts number and mass concentrations for six different hydro-meteor species. These are cloud droplets, rain drops, cloud ice, snow, graupel and hail. For this parametrization an extension was developed by Rieger (2016), which includes the aerosol effect on cloud formation through using the current, local aerosol mass and number concentrations from ART. It is based on parametrizations published by Phillips et al. (2013) for the heterogeneous ice nucleation spectrum and by Barahona and Nenes (2009) for the cirrus regime with competition between homo- and heterogeneous freezing. The parametrization is not used in this study, as the inclusion of aerosol - cloud microphysics interaction creates a full new set of research questions.

RRTM radiative transfer scheme

In the set-up used in this work, ICON utilizes the Rapid Radiative Transfer Model (RRTM) by Mlawer et al. (1997) as the radiative transfer scheme. For this routine the radiative effect of mineral dust based on the prognostic aerosol concentrations from ART was implemented in ICON. Therefore a short introduction on the RRTM is provided here.

The RRTM calculates shortwave fluxes, longwave fluxes and heating rates throughout the atmosphere for 30 spectral bands in the range from 200 nm up to 1000 μm . It consists of two separate parts, one treating the shortwave wavelengths up to 3846 nm termed RRTM_SW and one treating the long-wave wavelengths from 3076 nm onwards termed RRTM_LW. The spectral band from 3076 nm to 3846 nm is calculated in both models.

The RRTM is a so called broadband correlated k-distribution radiation model, the physical basis is briefly explained here based on the information provided in Mlawer et al. (1997). The correlated-k method is based on the principle of converting the spectrally (with frequency ν) highly variable (due to singular absorption lines by gases) absorption coefficient $k(\nu)$ into a cumulative probability distribution function $k(g)$ for each spectral band j . This mapping $\nu \rightarrow g$ is done by simply reordering the absorption coefficients $k(\nu)$ with the number of occurrence as a cumulative probability g for each spectral band, this is illustrated in figure 3.1. The distribution $k(g)$ is referred to as k-distribution. As detailed in Mlawer et al. (1997) limitations arise for the spectral band-borders in order for the k-distributions to be representative for the spectral band, accordingly the 30 spectral bands were carefully chosen. Each of the 16 longwave spectral bands is divided into 16 intervals in g space giving 256 g points to be evaluated, for a faster RRTM version this was reduced to 140 representative g points. Each of the 14 shortwave spectral bands is divided into 16 intervals in g space as well giving 224 g points to be evaluated, for a faster RRTM version this was reduced to 112 representative g points. Thereby, each subinterval represents a large number of frequencies in the band and absorption characteristics of the main species. The highly resolved

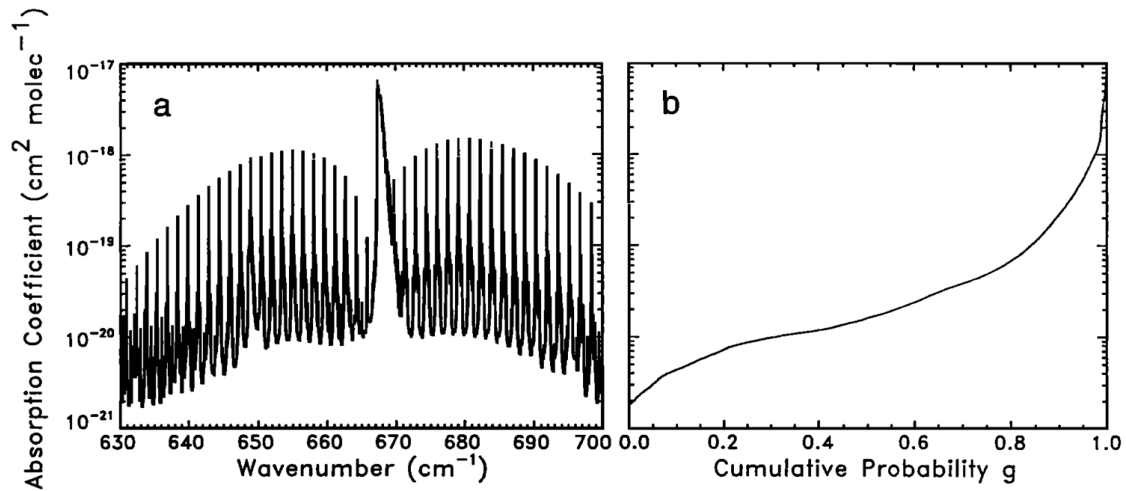


Figure 3.1: Mapping of spectrally highly variable absorption coefficient $k(\nu)$ to cumulative probability distribution function g for a single spectral band in the RRTM_LW. Extracted from Mlawer et al. (1997).

spectral information is lost but the reordering does not have an effect on radiative transfer calculations carried out for the reduced number of g points which are greatly accelerated but still provide the main absorption characteristics.

The radiative transfer calculations can be conducted in a monochromatic way for each subinterval in g space in each spectral band for every layer in the model using a two-stream method, if a linearly varying Planck emission function along the absorbing path and a homogeneous layer with respect to pressure, temperature and species distribution are assumed. For the RRTM this includes a delta two-stream method with SW scattering and an approximation for LW scattering. For each spectral band there is a higher resolution towards $g = 1$ (with 7 intervals between $g = 0.98$ and $g = 1.0$ for every spectral band) as cooling rates are dominated by the centres of the spectral lines (which have the highest absorption coefficients and are therefore at the maximum of the cumulative distribution function towards $g = 1$). For each interval a characteristic value of the absorption coefficient $\kappa_j = k(g)_j$ is used although an error is introduced by this averaging. To include the effect of atmospheric temperature, pressure and minor species such as varying quantities of water vapour (see table 3.1 for a list of included minor species) on radiative transfer in each spectral band the characteristic values of κ_j are parametrized as functions of the full range of relevant atmospheric conditions. For details on this parametrization the reader is referred to section 3.3 in Mlawer et al. (1997). The outgoing radiance calculated for each value of g is then used as the incoming radiance for the same g value of the adjacent layer. This assumes that the mapping $\nu \rightarrow g$ is identical for adjacent layers or, stated differently, that the k distributions in spectral space of adjacent layers are fully correlated. This is why the RRTM is called a correlated k -distribution model. However, in general this assumption is not fulfilled because molecular absorber concentrations, temperature and pressure change from layer to layer giving different spectral absorption characteristics.

The choice of one averaged κ_j (and spectral radiance as well as an effective Planck function) for every g interval and the lack of correlation between k -distributions of adjacent layers are important sources of errors for the correlated k -distribution method. The degree of error introduced thereby depends on the degree of correlation in mapping $\nu \rightarrow g$ for adjacent layers, however it is typically small (Mlawer et al., 1997).

The RRTM code has been implemented in numerous global circulation models and tested extensively for accuracy (Mlawer et al., 1997; Clough et al., 2005) in comparison with line-by-line radiative transfer models. It is also used by the European Centre for Medium-Range Weather Forecasts (ECMWF) in the Integrated Forecasting System (IFS) model (Morcrette et al., 2008). An overview of the RRTM characteristics as used therein is given in table 3.1, as Zängl et al. (2015) state that the implementation of the RRTM in ICON is done analogy to the IFS. For the IFS implementation the RRTM was simplified by avoiding any explicit cloud fraction reference. Therefore, for any given g point clouds fully occupy the respective model layer (for the radiation scheme only). This simplifies calculations of radiative transfer as cloud properties are reduced to modifying three optical parameters introduced in chapter 4, these are the optical thickness τ , the single scatter albedo ω and the asymmetry factor g (not to be confused with the cumulative probability distribution g points).

Table 3.1: Overview of the RRTM characteristics, adapted from Morcrette et al. (2008).

	RRTM_LW	RRTM_SW
Solution of RT equation	two-stream method	two-stream method
Number of spectral intervals	16 (140 g points)	14 (112 g points)
Absorbers	H ₂ O, CO ₂ , O ₃ , CH ₄ , ceN ₂ O, CFC11, CFC12, aerosols	H ₂ O, CO ₂ , O ₃ , CH ₄ , N ₂ O, CFC11, CFC12, aerosols
Spectroscopic database	HITRAN-96	HITRAN-96
Absorption coefficients	from LBLRTM	from LBLRTM
Optical properties of clouds and aerosol	16-band spectral emissivity from τ, g, ω	14-band spectral emissivity from τ, g, ω

3.1.2 The ART module

The Aerosol and Reactive Trace gases (ART) module is an extension of ICON developed at the Institute of Meteorology and Climate Research at the Karlsruhe Institute of Technology. A complete overview of the module is given by Rieger et al. (2015).

In the following, the simulation of mineral dust processes in ART is discussed. ART is capable of simulating a variety of aerosol species, e.g. volcanic ash, sea salt and radioactive substances and their treatment in ART is similar to that of mineral dust. In addition, atmospheric chemistry processes, e.g. two species of very short-lived bromocarbons (CHBr₃ and CH₂Br₂), a linearised ozone chemistry and photolysis are also available in ART. However, as only mineral dust processes are simulated as a part of this work the following description is limited to the same.

For the tracer transport simulations the seamless modelling capabilities of ICON are of crucial importance because inconsistencies in tracer transport and tracer physics at the nest boundaries

can be avoided, which is a major problem for other modelling systems. In ART the coarser domains provide the boundary conditions for the tracer concentrations advected into the finer model domains. However, a two way feedback has not been implemented yet, thereby the finer domain aerosol distribution is not used to update the coarser domain aerosol distribution. Other important features of ICON which are of great value for ART are the exact local mass conservation achieved and the mass-consistent tracer transport.

Mineral dust in ART

The size distribution of mineral dust is represented by three modes in ART. For each mode the integral values of specific number and mass are the prognostic variables. The distribution of specific number and mass with particle size during transport is described using log-normal distributions for each mode with a diagnostic median diameter and constant geometric standard deviation as parameters. In the following, the basic formulas used for the description of mineral dust in ART are introduced in accordance with Rieger et al. (2015). The barycentric mean of a variable Ψ (denoted by a $\widehat{\Psi}$) gives its value with respect to the density of air ρ ,

$$\widehat{\Psi} = \frac{\overline{\rho\Psi}}{\overline{\rho}}. \quad (3.8)$$

The over-line denotes Reynolds averaged variables. Using this relation the prognostic barycentric variables of the (mass-) specific number $\Psi_{0,l}$ and mass mixing ratio $\Psi_{3,l}$ of mode l are given as

$$\widehat{\Psi}_{0,l} = \frac{\overline{\rho\Psi_{0,l}}}{\overline{\rho}} = \frac{\overline{\rho\frac{N_l}{\rho}}}{\overline{\rho}} = \frac{\overline{N_l}}{\overline{\rho}}, \quad (3.9)$$

and

$$\widehat{\Psi}_{3,l} = \frac{\overline{\rho\Psi_{3,l}}}{\overline{\rho}} = \frac{\overline{\rho\frac{M_l}{\rho}}}{\overline{\rho}} = \frac{\overline{M_l}}{\overline{\rho}} \quad (3.10)$$

with respect to the number concentration N_l and mass concentration M_l . The log-normal distributions allow for calculation of the specific number $\widehat{\psi}_{0,l}$ of mineral dust at diameter d_p according to:

$$\widehat{\psi}_{0,l}(\ln d_p) = \frac{d\widehat{\Psi}_{0,l}}{d\ln d_p} = \frac{\widehat{\Psi}_{0,l}}{\sqrt{2\pi\ln\sigma_l}} \cdot \exp\left(-\frac{(\ln d_p - \ln \bar{d}_{0,l})^2}{2\ln^2\sigma_l}\right). \quad (3.11)$$

The factors determining the shape of the log-normal distribution of mode l are the median diameter $\bar{d}_{0,l}$ of the number distribution and the standard deviation σ_l .

In a similar way the mass mixing ratio $\widehat{\psi}_{3,l}$ with diameter d_p is given by

$$\widehat{\psi}_{3,l}(\ln d_p) = \frac{d\widehat{\Psi}_{3,l}}{d\ln d_p} = \frac{\widehat{\Psi}_{3,l}}{\sqrt{2\pi\ln\sigma_l}} \cdot \exp\left(-\frac{(\ln d_p - \ln \bar{d}_{3,l})^2}{2\ln^2\sigma_l}\right). \quad (3.12)$$

Hereby $\bar{d}_{3,l}$ denotes the median diameter of the mass distribution. As the standard deviation is kept constant during transport the diagnosed median diameters of number and mass concentration

Table 3.2: Initial median diameter of the number distribution $\bar{d}_{0,l}$ and of the mass distribution $\bar{d}_{3,l}$ and standard deviation σ_l for mineral dust modes used in ICON-ART.

	Mode A	Mode B	Mode C
$\bar{d}_{0,l} / \mu\text{m}$	0.644	3.453	8.671
$\bar{d}_{3,l} / \mu\text{m}$	1.5	6.7	14.2
σ_l	1.7	1.6	1.5

are always directly related to each other through

$$\ln \bar{d}_{3,l} = \ln \bar{d}_{0,l} + 3 \cdot \ln^2 \sigma_l. \quad (3.13)$$

The median diameter can be diagnosed from the prognostic variables using

$$\bar{d}_{0,l} = \sqrt[3]{\frac{\widehat{\Psi}_{3,l}}{\frac{\pi}{6} \rho_p \exp\left(\frac{9}{2} \ln^2 \sigma_l\right) \widehat{\Psi}_{0,l}}}, \quad (3.14)$$

where ρ_p denotes the density of the mineral dust particles given as 2500 kg m^{-3} . An overview of the initial median diameter and constant standard deviation used for each mineral dust mode is given in table 3.2. In order to investigate the behaviour of the median dust diameter during transport in section 5.3, a mass-weighted, column averaged median diameter $\bar{D}_{3,l}$ is calculated and normalized with respect to the initial emission diameter $\bar{d}_{3,l \text{ ini}}$ according to the following formula:

$$\bar{D}_{3,l} = \sum \frac{\bar{d}_{3,l}}{\bar{d}_{3,l \text{ ini}}} \cdot \frac{\bar{M}_l}{\sum \bar{M}_l}. \quad (3.15)$$

Hereby, the summation sign denotes averaging over the full model column.

The distributions of specific number and mass-mixing ratio can also be related to each other through

$$\widehat{\psi}_{3,l}(d_p) = \rho_p \left[\frac{\pi}{6} d_p^3 \right] \widehat{\psi}_{0,l}(d_p), \quad (3.16)$$

using this relation the mass-mixing ratio can be calculated by integration from the number distribution:

$$\widehat{\Psi}_{3,l} = \int_0^\infty \widehat{\psi}_{3,l}(d_p) dd_p = \int_0^\infty \rho_p \left[\frac{\pi}{6} d_p^3 \right] \widehat{\psi}_{0,l}(d_p) dd_p. \quad (3.17)$$

The prognostic equation for the spatial and temporal evolution of the specific number, which is discretized and solved in order to simulate the transport of mineral dust, reads as follows according to Rieger et al. (2015):

$$\frac{\partial (\widehat{\rho\Psi}_{0,l})}{\partial t} = -\nabla \cdot (\widehat{v\rho\Psi}_{0,l}) - \nabla \cdot (\overline{\rho\bar{v}''\Psi''_{0,l}}) - \frac{\partial}{\partial z} \cdot (v_{\text{sed } 0,l}\widehat{\rho\Psi}_{0,l}) - W_{0,l} + E_{0,l}. \quad (3.18)$$

Hereby, $-\nabla \cdot (\overline{\rho\bar{v}''\Psi''_{0,l}})$ denotes the turbulent flux in specific number of mode l . Variables extended by inverted commas Ψ'' represent deviations from the barycentric mean, $\Psi'' = \Psi - \widehat{\Psi}$. Furthermore $v_{\text{sed } 0,l}$ is the sedimentation velocity of the specific number distribution. $W_{0,l}$ is the loss-rate caused by wet deposition and $E_{0,l}$ the emission rate of mineral dust. The prognostic equation for the specific mass distribution is equal to that of the specific number in ART as condensation and coagulation of mineral dust particles is not yet implemented. It can be obtained by substituting the index $_{0,l}$ with $_{3,l}$ and is therefore not displayed again.

As a result, the processes which affect mineral dust number and/or mass concentrations in ART are sedimentation, dry deposition and wet deposition due to washout. Sedimentation of mineral dust is included through simulating a constantly downward directed vertical advection with a size-dependent sedimentation velocity. Because larger particles have a greater sedimentation velocity and therefore settle faster, the size distribution shifts towards smaller particles during transport. Dry deposition is connected to the one dimensional prognostic turbulent kinetic energy turbulence scheme in ICON by Raschendorfer (2001), which is adapted to treat vertical diffusion of mineral dust as a tracer. Washout of mineral dust due to rain below clouds is parametrized as a function of the particle size distribution and the size distribution of rain droplets depending on height. Here a problem might arise for evaporating rain below clouds, as mineral dust, which is only temporarily scavenged by rain drops which evaporate again before reaching the surface, is lost to the model but not in reality. In cloud scavenging of mineral dust particles which serve as condensation nuclei is not yet implemented in ART, however the number of particles undergoing this process is very small.

The prognostic variables of specific number and mass mixing ratio can develop independently from each other as some parametrizations influence the distributions differently, e.g. the sedimentation velocities for number and mass distributions are different. This is why specific number concentration and mixing ratio are both prognostic variables in ART, leading to a change in median diameter during transport as at all times both distributions are linked through equation 3.13.

Emission of mineral dust

Mineral dust emission occurs when the cohesion forces holding the mineral dust particles to the ground are overcome. However, small particles in the range from 1 – 20 μm which are most suitable for long-range transport are tightly bound by strong adhesive forces which can seldom be overcome by the aerodynamic force of wind alone (Knippertz and Stuut, 2014). Nevertheless, emission of these particles is possible in great quantities due to a process called saltation bombardment. In this process larger particles (diameter $\approx 70 - 1000 \mu\text{m}$) are lifted first by aerodynamic forces because their adhesive force is weaker and aerodynamic resistance greater, sending

them on a ballistic trajectory. The impaction of these particles can release enough kinetic energy to overcome the strong adhesive force of smaller particles. Alternatively, the larger particles can break-down upon impact, leading to the emission of smaller particles as well. Because the settling velocity of finer particles is smaller than the vertical wind velocity they can be uplifted further in the turbulent planetary boundary layer and transported long-range. The processes described here are depicted in figure 3.2 which is adapted from Shao et al. (2011b).

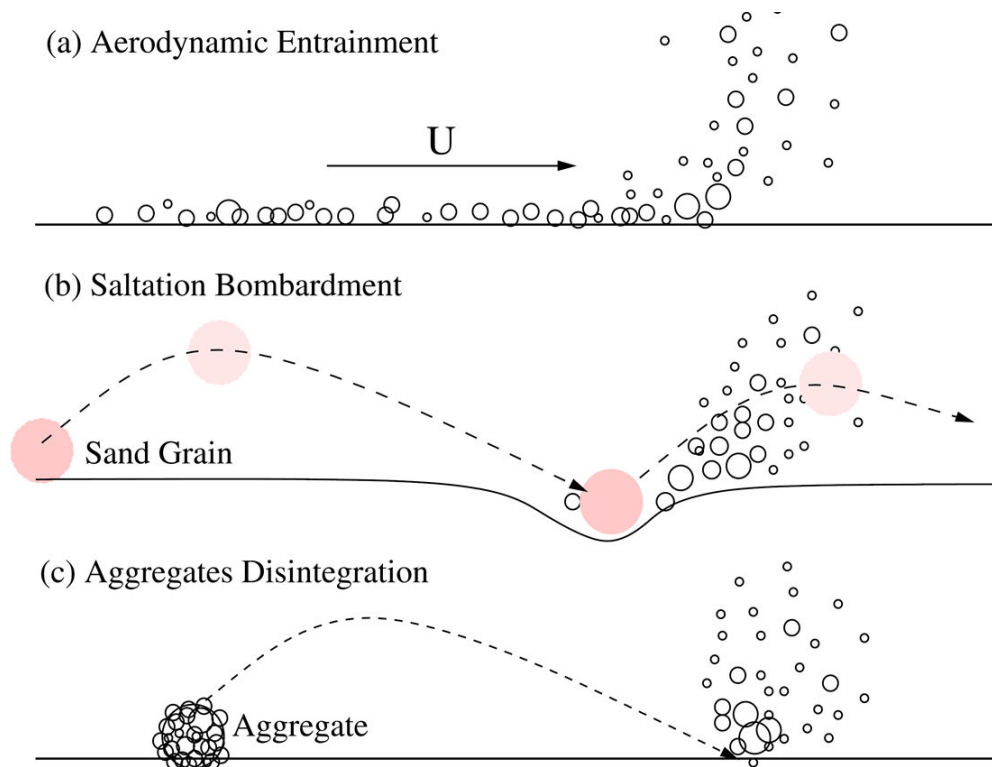


Figure 3.2: Dust emitting processes according to Shao et al. (2011b). Shown are (a) aerodynamic uplift of small particles, (b) ejection due to saltation bombardment and (c) release due to disintegration of larger particles.

The horizontal saltation flux and thereby dust emission scale with the cube of the friction velocity u_* . This highly non-linear relationship again demonstrates the need for high-resolution modelling in order to represent the wind field correctly (Knippertz and Stuut, 2014, and references therein). Resulting from the saltation bombardment theory a size dependent threshold friction velocity u_{*t} exists, above which dust emission can occur, although the size dependency of emissions is questioned by Kok (2011). Investigating measurements from various studies they report that the size distribution of mineral dust emission does not depend on wind speed. A global minimum threshold velocity $u_{*t,min}$ exists below which no dust at all can occur independent of size distribution. The threshold friction velocity is influenced by surface roughness and soil moisture content.

The scheme used for emission of mineral dust in ART is described in Rieger (2016). It is based on an emission scheme introduced by Vogel et al. (2006). Compared to the original version three improvements were implemented, these are (1) the global availability of soil properties (size

distribution, residual soil moisture), (2) accounting for the soil dispersion state, and (3) a tile approach used to account for soil type heterogeneity at coarse resolutions. For the equations used the reader is referred to the work by Rieger (2016). The scheme parametrizes the threshold friction velocity for dust emission according to Shao and Lu (2000), who base their description on a physical balance between aerodynamic drag and lift causing upward directed forces and cohesion and gravity causing downward directed forces on particles. The effect of surface roughness and soil moisture are accounted for through parametrizations by Raupach et al. (1993) and Fécan et al. (1999) respectively, which modify the threshold friction velocity. Higher values of surface roughness and soil moisture lead to a higher threshold friction velocity needed for dust emissions, as they decrease the momentum available for eroding the surface or strengthen the retaining forces, respectively.

Utilizing the threshold friction velocity u_{*t} and the cubed friction velocity u_*^3 at every grid point the horizontal saltation flux is calculated according to a parametrization developed by White (1979). This parametrization contains a tuning parameter C_{white} which can be used to adjust the horizontal saltation flux to measurements.

From the horizontal saltation flux a vertical saltation flux of dust particles is then calculated according to parametrization suggested by Alfaro and Gomes (2001). Their approach is based on the assumption that the cohesive force retaining the particles has to be surmounted through the impaction of larger particles converting their kinetic energy. The integration over the vertical saltation flux gives the total emission flux for every mode, for which additionally the erosion state of the soil and the fraction of erodible soil are taken into account.

The fraction of erodible soil is determined assuming that certain land uses classes from the GlobCover2000 dataset (Arino et al., 2008) contribute to mineral dust emission whereas others do not, with snow generally prohibiting emissions. The land use classes which can contribute to emission are regions with sparse vegetation, bare areas, closed to open grass- and shrub-lands, furthermore mosaic forest/grassland and shrub-land.

The regional distribution of soil types used for dust emission in ART is taken from the HWSD dataset with a resolution of 30 arc seconds (Nachtergaele and Batjes, 2012). The dominant soil types in the study region are shown in figure 2.10. In order to retain the high spatial resolution of the dataset for ART a tile approach is used for calculating dust emissions. The tile approach calculates the overall emission in every grid box as a weighted average of the emissions from different soil types based on their fractional coverage of the grid box. The 13 soil types are assigned with a specific clay content determining the minimal residual soil moisture content (Rieger, 2016). Each soil type from the HWSD dataset is attributed with two limiting particle size number distributions, minimal and maximal dispersed, from up to four modes according to a study conducted by Shao et al. (2010). The size distribution describing the minimally dispersed state is used at low wind speeds and therefore describes weak erosion. The maximally dispersed distribution describes strong erosive conditions during high wind speeds when larger particles compounds break free and lead to higher emissions of small particles. At intermediate conditions a size distribution between the two limiting distributions is chosen as a function of friction velocity (Rieger, 2016).

3.2 Model set-up

In this study ICON-ART is run in a set-up with one global domain and four nests, with two-way feedback for the meteorological parameters enabled throughout all domains. The horizontal extent of the nests is shown in figure 3.3. Each domain presents a stand-alone model run which obtains its lateral boundary conditions from the coarser domain. For the global domain an R2B6 grid is used, this corresponds to an effective grid spacing of 40 km. For every nest, the grid point distance is halved, thereby ending at R2B10 with an effective grid spacing of 2.5 km. The resolution of a model is in the region of five times the grid point spacing, consequently features as small as 12.5 km can be resolved in the model, this is sufficient for the Dead Sea Rift Valley (see also figure 2.6).

On the global domain the model consists of 90 levels extending up to the mesosphere, with the lowest level being at 20 m and the highest level at 75 km. For the nests the simulated atmosphere extends into the stratosphere up to 22.5 km containing 60 vertical levels. To achieve numerical stability the advective time step is set to 216 seconds for the global domain. ICON performs a sub-stepping for the dynamical core with a factor of 4 and the advective time step is halved for every nest. The parametrization for radiation is called every 1728 s for the global grid and every 288 s for the finest nest, the convection parametrization is called every 576 s for all nests except the finest. In order to realistically represent the moist, deep convection producing the CPO, a convection permitting model resolution is required. A grid spacing of 2.5 km is generally assumed to be sufficient to permit the development of convection in a non-hydrostatic model, therefore the convection parametrization is switched off for the finest grid. For the cloud micro-physical processes a the two-moment cloud scheme is used (see section 3.1.1), as this was found to lead to more realistic features of the meso-scale organized convection.

Due to an instability of the lake model FLAKE when initializing at noon, a constant sea surface temperature of 33°C is prescribed for the Dead Sea. This does not allow for development of a diurnal cycle of the lake surface temperature which can have an impact on the development of local wind systems.

The HWSD soil dataset which is important for dust emission (see section 3.1.2) contains a large undefined region for soil properties on the Sinai Peninsula, this was modified to a mixture of

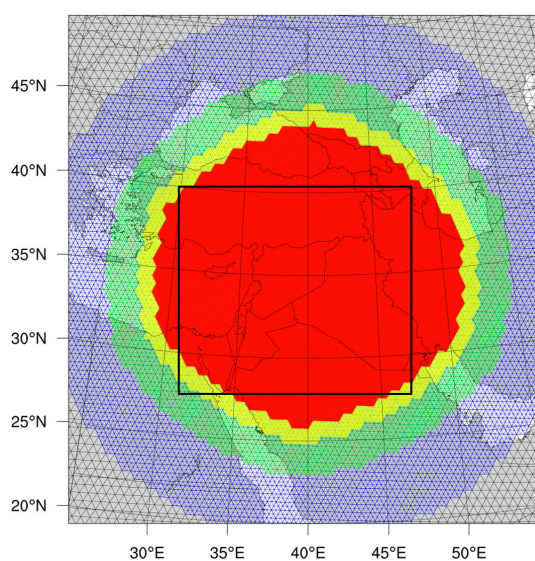


Figure 3.3: Grid and nesting structure used for the model setup, from R2B6 (black, global) to R2B10 (red). The black frame shows the region for subsequent plots in the analysis part.

80% loam and 20% sand in similarity with soil properties of the surrounding regions in order to avoid unrealistic gradients. The resulting dust emissions on the Sinai Peninsula are of realistic magnitude, however their influence on the EM and Dead Sea Valley is of negligible influence due to a strong southward transport in this region.

In the ART module the horizontal saltation flux tuning parameter C_{white} is set to 1.4 (see section 3.1.2).

ICON-ART is initialized with analysis fields from the IFS of the ECMWF. The IFS data is averaged and interpolated to the needed grid spacing for all domains with tools provided the DWD. A limitation with initializing from the IFS analysis datasets is that the IFS has a horizontal grid spacing of approximately 13 km and is therefore non convection-permitting. Thus, when re-initializing ICON-ART with the current meteorological fields any convection which develops in ICON-ART is terminated. The re-development and organization of convection in ICON-ART takes approximately six hours, during this time the advantages of a convection permitting simulation are compromised and the meteorological situation is not captured in the best possible way. Consequently, the times at which a re-initialization of the meteorological fields is performed have to be chosen with care, this is discussed below. The IFS initialization data for soil moisture was modified in a region along the Syrian-Iraqi border which showed unrealistically high soil moisture values and spatial patterns without preceding rain or changes in soil properties. Therefore, in a region from $37.5^{\circ}\text{N} - 41.5^{\circ}\text{N}$ and $32.5^{\circ}\text{E} - 35^{\circ}\text{E}$ the soil moisture index in the four layers provided by the IFS is set to the average value of the region between $36.5^{\circ}\text{N} - 38^{\circ}\text{N}$ and $32^{\circ}\text{E} - 34^{\circ}\text{E}$ which represents the soil moisture conditions in the region more realistically. The region modified is an important dust source region in the CPO and emission fluxes for mineral dust increased due to the reduction of the soil moisture content.

For investigation of the dust radiative effect two simulations are performed. The first is the simulation including the on-line radiation interaction with mineral dust from ART which is called 'ARI' (aerosol radiation interaction) in the following. The second is a simulation in which the mineral dust concentrations are multiplied by zero in the ART routine calculating the radiative effect of dust. This simulation is called 'CTRL' (control) in the following, it contains no mineral dust influence on radiation at all. In this study only the mineral dust radiation interaction is simulated on-line by ART, for all other aerosols the default climatologies are used in all runs.

The ART mineral dust aerosol concentrations are passed on to the next run whenever a reinitialization of the meteorological fields from an IFS analysis is performed. No assimilation of mineral dust concentrations from observations takes place. Hence, the runs are performed as free runs for the mineral dust concentrations with a frequent update of the meteorological background conditions from IFS analysis in order to benefit from the data assimilation performed therein. The points in time chosen for initialization of ICON-ART with IFS analysis are shown in figure 3.4. A two week spin-up simulation is performed starting on 23rd August 2015 in order to achieve a realistic background concentration for mineral dust on the global domain. Another reinitialization from an IFS analysis is performed at 00 UTC 04 September 2015 to obtain a realistic background concentration of mineral dust in the finer domains for the simulations starting at 18 UTC 05 September. From 00 UTC 06 September onwards, a multitude of partially overlapping

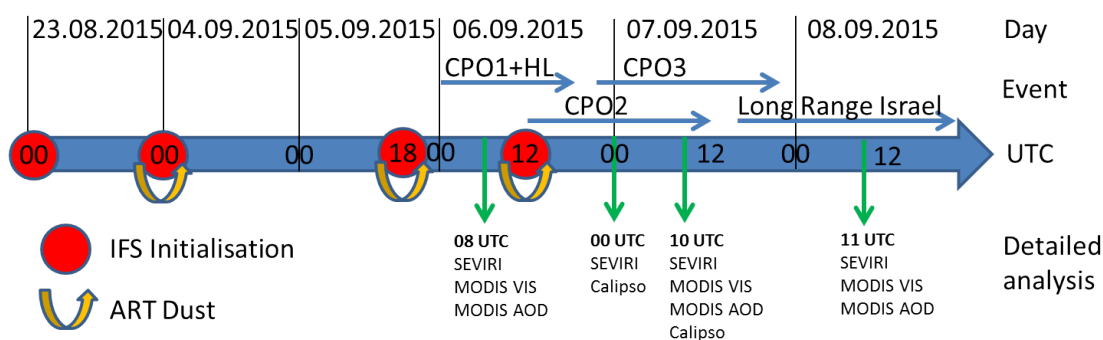


Figure 3.4: Overview of the initialization and analysis scheme used in this study. ICON-ART is initialized with IFS at the times denoted by red points. ART dust fields are transferred to the next run, creating a continuous dust simulation denoted by yellow arrows. The course of events is denoted by blue time arrows with event names as discussed in section 5.2 and shown in figure 5.2. Points in time at which an extensive analysis and comparison to observations is conducted are denoted by green arrows.

events take place which need to be simulated correctly in order to obtain a realistic dust distribution in the EM. Therefore, the time chosen for initialization is of crucial importance due to the aforementioned termination of organized convection. The settings used greatly influence the timing of convection and thereby the CPO structure. Various options were examined, the times chosen for initialization are 18 UTC 05 September and 12 UTC 06 September.

3.3 Observations

In chapter 5 the model results are compared to measurements from a variety of different observational systems. For the validation of the simulated horizontal and vertical distribution of mineral dust satellite measurements are used, which are introduced in this section. Furthermore, in order to validate the amount of dust which is transported long range, the model results are compared to observations in Israel. All systems used are introduced in the next sections.

SEVIRI

For validation of the cloud conditions and dust transport pathways the Spinning Enhanced Visual and Infrared Imager (SEVIRI) dust RGB product is used. It is available every 15 minutes for the investigated period from the European Organisation for the Exploitation of Meteorological Satellites (EUMETSAT). The product uses brightness temperature data measured by the geostationary Meteosat Second Generation Meteosat-10 satellite. In order to obtain the dust product, spectral regions sensitive to characteristic absorbers are colour coded using different colour-maps as described in Lensky and Rosenfeld (2008). The brightness temperature measured by the SEVIRI 10.8 μm channel is used as an indicator for cloud top and surface temperature and mapped towards blue colours. Vertically mighty clouds are mapped towards reddish tones and cirrus clouds

towards black using the difference in brightness temperature measured at $12.0\ \mu\text{m}$ and $10.8\ \mu\text{m}$ channels which indicates the opacity of clouds. According to Lensky and Rosenfeld (2008) the emissivity of small mineral quartz particles ($0 - 45\ \mu\text{m}$) is large for the $8.7\ \mu\text{m}$ channel, in contrast the emissivity of large mineral dust particles ($125 - 500\ \mu\text{m}$) is low for this channel. Thus, the difference in brightness temperatures between $10.8\ \mu\text{m}$ and $8.7\ \mu\text{m}$ is mapped towards pink values and used as an indicator for the amount of small dust particles transported in the atmosphere, clearly distinguishing it from the desert sand background. As Brindley et al. (2012) discuss, a high amount of integrated column water vapour can prevent the detection of uplifted dust which can pose a problem in CPOs due to the high amount of water contained in the air mass.

MODIS

A second instrument used for validation of ICON-ART model results is the Moderate Resolution Imaging Spectroradiometer (MODIS) which flies on-board of two satellites, Aqua and Terra. Terra MODIS and Aqua MODIS are polar orbiting instruments and therefore able to view the EM region twice a day only. However, they acquire a wealth of data in 36 spectral bands at high spatial resolution at every overpass. For the analysis, two MODIS products are used, the first being satellite images for the visible part of the spectrum to identify cloud and transport structure. The second product used is the aerosol optical depth over land at $550\ \text{nm}$ from the MODIS daily Level 2 data which is retrieved using the Deep Blue 2 (DB2) algorithm in Collection 6 at a $10 \times 10\ \text{km}$ resolution at nadir (Hsu et al., 2004; Levy and Hsu, 2015). It is used for the quantitative evaluation of the simulated mineral dust optical depth magnitude. Because MODIS detects absorption due to all aerosols and not only mineral dust an aerosol optical depth offset of 0.3 is subtracted from the MODIS data in order to make the scales comparable to model output and mineral dust features more visible. As a result the MODIS measurements are treated as pure dust measurements, however, one should bear in mind the difference.

CALIOP

The systems discussed above provide column integrated values of the aerosol distribution, but for the transport processes the vertical distribution of the dust column is also of great importance. Aqua MODIS orbits the Earth as a part of a bigger satellite group termed the afternoon satellite constellation (A-Train) consisting of five satellites flying in close proximity. At two points in time the developing event is passed directly overhead by the A-train. Another instrument from the A-train used in this study is the Cloud-Aerosol Lidar with Orthogonal Polarization (CALIOP) which flies on-board the CALIPSO satellite. CALIOP measures the atmospheric backscatter signal at $532\ \text{nm}$ and $1064\ \text{nm}$ wavelengths and polarization of the backscattered signal at $532\ \text{nm}$. Along the satellite track this system provides vertically resolved profiles of the total attenuated backscatter in the atmosphere with a $30\ \text{m}$ vertical resolution and a profile spacing of $333\ \text{m}$ (Winker et al., 2007). For the analysis shown 25 profiles are averaged horizontally in order to reduce the noise. As under cloud-free conditions mineral dust is the dominant scatterer in the region, the backscatter Level 1 Version 3-30 data from CALIOP is used to investigate the modelled vertical

distribution of mineral dust. Using the polarization information, the satellite data also provides a vertical feature mask which assigns the measured signal to different scatterers such as mineral dust and clouds. In this work, the vertical feature mask classification is obtained from Level 2 Validation stage 1 Version 3-30 data with 5 km horizontal resolution.

Environmental station data

In order to investigate the long-range transport of dust to the southern EM, a comparison with surface observations in the region is conducted. The validation of model results and circulation phenomena is done with the help of three meteorological stations at different elevations in the Golan Heights region because the dust plume interacts strongly with the topography in the Dead Sea Rift Valley. The locations and names of the stations used are marked in figure 5.18. The highest station is Merom Golan at an elevation of 950 m, followed by Gamla at 405 m and Zemah at the valley bottom at -200 m. For the provision of an extensive and high-quality dataset of all meteorological stations in Israel P. Khain and Y. Levi from the Israeli Meteorological Service are gratefully acknowledged.

Furthermore, the simulated dust concentrations are compared to measurements from three environmental stations in Israel which measure PM10 concentrations. The selected stations are Afula, Jerusalem (Bar Ilan) and Ashdod (Nir Galim) as they all show individual dust concentration characteristics during the event (see figure 5.18 for a map of the station locations). For the provision of an extensive and high-quality dataset of all environmental stations in Israel P. Khain and Y. Levi from the Israeli Meteorological Service are gratefully acknowledged again.

AERONET

A comparison of the modelled DOD in Israel is conducted with measurements from the Aerosol Robotic Network (AERONET) station in Sede Boker. AERONET is a world-wide sun-photometer network established by NASA to measure aerosol optical properties (Holben et al., 1998). From ground-based, remote sensing measurements of sun and sky radiances the aerosol optical properties are calculated using inverse retrieval algorithms (Dubovik et al., 2000; O'Neill et al., 2003). For the Sede Boker AERONET data A. Karnieli is acknowledged, this study uses AERONET Version 2 Direct Sun Algorithm Level 2 data.

4. Implementation of the mineral dust radiative effect in ICON-ART

In this section the interaction between mineral dust and radiation within ICON-ART is outlined. It is now possible to calculate the radiative effect of the current, local mineral dust concentration from ART at every grid point and time step in ICON.

The implementation in ICON-ART is done following the work of Stanelle (2008) and Lundgren (2011), who describe the implementation of the radiative effect of mineral dust and sea salt aerosol, respectively, within COSMO-ART. However, in this work a new code to conduct the Mie calculations is used and new, size dependent optical properties are introduced. The new parametrization is able to account for changes in median diameter of the aerosol modes during transport.

To account for the influence of mineral dust on radiation the optical properties of mineral dust are determined off-line once with the help of Mie calculations using the complex refractive index of mineral dust. The local radiative transfer parameters needed for the RRTM are then calculated on-line within ICON-ART through multiplication of the mass-specific dust optical properties with the current dust mass concentration from ART. The altered radiative transfer parameters are then used by the RRTM radiation scheme, thereby accounting for the local mineral dust effect on radiation. The changed radiative fluxes from the RRTM scheme feed back on the meteorological conditions, which themselves can influence the dust processes again.

4.1 Radiative transfer

In the following a short description of physical variables used for the description of radiative transfer through a layer is given according to Petty (2006).

The amount of extinction caused by a single particle can be expressed through its extinction cross-section σ_e which is analogous to the shadow a particle casts in incident radiation and thereby has the dimension of area. Relating this quantity to the cross sectional area $A_{pc} = \pi r^2$ of the particle itself we can define the extinction efficiency Q_e as

$$Q_e = \frac{\sigma_e}{A_{pc}}. \quad (4.1)$$

It describes the ability of a particle to cause extinction in relation to its area. Using geometric

optics one might assume that Q_e can only range from zero to one because a particle can only cast a shadow as big as itself. However, when dealing with extinction in the Mie-region where particles are in the same size range as the wavelength of incident radiation the extinction efficiency can reach values above five.

When dealing with a number of particles along the light path described by their number concentration N with dimension of particles per unit volume, we can calculate the extinction caused by these particles per unit length through

$$\beta_e = \sigma_e N. \quad (4.2)$$

The volume extinction coefficient β_e has dimensions of inverse length. The quantity $1/\beta_e$ gives the length required to reduce the radiation intensity to $e^{-1} \approx 37\%$ of its original value. For calculation of optical depths from aerosol concentrations it is desirable to express the extinction coefficient not in reference to a distance between points but in reference to the mass contained between the points. This can be achieved through relating the volume extinction coefficient β_e to the density of the material ρ causing extinction,

$$\beta_e = \rho k_e. \quad (4.3)$$

The mass extinction coefficient k_e has dimensions of area per unit mass and it can be interpreted as an extinction cross-section per unit mass. The mass extinction coefficient is constant for aerosols in the atmosphere irrespective of concentration.

When dealing with a mixture of components l the extinction coefficients can be handled additively. This means that the total volume extinction coefficients are equal to the sums of the corresponding coefficients for the individual components (Petty, 2006):

$$\beta_e = \sum_l \beta_{e,l} = \sum_l \rho_l k_{e,l}. \quad (4.4)$$

Using the volume extinction coefficient we can describe radiative transfer through a layer using the Lambert-Beer law. In general, the intensity of radiation transmitted from points z_1 to point z_2 ($z_2 \geq z_1$) given as $I_\lambda(z_1)$ and $I_\lambda(z_2)$ will decay exponentially along the path according to:

$$I_\lambda(z_2) = I_\lambda(z_1) \exp \left\{ - \int_{z_1}^{z_2} \beta_e(z) dz \right\} = I_{\lambda,0} \exp \{ -\tau(z_1, z_2) \}, \quad (4.5)$$

where β_e is the volume extinction coefficient along the path between z_1 and z_2 . The dimensionless, integral quantity $\tau_e(z_1, z_2)$ given as

$$\tau_e(z_1, z_2) = \int_{z_1}^{z_2} \beta_e(z) dz, \quad (4.6)$$

is called the optical depth (also optical thickness) between points z_1 and z_2 . In analogy to the statement above, an optical depth of 1 between z_1 and z_2 corresponds to a reduction of radiation intensity I_λ to $e^{-1} \approx 37\%$ of its incident quantity. If the extinction coefficient between the points

is constant the equation simplifies to:

$$\tau_e(z_1, z_2) = \beta_e \cdot (z_2 - z_1). \quad (4.7)$$

When substituting β_e with the mass extinction coefficient it is apparent that the optical depth is then independent of the length over which an amount of mass causing extinction is distributed but instead related to the amount of mass contained.

Extinction of radiation along the light path can be caused through two mechanisms, these are absorption and scattering of radiation. The first causes conversion of the radiative energy to heat or chemical energy, the latter redirects the radiation out of the original light path. As both effects are of importance in the atmosphere we need a more detailed description of radiative transfer through a layer including the effect of scattering.

We can express the extinction coefficient as a sum of an absorption coefficient and a scattering coefficient:

$$\beta_e = \beta_a + \beta_s. \quad (4.8)$$

The same can be done for the mass extinction coefficient, the extinction cross-section and the extinction efficiency. In order to have a measure for the relative contribution of absorption and scattering to extinction we can define the single scattering albedo as

$$\omega = \frac{\beta_s}{\beta_e} = \frac{k_s}{k_e} = \frac{\sigma_s}{\sigma_e} = \frac{\beta_s}{\beta_s + \beta_a}. \quad (4.9)$$

A single scattering albedo of one corresponds to a purely scattering medium, whereas a single scattering albedo of zero corresponds to a purely absorbing medium. No conclusion on the total amount of extinction can be drawn from the single scattering albedo, however it can be used to estimate the amount of heating caused by absorption of radiation versus scattering of radiation. The single scattering albedo of a mixture of substances can be calculated by first finding the combined β_s and β_e , and then taking the ratio as stated above (Petty, 2006).

Scattering of radiation arriving from any direction can occur into any direction depending on the wavelength of the incident radiation and the scattering particle characteristics. Therefore, when considering radiative transfer through a layer with multiple scattering we have to consider the effect of radiation being scattered out of the light path and *into* the light path again. These complex scattering characteristics can be expressed through a so called scattering phase function which can be viewed as a probability density. It describes the probability of a photon arriving from any direction being scattered into any direction and is typically complex and not easily describable by mathematical means.

As this description would be too computationally expensive in numerical weather modelling azimuthal isotropic scattering is assumed because we are not interested in angular resolved intensities but only the hemispheric fluxes. This is also called two-stream approximation and leads to the details of the phase function being irrelevant. Thereby one is only interested in the proportion of forward versus backward scattered photons into the two hemispheres. This information is

contained in the asymmetry parameter g , with

$$-1 \leq g \leq 1. \quad (4.10)$$

An asymmetry parameter of $g = 1$ implies purely forward scattering, with decreasing asymmetry parameter the backward scattered fraction of photons becomes larger. An asymmetry parameter of $g = 0$ is obtained when scattering into the forward and backward hemisphere occur with equal probability. A value of $g = -1$ denotes reversal a of the photon travel direction with every scattering process, however this is physically unlikely.

Radiative transfer through a layer is described with the help of the three parameters described above in the RRTM radiation scheme as it uses a δ -two stream method (which is not detailed further here as this would be beyond the scope of this work, for details on this method see e.g. Petty, 2006, chapter 13). The first parameter is the extinction optical thickness per layer τ_e , which describes the amount of radiation that becomes extinct due to scattering out of the light path or absorption on the way through the layer. The second parameter is the single scattering albedo ω which describes the probability of a single photon being absorbed during a photon-particle interaction process. The last parameter is the asymmetry parameter g which describes the proportion of forward scattering compared to that of backward scattering.

In order to obtain the optical depth due to mineral dust at every grid point we need to calculate the mass-specific extinction coefficient of mineral dust using Mie theory and then multiply it with the local prognostic mass-mixing ratio from ART. The derivation of the other local radiative transfer parameters is done accordingly. The details of the implementation of the mineral dust effect on radiative transfer within ICON-ART are explained in the next section 4.2 whereas the calculation of mineral dust optical properties is outlined in section 4.3.

4.2 Mineral dust radiative effect in ICON-ART

The basic outline of the mineral dust-radiation interaction in ICON-ART is shown in figure 4.1. In this section more detailed insight is given including the physical equations used in the ICON-ART routine to include the aerosol effect on radiation for the RRTM. The implementation was done in collaboration with C. Walter and D. Rieger and it allows for consideration of the radiative effect from various aerosols. C. Walter has implemented the radiative effect of volcanic ash using the same routine.

The ART aerosol radiation routine is called at every time step at which the ICON radiation routine is called. It provides three optical parameters for 30 wavebands j as output to the subsequently called RRTM radiation scheme. These are the optical depth $\tau_{e,j}^*$, the single scattering albedo ω_j^* and the asymmetry parameter g_j^* , with the asterisk denoting values per model layer. The parameters returned are the combined values from the local ART aerosol concentration plus the Tegen climatology, the latter being used only for aerosol species not simulated in ART.

In order to calculate the local radiative transfer parameters the ART routine needs the mass extinction coefficient $k_{e,l,j}$, the single scattering albedo $\omega_{l,j}$ and the asymmetry parameter $g_{l,j}$

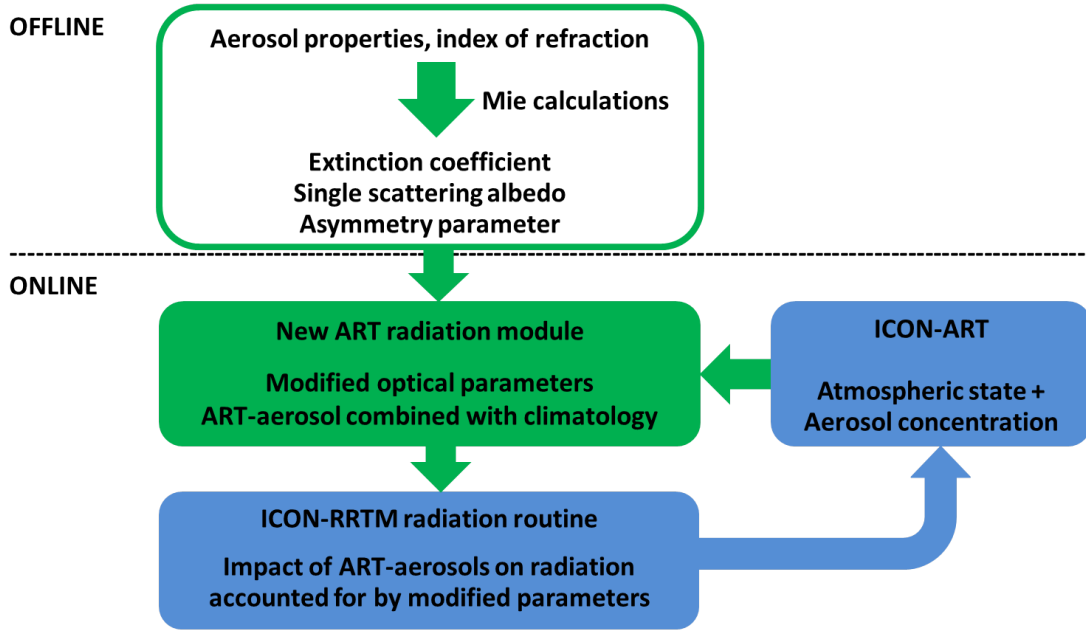


Figure 4.1: Schematic depiction of new modules in green and existing routines in blue

for every mode l and every waveband j . These are obtained using Mie calculations which are explained in the next section. Together with the local aerosol mass mixing ratios from ART and air density ρ_a they allow for calculation of the volume specific extinction coefficient according to:

$$\beta_{e\ l,j} = k_{e\ l,j} \cdot \rho_a \cdot \Psi_{3,l} \cdot 10^{-6}. \quad (4.11)$$

Using equation 4.9 and the single scattering albedo gives the scattering volume coefficient:

$$\beta_{s\ l,j} = \omega_{l,j} \cdot \beta_{e\ l,j}. \quad (4.12)$$

Furthermore, in order to obtain an averaged asymmetry parameter from the combination of ART aerosol and climatology later on an auxiliary variable $\chi_{l,j}$ is defined as:

$$\chi_{l,j} = \beta_{s\ l,j} \cdot g_{l,j}. \quad (4.13)$$

The reason for doing so becomes clear at the end of this section. Summation over all ART modes results in parameters solely dependent on the waveband as the three previous measures can be handled additively (equation 4.4):

$$\beta_{e\ j} = \sum_{l=1}^L \beta_{e\ l,j}; \quad \beta_{s\ j} = \sum_{l=1}^L \beta_{s\ l,j}; \quad \chi_j = \sum_{l=1}^L \chi_{l,j}. \quad (4.14)$$

The next step is a conversion from volume specific measures to values per model layer in order to be consistent with the Tegen climatology later on and enable introduction into the RRTM scheme. This is achieved by multiplication with the respective layer height Δz for every grid box, assuming

a homogeneous volume extinction coefficient throughout the layer:

$$\tau_{e j} = \beta_{e j} \cdot \Delta z, \tau_{s j} = \beta_{s j} \cdot \Delta z, \Xi_j = \chi_j \cdot \Delta z. \quad (4.15)$$

As the previous step involved a unit change from $/\text{m}^{-1}$ to $/\text{layer}^{-1}$ for all variables the resulting τ is a measure of the optical depth per layer. Summing up over all layers gives the total aerosol optical depth of the ART aerosol at a specific waveband which is used frequently in the analysis part of this work.

Subsequently the values obtained for the ART aerosol can be added to the climatological aerosol properties from the Tegen climatology. The climatology of the respective aerosols calculated on-line within ART is multiplied by zero. The values for the optical depth $\tau_{e j}^*$, the single scattering albedo ω_j^* and the asymmetry parameter g_j^* are the combined values from ART and climatology at every grid point per waveband which are then returned to the RRTM radiation routine:

$$\tau_{e j}^* = \tau_{e c j} + \tau_{e j}, \quad (4.16)$$

$$\tau_{s j}^* = \tau_{s c j} + \tau_{s j}, \quad (4.17)$$

$$\Xi_j^* = \Xi_{c j} + \Xi_j, \quad (4.18)$$

$$\omega_j^* = \frac{\tau_{s j}^*}{\tau_{e j}^*}, \quad (4.19)$$

$$\begin{aligned} g_j^* &= \frac{\Xi_j^*}{\tau_{s j}^*} = \frac{\Xi_{c j} + \Xi_j}{\tau_{s c j} + \tau_{s j}} = \frac{\Xi_{c j} + \chi_j \cdot \Delta z}{\tau_{s c j} + \beta_{s j} \cdot \Delta z} \\ &= \frac{\Xi_{c j} + \sum_{l=1}^L \beta_{s l, j} \cdot g_{l, j} \cdot \Delta z}{\tau_{s c j} + \beta_{s j} \cdot \Delta z}. \end{aligned} \quad (4.20)$$

The last line clarifies the reason for introducing the auxiliary parameter χ_j earlier on, it enables calculation of a weighted average value of the asymmetry parameter from ART aerosol and climatology using quantities suitable for summation.

4.3 Radiative properties of mineral dust

The following section deals with the determination of the optical properties for mineral dust which are needed as input arguments for the radiation routine. The optical properties which are calculated for every mode l and radiation waveband j with the help of Mie calculations are the mass-specific extinction coefficient $k_{e l, j}$, the single scattering albedo $\omega_{l, j}$ and the asymmetry parameter $g_{l, j}$.

When investigating the interaction of particles with radiation size matters. An overview of scattering regimes in dependence of particle size and wavelength is given in figure 4.2, which is adapted from Petty (2006). The relation between the size of scattering particles and the wavelength of the

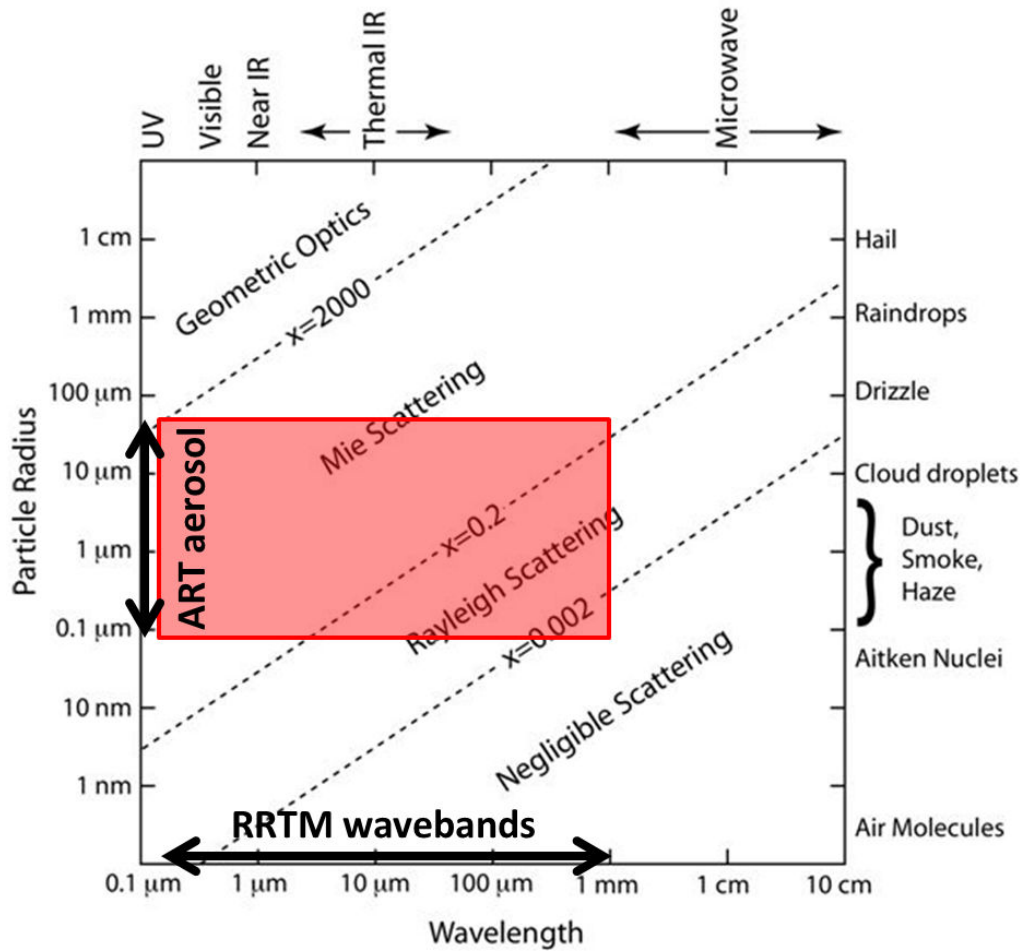


Figure 4.2: Scattering regimes, approximate size range of the mineral dust log-normal distributions simulated in ART and range of wavelengths for which radiative transfer is calculated by the RRTM. Red rectangle displays region for which the optical properties have to be calculated. Adapted from Petty (2006).

incident radiation is described using a non-dimensional size parameter defined as

$$x = \frac{2\pi r}{\lambda}, \quad (4.21)$$

where r denotes the particle radius and λ the wavelength of the incident radiation. There are two regimes in which scattering properties can easily be estimated. If particles are far smaller than the wavelength of incident radiation scattering is negligible, although absorption can still play an important role. If particles are far larger than the wavelength the laws of geometric optics become applicable. However, in between those two regimes a region exists where the particles are of the same order as the wavelength of incident radiation. For this region the phenomena of diffraction and constructive as well as destructive interference become important and more complex methods are needed to estimate the scattering and absorption optical properties of particles. Three parameters are important to determine the optical properties in this region:

1. The value of x , representing the exact ratio of particle size to incident wavelength of radiation.
2. The relative index of refraction defined as $m = \frac{B_2}{B_1}$, describing the ratio of the complex refractive indices of particle B_1 and surrounding medium B_2 , respectively. As mineral dust is suspended in air, whose refractive index is approximately equal to one, we are left with $m = B_2$.
3. The particle shape, which can be very complex. However, due to the simplicity of radiative transfer equations the complexity can not be accounted for in the model so far. Furthermore determination of optical properties for non-spherical particles is very complex and computationally expensive. Therefore particles are assumed to be spherical, the validity of this assumption in the case of mineral dust is discussed later on.

The theory providing the optical properties for spherical particles by solving the Maxwell equations is called Mie theory after Gustav Mie who provided the first complete description in 1908. It is explained in the following section. The solutions obtained using Mie theory are also valid in the Rayleigh-scattering regime which is only an approximation of the more exact Mie-solutions. The same is true for the geometric optics regime.

4.3.1 Mie calculations

Mie calculations can be used to determine the optical properties of mineral dust if the complex refractive index is known (Bohren and Huffman, 1983; Petty, 2006). Mie calculations provide a solution to the Maxwell equations using proper boundary conditions. The theory was introduced by Mie (1908) and since then numerous computer codes have been developed to calculate the Mie series solutions. A very brief outline is given in Petty (2006) which is recounted here. The Mie theory uses Maxwell's equations to solve a three dimensional electromagnetic wave equation expressed in spherical coordinates. Using appropriate boundary conditions at the surface of the sphere, a separable partial differential equation is obtained. The solution of this equation can be written as an infinite series of products of orthogonal functions. These series include sines and cosines for the azimuthal dependence on ϕ , spherical Bessel functions for the radial dependence on r as well as Legendre polynomials for the dependence on the polar angle Θ . As Petty (2006) states, the extinction and scattering efficiencies of a spherical particle can then be written as:

$$Q_e = \frac{2}{x^2} \sum_{n=0}^{\infty} (2n+1) \Re(a_n + b_n), \quad (4.22)$$

$$Q_s = \frac{2}{x^2} \sum_{n=0}^{\infty} (2n+1) (|a_n|^2 + |b_n|^2). \quad (4.23)$$

Mie codes calculate the coefficients a_n and b_n which are called Mie scattering coefficients, these are solely dependent on the particle diameter d_p , wavelength λ of the incident radiation, and the complex refractive index B . The refractive index B of the scattering material itself is dependent on

the wavelength again, therefore Mie calculations can only be performed for wavelengths at which B_λ is known. By truncation of the infinite series an approximate solution for Q_e and Q_s can be obtained as is explained by Bohren and Huffman (1983). Estimation of the number of terms required before truncation and calculation of the series is performed by the Mie code as well.

$Q_e(d_p, \lambda, B_\lambda)$ and $Q_a(d_p, \lambda, B_\lambda)$ are the results for the extinction and absorption efficiency obtained from Mie calculations. Likewise to the Mie scattering coefficients, they are solely dependent on the particle diameter (and thereby the parameters of the log-normal distribution of mode l), the wavelength of the incident radiation and the refractive index of mineral dust. To obtain the volume-specific extinction coefficient $\beta_e(l, \lambda, B_\lambda)$ of a log-normally distributed mode l from the extinction efficiency $Q_e(d_p, \lambda, B_\lambda)$, the following integration needs to be performed:

$$\beta_e(l, \lambda, B_\lambda) = \int_0^\infty \frac{\pi d_p^2}{4} Q_e(d_p, \lambda, B_\lambda) \psi_{0,l}(d_p) dd_p. \quad (4.24)$$

It is of crucial importance that the sampling points used for the diameter d_p in the integration are the same ones which are used for representation of the log-normal distribution in the Mie calculations. Because the total mass mixing-ratio $\Psi_{3,l}$ is the prognostic variable in ICON-ART we need the mass-specific extinction coefficient $k_e(l, \lambda, B_\lambda)$ which can be obtained through combining equations 4.1 and 4.3:

$$k_e = \frac{\beta_e}{M} = \frac{N\sigma_e}{M} = \frac{NA_{pc}Q_e}{M}.$$

However, mineral dust in ICON-ART is not mono-disperse but represented by three modes, described by log-normal distributions of particles (see section 3.1.2). According to Petty (2006), we can therefore obtain the mass-extinction coefficient for every mode and wavelength through:

$$\begin{aligned} k_e(l, \lambda, B_\lambda) &= \frac{\int_0^\infty \frac{\pi}{4} d_p^2 Q_e(d_p, \lambda, B_\lambda) \psi_{0,l}(d_p) dd_p}{\int_0^\infty \psi_{3,l}(d_p) dd_p} \\ &= \frac{\int_0^\infty \frac{\pi}{4} d_p^2 Q_e(d_p, \lambda, B_\lambda) \psi_{0,l}(d_p) dd_p}{\int_0^\infty \rho_p \left[\frac{\pi}{6} d_p^3 \right] \psi_{0,l}(d_p) dd_p}. \end{aligned}$$

Because the wavelengths λ for which the refractive index is known do not coincide with the RRTM wavebands the results have to be averaged to the respective wavebands. Averaging the $k_e(l, \lambda, B_\lambda)$ to one value per band gives the final values of the mass extinction coefficient $k_{e,l,j}$ used in ICON-ART.

Utilizing Mie calculations introduces assumptions about the mineral dust's properties. First, Mie calculations can only be conducted for spherical particles, this is generally not fulfilled for single mineral dust particles (Otto et al., 2009; Kahnert et al., 2007). However, for a population of

randomly oriented non-spherical particles this assumption introduces negligible errors if only albedo and flux related quantities are calculated (Mishchenko et al., 1995, 1997). Due to the random orientation of the particles a collection of particles scatters light similar to a spherical particle because the individual differences disappear in the angular integration (Tegen and Lacis, 1996). Therefore Mie calculations are able to provide a good representation of scattering even for non-spherical particles.

The second assumption arises from the need to know about the particles refractive index. Because Mie calculations are conducted off-line and just once for the global domain, an internal homogeneous mineralogical mixture of all particles is assumed. This is a more critical assumption, because generally it is not fulfilled. The refractive index of mineral dust depends on the mineralogical composition and thereby on the source region of the particles (Petzold et al., 2009). For this problem however, three practical issues prevent the more detailed description of the different properties within ICON-ART. The first problem is the lack of observational data of mineral dust refractive indices. The measurement of dust refractive indices itself presents a great challenge to researchers and variability between different studies is responsible for a large uncertainty in the radiative forcing, as discussed in Myhre and Stordal (2001). Furthermore, there is lack of observations of refractive indices from different source regions. In this work refractive indices from different experiments are discussed and used, most of them investigating Saharan dust. To complicate things further, even within the Sahara there exist large differences when investigating dust from different source regions (Petzold et al., 2009). The second problem is the currently lacking possibility to transport dust with different properties in ART. At the moment it is not planned to implement this feature in the near future. However, the ageing of dust through coagulation with different coating materials, e.g. black carbon or water, will be considered. The third problem is the absence of a global dataset of the earth's crust mineralogical composition in ICON-ART at the moment, making a more detailed availability of refractive indices futile. In conclusion, the optical properties of mineral dust transported in the model are similar to those of Saharan dust for all model domains.

Nevertheless, a principal investigation of mineral dust influence on meteorological systems in the Middle East is possible. The influence of differences in the refractive indices is mostly small compared to the influence of a varying size distribution, the latter effect being represented in ICON-ART. This is shown in the subsequent sections and was also the main result of a sensitivity study conducted by Myhre and Stordal (2001).

4.3.2 Refractive index

For computation of the optical properties using Mie calculations the spectrally resolved refractive index of mineral dust is needed. The refractive index B can be written as a complex number:

$$B_\lambda = \Re(B_\lambda) + \Im(B_\lambda) = n + ik. \quad (4.25)$$

The real part n describes the relation between the phase speed of an electromagnetic wave in vacuum c_0 and in a medium c ,

$$n = \Re(B) = \frac{c_0}{c}. \quad (4.26)$$

The imaginary part k is related to the ability of a substance to absorb radiation. For a homogeneous medium the relation with the absorption coefficient β_a in the Lambert-Beer law is straight forward and given through:

$$k = \Im(B) = \frac{\beta_a \cdot \lambda}{4\pi}. \quad (4.27)$$

However, a distribution of mineral dust particles suspended in air does not represent a homogeneous medium but lies in the Mie-scattering regime for most particle diameters and wavelengths. Therefore the relation is complex and can only be calculated using Mie calculations.

The refractive index of mineral dust has been determined in numerous laboratory as well as field experiments which are discussed in the following. An overview of different studies is given in table 4.1.

Table 4.1: Overview of studies determining mineral dust refractive indices.

Publication	Characterisation	Source	Collection	Waveband	Acronym
Petzold et al. (2009)	SAMUM	Sahara	Aircraft	SW	SAM
Helmert et al. (2007)	Compilation	Various	-	SW, LW	HEL
Fouquart et al. (1987)	ECLATS	Sahara	Niamey, Niger	LW	FOU
Köpke et al. (1997)	GOADS Comp.	Various	-	SW, LW	KOE
Volz (1973)		Sahara	Barbados	LW	SVO
Volz (1972)	Rain-out Dust	Various	USA	SW, LW	DVO
Dubovik et al. (2002)	AERONET	Various	Worldwide	SW	DUB

Results from the different studies are portrayed in figure 4.3 for the real part of the refractive index and in figure 4.4 for the imaginary part. Values for the real part of the refractive index in the shortwave are regularly determined to be between 1.48 and 1.56 independent of wavelength. The imaginary part exhibits a much larger variation with wavelength on the order of two magnitudes (fig. 4.4). Additionally, differences between and within studies amount to approximately one order of magnitude. Two main reasons can be identified for this behaviour, first the experimental difficulties in determining the imaginary part of the refractive index itself and second differences in mineralogical composition of the materials leading to different absorption characteristics. For the longwave part of the spectrum fluctuations in the real part of the refractive index are also apparent. Values range from 0.5 to 3 depending on wavelength. The imaginary part shows larger values up to 2 in this part of the spectrum, also with sharp variations due to specific minerals.

Highwood and Ryder (2014) give a summary of how the different characteristics in the refractive indices influence the optical properties. For example, peaks in the real part clearly show as maxima of the extinction coefficient. The single scattering albedo (SSA) on the other hand is determined by the imaginary part of the refractive index. Lower values of the imaginary part cause higher values of the SSA, thereby signalling reduced absorption.

As discussed in Sokolik and Toon (1999), different minerals lead to different peaks in the refrac-

tive index depending on the mineralogical composition of the dust. Iron oxides such as haematite show the strongest absorption at UV and visible wavelengths and therefore their varying contribution is the most important. Typical values range below 10% weight percentage, with the variability explaining most of the refractive's index imaginary part fluctuations as was shown in Alfaro et al. (2004) and Linke et al. (2006). According to Sokolik and Toon (1999), Quartz, often being dominant in terms of mass, shows high values of absorption in the IR atmospheric window without being a good absorber at UV and visible wavelengths. Clays also exhibit strong absorption at IR wavelengths with the different types of clay having noticeably different features in their absorption spectra. In addition, clays are good absorbers at visible wavelengths with the values of their imaginary part refractive index increasing towards UV wavelengths.

One of the most widely used measurements of the refractive index for the full spectrum was done by Volz (1972), the values are also reproduced in a study by Shettle and Fenn (1979). Mineral dust was collected and analysed after being washed out through precipitation processes. Compared to measurements from more recent studies Volz (1972) tends to overestimate the absorptive characteristics of the mineral in the near infra-red region as can be seen in figure 4.3. In the long-wave part of the spectrum the curve appears smoother than other studies and represents a lower bound for the imaginary part of the refractive index. In another study Volz (1973) determined the refractive index of Saharan dust samples collected in Barbados for the longwave part of the spectrum. The samples generally show a higher absorption than the rain-out dust. Furthermore the variations with wavelength are larger, probably due to a less homogeneous mixture and mainly clay with traces of quartz being present, explaining the higher values towards the near-IR region. Also shown in figure 4.3 and 4.4 are values of the refractive index from two studies which are widely cited in literature. Fouquart et al. (1987) measured the optical properties from an aircraft during the ECLATS experiment. For the real part these values constitute a lower boundary, whereas for the imaginary part they are represented well by other studies. The values from Fouquart et al. (1987) were used by Rémy et al. (2015) for modelling aerosol optical properties during a dust storm in the eastern Mediterranean.

The values for the Global Aerosol Dataset (GADS) study (Köpke et al., 1997) presents a compilation of various other measurements. In the longwave part of the spectrum it is mostly made up of the values measured by Volz (1973). However, in the shortwave some differences exist, most noticeably the increasing values of absorption towards the UV. In the near IR the values are not representative when compared to more recent studies of the refractive index.

Helmert et al. (2007) created an extensive literature review based compilation and extended it with new inputs, it is an important study for this work as their refractive index values are used for the longwave part of the spectrum. The authors combined the spectral refractive indices from multiple studies, both field measurements (Dubovik et al., 2002; Sinyuk et al., 2003) as well as laboratory studies (Volz, 1973). In addition, Helmert et al. (2007) added new data through calculating the refractive index for an internal mixture of 98% kaolinite and 2% haematite using a method by Sokolik and Toon (1999). The real part of the refractive index by Helmert et al. (2007) is confined by the measurements of Volz (1973) as an upper bound and by Fouquart et al. (1987) as a lower bound. The imaginary part shows higher values of absorption than other studies between 4 μm and

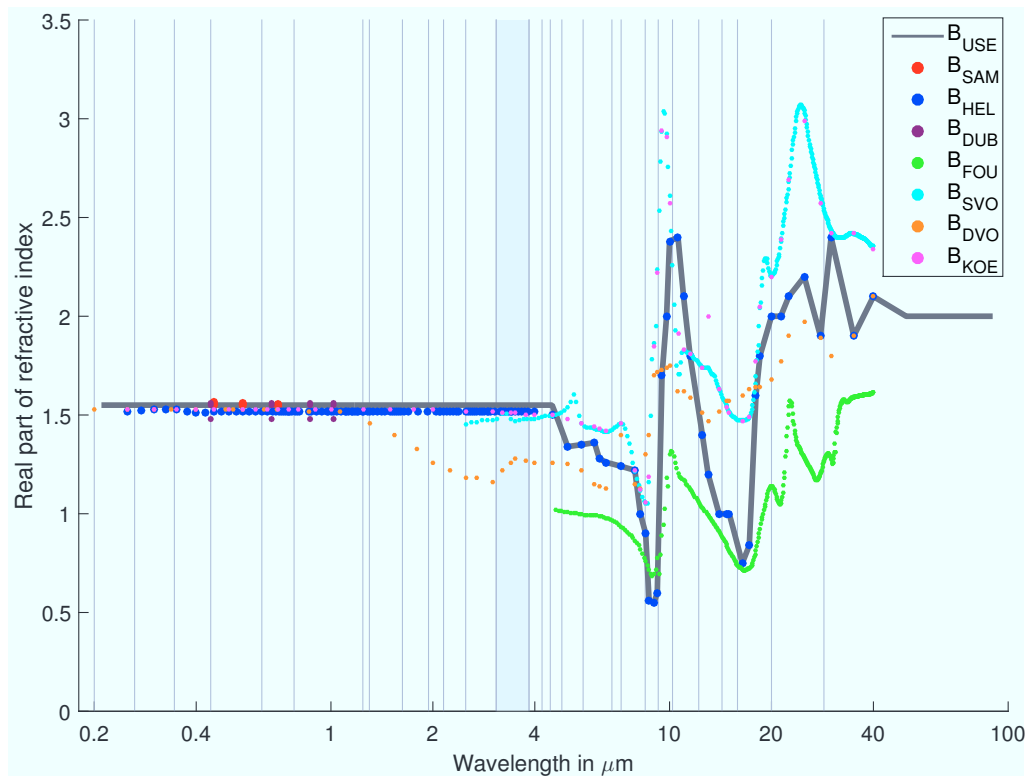


Figure 4.3: Real part of refractive indices according to studies listed in table 4.1. Note the logarithmic x-axis. The borders of the RRTM radiation scheme wavebands are adumbrated as grey lines in the background. The filled grey band represents the waveband present both in the longwave and shortwave part of the RRTM.

10 μm . Peaks of absorption coincide well with maxima determined by Volz (1973) and Fouquart et al. (1987), however with a larger amplitude. As Helmert et al. (2007) explain, this could be due to the fact that the Caribbean dust samples contained no haematite. In the shortwave region the values show a strong increase towards the UV, which is also seen by other studies. Probably due to the presence of a higher haematite fraction the values determined by Helmert et al. (2007) are higher than those of e.g. Petzold et al. (2009) and Dubovik et al. (2002).

Another important study for this work was done by Petzold et al. (2009). They determined the refractive index of mineral dust from aircraft measurements during the Saharan Mineral Dust Experiment (SAMUM) for three wavelengths (467 nm, 530 nm and 660 nm) in the shortwave. The evaluated flights were conducted over different regions of the Sahara in summer 2006. Back trajectories were calculated to identify the source region of the dust. They found the imaginary part of the refractive index to be highly variable depending on the source region, which was confirmed by a chemical analysis conducted on samples taken during the flight. The greatest variation on the order of one magnitude was apparent in the red spectral region at 660 nm. However, Petzold et al. (2009) could not attribute this change to a variation in haematite content which is only weakly absorbing at this wavelength and thereby cannot explain the large variation. Hence they conclude that another spectrally flat absorber such as black carbon or kaolinite must be present. Petzold

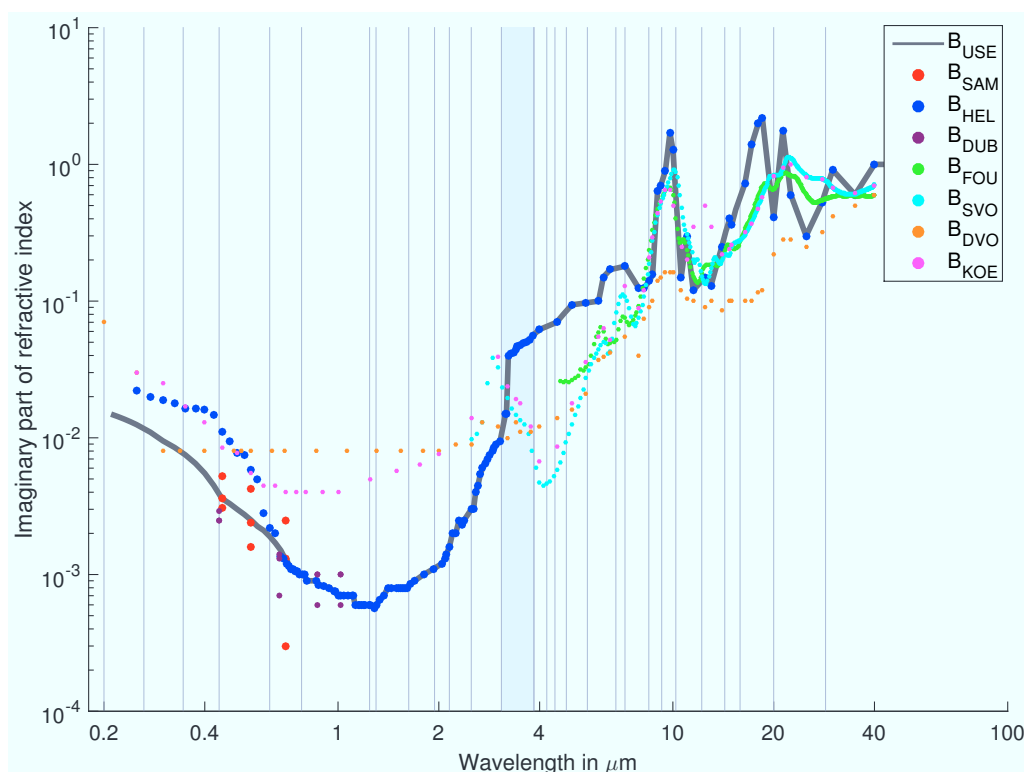


Figure 4.4: Same as figure 4.3, but for the imaginary part of refractive indices.

et al. (2009) also state that laboratory studies tend to overestimate the absorption properties of mineral dust due to the sole attribution of absorption to haematite. Furthermore, sun photometry derived values can be seen as a lower bound for the imaginary part of the refractive index according to them.

The values used in ICON-ART are shown as grey lines in figure 4.3 for the real part and in figure 4.4 for the imaginary part of the mineral dust refractive index. These are the same values as used by Stanelle et al. (2010) for COSMO-ART. The longwave part of the radiative transfer model down to 4 μm utilizes values as published by Helmert et al. (2007). For wavelengths smaller than 4 μm the shape of the Helmert et al. (2007) curve is still replicated, however with a fit through smaller values for the refractive index imaginary part in the visible part of the spectrum. This part of the spectrum is especially important as solar radiation intensity is highest for these wavelengths. The values taken as a reference were measured during SAMUM (Petzold et al., 2009). The reason for deviating from Helmert et al. (2007) in the shortwave part is the more recent date of the Petzold et al. (2009) study. Furthermore, there is a better agreement with Dubovik et al. (2002), who by inversion of AERONET retrievals determined values similar to Petzold et al. (2009). Recent studies found a better agreement of observed radiative forcing by mineral dust with data obtained from AERONET (Balkanski et al., 2007). Finally, McConnell et al. (2010) also measured imaginary part refractive index values similar to those used in ICON-ART.

4.3.3 Results of Mie calculations

For the Mie calculations a code developed by Bond et al. (2006) was used, this in turn utilizes a subset developed by Mätzler (2002) for calculation of the Mie scattering coefficients and truncation of the series. The code was adapted to allow for processing of multiple wavelengths and averaging to the RRTM wavebands in a post-processing step. Furthermore a new polynomial parametrization per waveband with the median diameter as independent variable was introduced to account for the change in median diameter during the transport processes.

Results of Mie calculations for three ART mineral dust modes are shown in 4.5 and can be compared to studies by different authors such as Rémy et al. (2015), Helmert et al. (2007) and Tegen and Lacis (1996). Although these authors use slightly different size distributions and refractive index properties they obtain results very similar to the ones presented here.

Dependence on wavelength

The absolute values of the extinction coefficient (EXT) are of secondary importance, as the total extinction optical depth is obtained by multiplication with the local mass mixing ratio of the mineral dust aerosol. The mass mixing ratio of the different modes usually changes with distance from the source region as larger particles settle out. Close to the source region the largest mode dominates the mass mixing ratio, whereas in more distant regions the smallest mode can play an important role (see section 5.3.4). To discuss the wavelength dependent optical properties of the modes in general, the EXT are shown as points normalized with respect to the value at 550 nm in figure 4.5. As can be seen from the normalized values, the EXT is highest in the regions where the median particle diameter is in the same range as the wavelength. One should bear in mind however, that the absolute values of the EXT are $1.22 \text{ m}^2 \text{ g}^{-1}$ for the smallest mode at 550 nm, $0.21 \text{ m}^2 \text{ g}^{-1}$ for the second largest mode and $0.09 \text{ m}^2 \text{ g}^{-1}$ for the largest mode. Therefore, particles from the smallest mode have a 10 times higher extinction efficiency than particles from the largest mode in the shortwave. The absolute values of the EXT, averaged to the RRTM wavebands as used in ICON-ART, are shown as horizontal lines in figure 4.5. The difference in absolute values of the EXT decreases towards the longwave and eventually the EXT for all modes is in the vicinity of $0.1 \text{ m}^2 \text{ g}^{-1}$.

The shape of the SSA curve is mostly determined by the values of the imaginary part of the RI as it represents the likelihood of absorption during a scattering process. Consequently, due to the increase of the imaginary part of the RI towards the visible part of the spectrum, the SSA shows decreasing values in this region representing a greater probability for absorption. In the near infra-red region the SSA reaches values of almost one, showing that mineral dust absorbs very little in this part of the spectrum. However, towards the far infra-red region the values of the SSA decrease again substantially, coinciding with higher values of the imaginary part of the RI. This justifies the RRTM's neglect of scattering on the longwave region of the spectrum, the drop in SSA can be seen to coincide well with the RRTM regime borders. In close analogy to the EXT, each mode has the highest values of SSA in the region of its median diameter. In the shortwave, the largest mode absorbs radiation most efficiently, whereas in the longwave the smallest mode

is the best absorber. Again, one needs to bear in mind the absolute concentrations are of great importance for the overall absorptive effect of each dust mode.

The asymmetry parameter (ASY), representing the ratio of forward versus backward scattering, shows an almost monotonous decrease towards longer wavelengths. The smallest mode shows significantly lower values than the two larger modes which implies stronger backward scattering by this mode.

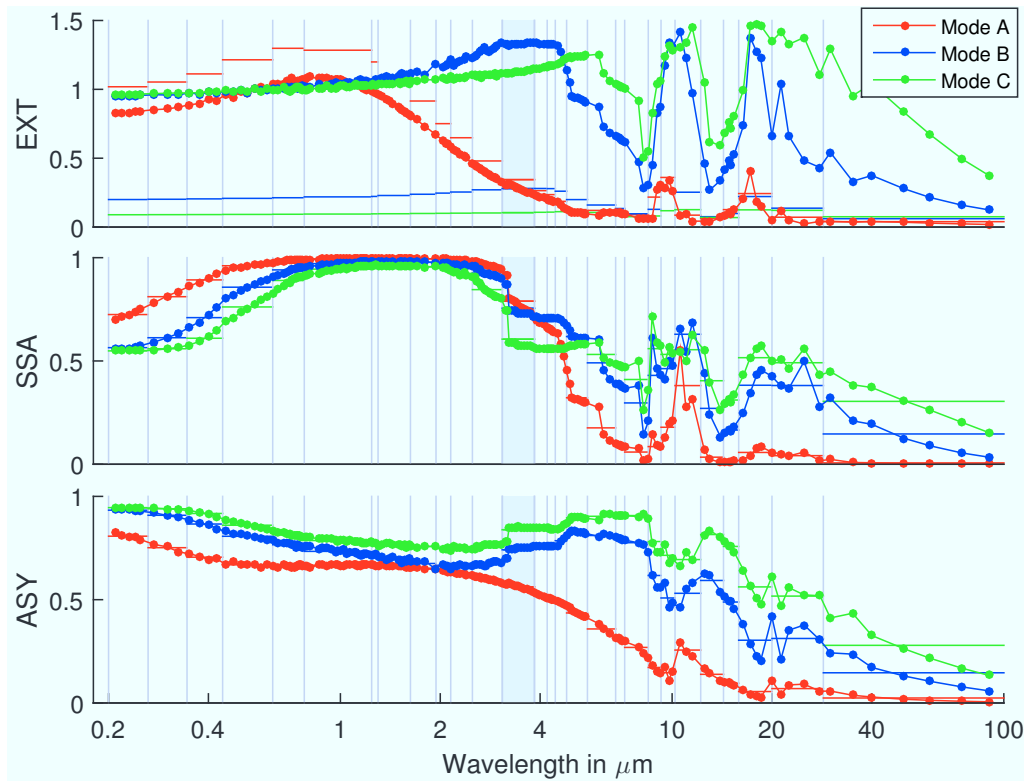


Figure 4.5: Extinction coefficient (EXT), points are normalized with respect to value at 550nm, horizontal lines show absolute values as used in ICON-ART in $\text{m}^2 \text{g}^{-1}$, single scattering albedo (SSA) and asymmetry parameter (ASY) for all modes utilizing B_{USE} .

Dependence on refractive index

Using refractive indices from other studies has an effect on the calculated mineral dust optical properties. In figure 4.6 results of the Mie calculations are shown using refractive indices from different studies for the smallest mode A, for which a change in the refractive index exhibits the largest influence. The refractive indices used for comparison are the ones with largest differences compared to B_{USE} , namely that of Volz (1972) and Köpke et al. (1997). Changes in the optical properties are biggest in the visible and near infra-red spectral region up to 10 μm , this is where the largest differences in the imaginary part of the refractive index exist between studies. Consequently, the shape of the SSA curves determining absorption properties varies strongest in this region. As the SSA values obtained using B_{USE} are highest in all spectral regions where scatter-

ing is taken into account it can be said that the absorption of radiation due to mineral dust is more likely to be under- than overestimated in ICON-ART, as the mineral dust has weakly absorbing characteristics. This is coherent with the imaginary part of the refractive index in the shortwave being based on SAMUM results, an experiment which found less absorptive properties of mineral dust in the visible spectral region (Petzold et al., 2009). For the scattering direction characteristics (ASY) a variation in refractive indices has small effects and ICON-ART mineral dust scattering direction properties are well reproduced. An interesting feature is the variation of the EXT and ASY calculated from Volz (1972) in the near infra-red region, this is due to the lower values of the real part of the refractive index in this region according to Volz (1972). Due to the older date of the study and the special dust characteristics (rain-out dust) these differences are not investigated further but deemed measurement artefacts. The same behaviour as explained here is observable for the two larger modes as well, variations can be seen mostly for the SSA in the visible to near infra-red spectral region (not shown).

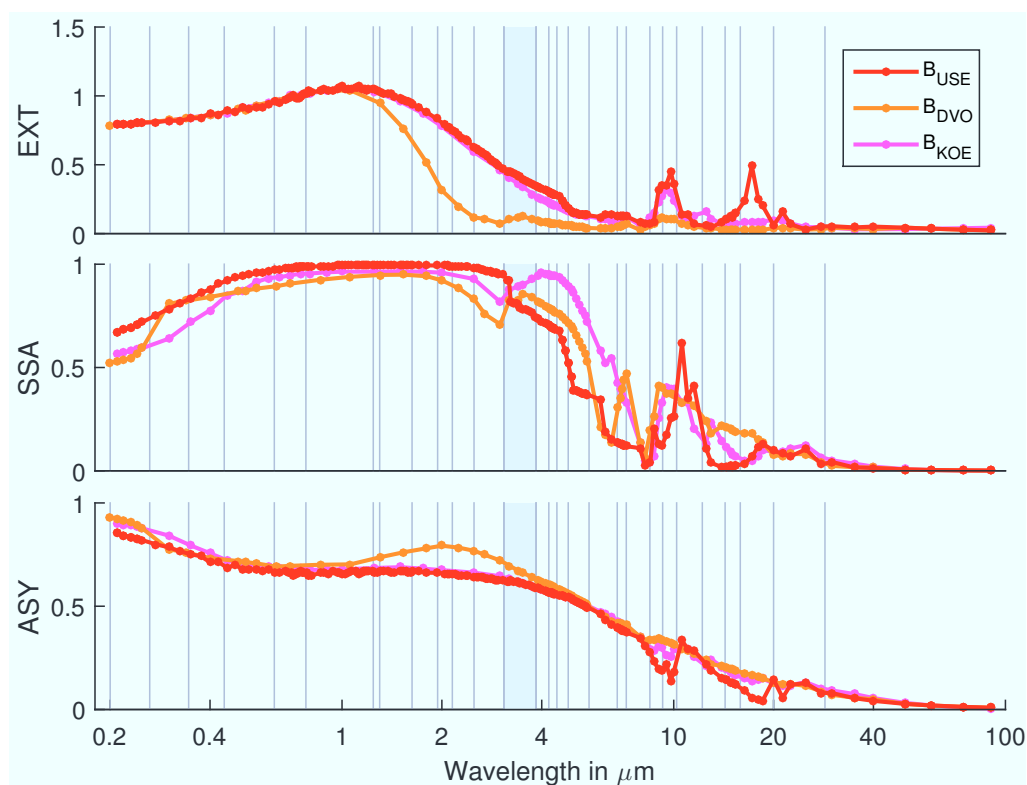


Figure 4.6: Influence of differences in refractive indices on optical properties for mode A.

Dependence on size distribution

The optical properties of mineral dust are highly dependent on its particle size distribution represented through three log-normal modes in ART. From the six prognostic variables in ART, the specific aerosol mass and number concentration for each of the three modes, a median diameter can be diagnosed for each mode. Due to different processes such as sedimentation and dry depo-

sition acting independently on the specific aerosol mass and number concentrations in ART, the diagnostic median diameter of each mode changes during transport (the standard deviation of each mode is kept constant). In a physical sense, the most important effect is large particles settling out faster due to sedimentation, which results in mostly smaller particles being transported to distant regions within each mode. Therefore, the median diameter of each mode is expected to decrease during transport which is investigated in section 5.3.4. To include the effects of a 'intra-modal' changing median diameter for each mode during transport a new parametrization was developed as a part of this work. The effect of a changing median diameter should not be confused with, e.g. the largest mode being subject to stronger gravitational settling than the smallest mode as this 'inter-modal' effect is already included in the simpler parametrization of mineral dust optical properties shown before.

To investigate the effect of a changing median diameter during transport, Mie calculations were conducted repeatedly with different median diameters for each mode. The results are shown, again for the smallest mode where changes are most visible, in figure 4.7. The median diameter changes from 0.25 – 1.25 times the initial median diameter of mode A, in numeric values this corresponds with a median diameter of the count number distribution from 161 nm to 805 nm.

It is apparent that changes in the optical properties due to varying median diameters have the same magnitude as changes due to the refractive index used. In the shortwave spectral region the EXT increases strongly with a decreasing median diameter, whereas in the near infra-red region the EXT decreases. The course of the SSA shows that distributions of smaller particles absorb more strongly in the visible spectrum, whereas in the near infra-red to far infra-red they scatter a greater proportion of incident radiation. From the change in the ASY with varying median diameter it can be deduced that distributions of smaller particles scatter less into the forward direction than distribution of larger particles for all wavelengths. This is already apparent when comparing the scattering properties for the three initial modes. Mode B and mode C show a similar behaviour as discussed here although with lesser magnitude. One should bear in mind, however, that the absolute variations in optical properties with median diameter per mode are of secondary importance. This is due to the fact that for a change in radiative characteristics, both a change in median diameter and a high mass concentration are necessary to obtain a noticeable effect for the overall mineral dust optical properties. Therefore, even though changes in optical properties are largest for the smallest mode, incorporating the effect of a varying median diameter in ART is most important for the largest mode as is shown in section 5.3.4.

Parametrization of results

The previous section highlighted the importance of the mineral dust's population median diameter in determining its optical properties. For this reason the effect of a varying diameter has been implemented in ICON-ART, implying that the optical properties are calculated at every grid point and time step using the current diagnosed median diameter for each mode (equation 3.14).

In order to achieve this a parametrization for all optical properties f as function of the median diameter $\overline{d_{0,l}}$ was developed. In a Mie calculation post-processing step a third order polynomial

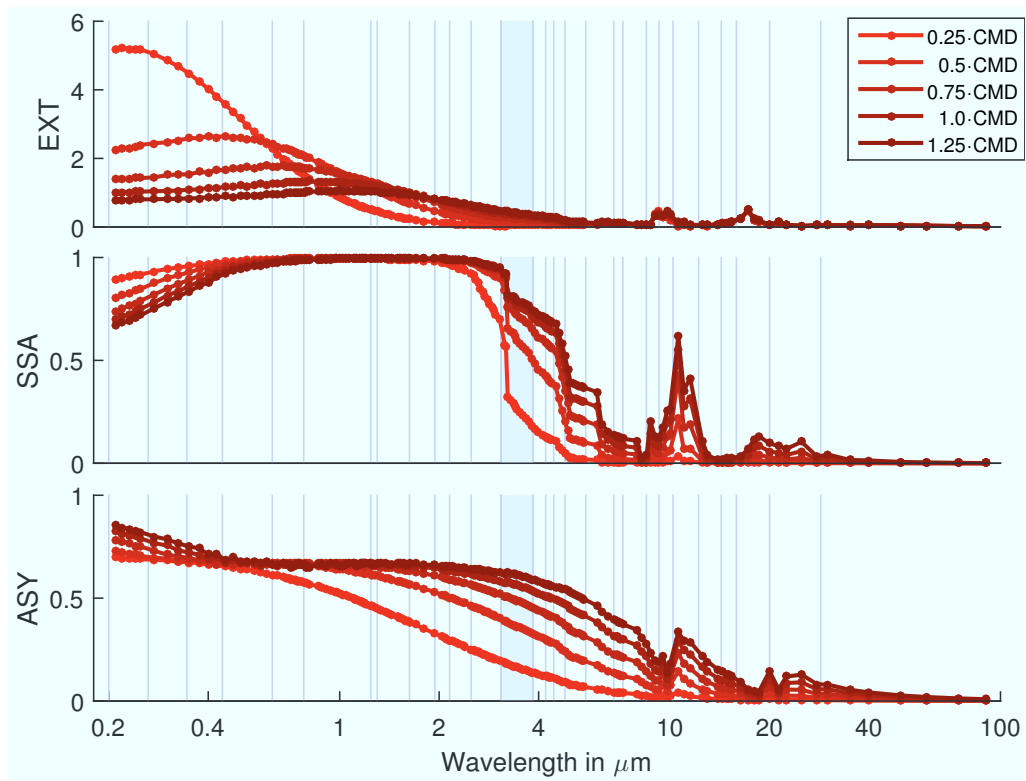


Figure 4.7: Influence of varying median diameter on optical properties for mode A.

of the form

$$f(\overline{d_{0,l}}) = p_1 \overline{d_{0,l}}^3 + p_2 \overline{d_{0,l}}^2 + p_3 \overline{d_{0,l}} + p_4 \quad (4.28)$$

is fitted to the results of multiple Mie calculations for median diameters between 0.25 – 1.25 times the initial median diameter of the count number distribution. This is done for every mode and every RRTM waveband respectively. The polynomial fit parameters are initialized in ICON-ART and used for determination of optical properties at every grid point with the diagnosed median diameter being the independent variable using the above formula. An example of this parametrization process is shown in figure 4.8 for the EXT of mode A for all 30 RRTM wavebands. The initial median diameter of the count number distribution is shown as a vertical black line at 644 nm. Results for the EXT are shown as a function of the count number median diameter and calculated for five diameters and 30 wavebands. An assignment of the polynomial fits to the specific wavebands is not shown as this figure serves only illustrative purposes. Different trends of the EXT for different wavebands are apparent. Whereas the EXT increases for some wavebands it decreases for others if the median diameter reduces. This behaviour is in agreement with figure 4.7, the maximum values allowing for attribution of some of the polynomial fits to specific wavebands. If the diagnosed median diameter in ICON-ART exceeds the boundaries of the parametrization scheme it is set to the last value calculated within the bounds of the parametrization. The procedure explained here is conducted for all properties and all modes separately as a continuous

parametrization over the full median diameter range is not possible due to the different standard deviation of each mode.

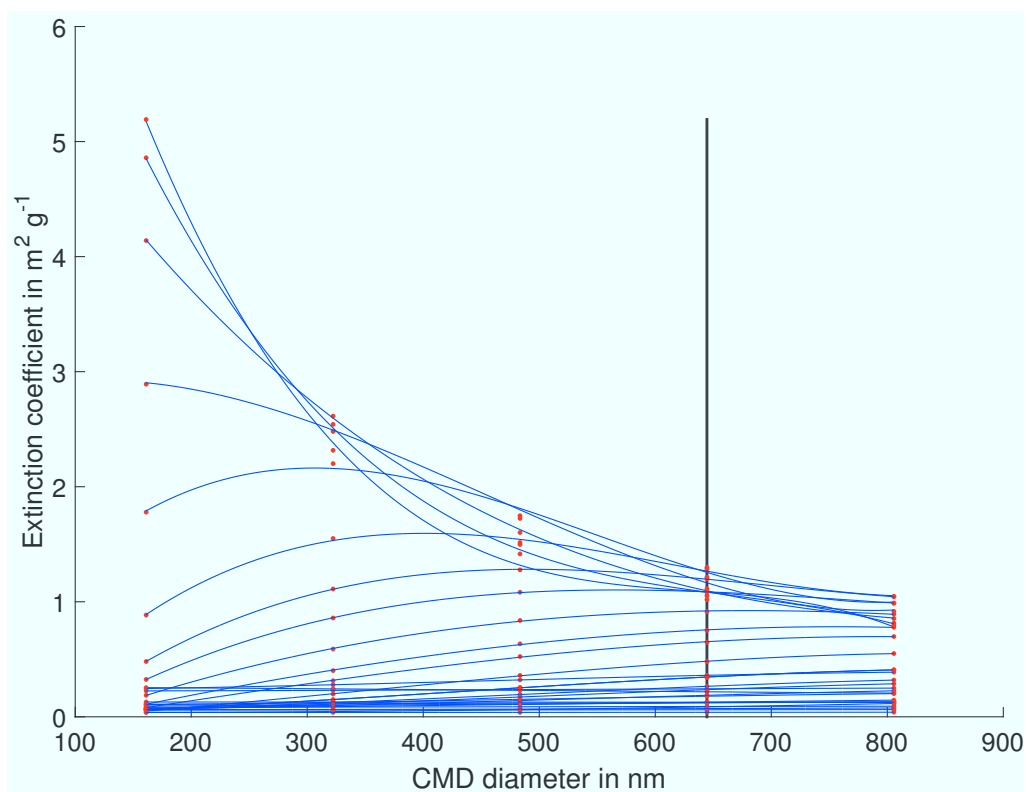


Figure 4.8: Parametrization of extinction coefficient as a function of the count number distribution median diameter (CMD) for 30 RRTM wavebands for mode A. The black line represents the initial CMD of mode A. Red points denote results of Mie calculations for five count median diameters and 30 wavebands. The blue lines represent the third order polynomial fit for every waveband.

5. Simulation of a severe dust event in the Eastern Mediterranean

In this chapter an in-depth analysis of a severe dust event which occurred in the Eastern Mediterranean in early September 2015 is provided (for an overview of the event, global circulation model forecast quality and its impact see chapter 1). The event investigated in this study is triggered by a synoptic situation termed active Red Sea Trough (RST) which is discussed in section 5.1.

The dust event consists of multiple stages and is created by the interaction of different meteorological systems, as is detailed in section 5.2. The section also provides a comparison of model results to available satellite observations, highlighting the ICON-ART simulation quality. The dominant atmospheric drivers are meso-scale convective systems (MCS) and their related cold-pool outflows (CPO). Furthermore, a heat low and the interaction of its associated cyclonic flow with the land inward penetrating land-sea breeze are important. At a later stage, a super-critical boundary layer flow and the connected hydraulic jump are responsible for the high dust concentrations in the southern EM.

The event and the related atmospheric drivers are influenced by the mineral dust radiation interaction, as is investigated in section 5.3. The mineral dust radiative effect is shown to have a systematic influence on the CPO structure and propagation speed. In addition, the effect of the improved parametrization for the mineral dust optical properties is also detailed in this section.

A special focus is put on long-range dust transport processes towards the southern EM in section 5.4 due to the occurrence of a hydraulic jump upstream the Dead Sea Rift Valley. Its importance for dust transport towards the southern EM is highlighted by a comparison of ICON-ART results to station measurements in Israel.

5.1 Synoptic situation

During early September, the region is usually still under the influence of a the Mediterranean ridge and connected subsidence over the EM. Furthermore, under usual early September conditions a stable and long-wave trough extends across Mesopotamia southwards to the Persian Gulf at 500 hPa (Bitan and Sa'Arani, 1992). Near the surface and up to 800 hPa the upper atmospheric trough is countered by a so called Persian trough which extends towards north-west from the Persian Gulf under easterly flow conditions. The normal surface circulation pattern over Mesopotamia and the EM in summer is therefore dominated by a Heat Low in the Persian Gulf

region extending towards north-west with an associated cyclonic flow around it. The result is in easterly flows across the Zagros Mountain range and Syria which converts into a northerly Etesian flow in the EM. This flow pattern in combination with the upper level subsidence due to the EM ridge reliably prevents development of any deep convection over the region in summer.

For the event simulated, the flow patterns are distinctively different from the usual summer conditions as the aforementioned Persian trough does not exist. Instead a low-level synoptic pattern termed Red Sea Trough (RST) with an eastern axis is apparent below 800 hPa which extends northward from the Red Sea towards central Syria under easterly flow conditions. The RST thereby advects hot and moist air from the Persian Gulf into the Mesopotamia region. The RST is accompanied by a mid-tropospheric trough between 700 – 400 hPa extending far southward into the EM under westerly flow conditions. This mid-level trough also advects warm and moist air into the Mesopotamia region alongside its front (downstream) region. At upper tropospheric levels above 400 hPa a short-wave trough exists in the region above Syria. This trough advects positive vorticity and cold air into the region at high altitudes, thereby creating quasi-geostrophic forced ascent and potential instability which enable the development of meso-scale organized convection. The combination of a low-level RST extending northward and upper tropospheric troughs extending southward into the EM has been termed active RST by previous researchers due to its high potential for severe weather (Krichak et al., 2012). The timing of the active RST synoptic situation is exceptional, as the RST usually starts to occur only by late September or early October (Alpert et al., 2004; Tsvieli and Zangvil, 2005), although events have been documented in August and September (Osetinsky, 2006). The active RST has been linked to severe weather phenomena in the EM and the Arabian peninsula in connection with atmospheric rivers transporting large quantities of precipitable water from eastern Africa, although the specific moisture sources are still debated (Vries et al., 2013, and references therein). The clustering of convectively active days with meso-scale convective organization is often observed during active RST situations (Krichak et al., 2012; Vries et al., 2013). In analogy with the findings of Miller et al. (2008), the meso-scale organized convective systems investigated here are clustered into a period of convectively active days due to the favourable conditions created by the RST. Vries et al. (2013) propose six criteria for the identification of active RSTs situations, these are:

1. The northward extension of the semi-permanent quasi-stationary RST.
2. An intensifying semi-permanent quasi-stationary Arabian anticyclone.
3. The intrusion of a mid-latitude upper level trough.
4. The intensification of the sub-tropical jet.
5. Enhanced moisture transport from the adjacent seas.
6. Upward motions resulting from the synoptic-scale dynamical forcing and tropospheric instability.

The existence and intensity of the phenomena suggested for the detection of active RST situations is investigated in the following.

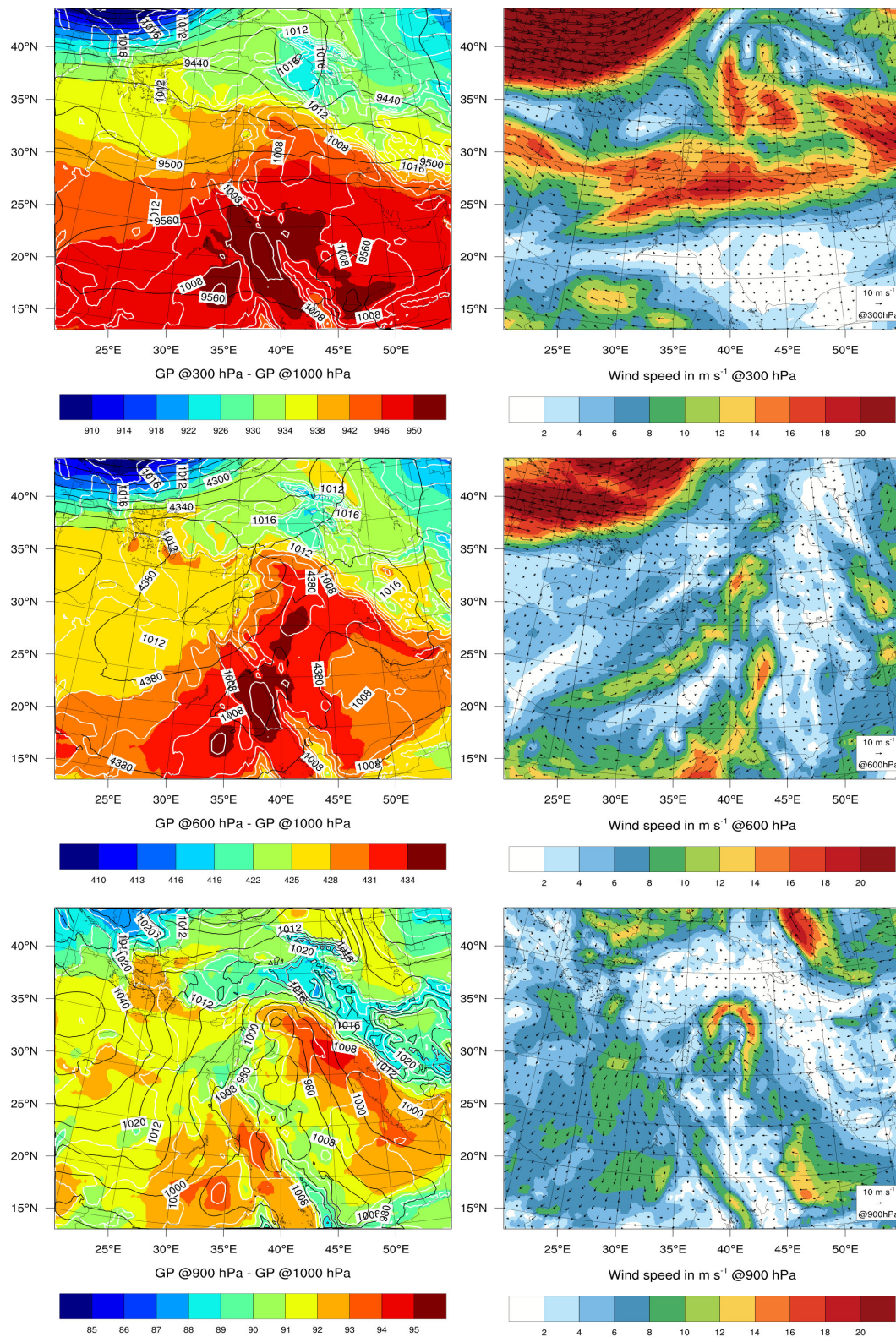


Figure 5.1: Synoptic situation on 06 September at 18 UTC as simulated by ICON-ART for the global domain. Shown are from top to bottom the 300 hPa, 600 hPa and 900 hPa level. Colour coded on the left side is the relative topography as the geopotential height of the respective layer minus the geopotential height of the 1000 hPa layer. Black lines denote the height of the respective pressure level in geopotential metres at 5 gpm intervals. White lines show surface pressure in hPa. On the right side wind speed is colour coded and wind velocity is shown as vectors.

The synoptic situation is analysed for 06 September 2015, 18 UTC in detail at 300 hPa, 600 hPa and 900 hPa levels, as at this point in time and the respective altitudes all relevant features are present in the atmospheric flow conditions. In figure 5.1, the RST with an eastern axis relative to the EM shoreline is visible at 900 hPa. The trough extends northwards along the Red Sea and up towards Turkey in easterly flow conditions. The direction of the trough axis and its position over the Red Sea make it plausible to attribute this trough to the RST category rather than to the Persian trough category, although in transition seasons mixture forms of both exist as they compete for dominance over the Arabian peninsula. The eastern flank (upstream) of the RST extends up to the Persian Gulf which is unusually far to the east. This is due to the early occurrence of the RST in September, when the Arabian peninsula is still intensely heated, with the thermal forcing favouring the spread of the RST over the land surface towards the east. The Arabian peninsula anticyclone at low to mid-levels is only weakly pronounced and located towards the east over the Persian Gulf. The reason is probably the early occurrence of the event shortly after summer with the Indian monsoon flow south of the Arabian peninsula still having great intensity. Extending far to the east, the RST, in connection with the Arabian peninsula anti-cyclone, advects moist and hot air towards Mesopotamia in a lower tropospheric southerly flow from the Arabian Sea and Gulf region. The described surface flow characteristics and surface level pressure distribution further support the categorization of the event as belonging to the RST category. For Persian trough regimes, the flow structure is characterized by a cyclonic flow around the Persian Gulf due to the low pressure centre in this region, resulting in a flow from northerly directions over Iraq and northern Saudi-Arabia. In opposition to this, a strong southerly flow exists in the region in the case presented here, which is crucial for the sustained lifetime of the meso-scale organized convection. The continuous advection of moist and hot air and its uplift in connection with the out-flowing cold-pool airmass enables sustained organized convection over the Syria-Iraq-Iran border region for a duration of more than 12 hours. The northern tip and axis of the RST is located above Syria and therefore matches with the development region of an intense heat low. During the later stages on 07 and 08 September a convective CPO and dust contained within it are transported towards south-west on the downstream side of the lower tropospheric RST.

In the mid troposphere from 700 – 400 hPa, overlaying the RST, a marked trough exists with an axis approximately along the Dead Sea Rift Valley, curving eastwards towards Egypt in the southern part. East of this trough structure (downstream) high wind speeds up to 20 m s^{-1} exist in a streak running from south-west towards north-east. This region also features high values of virtual temperature denoting hot air masses with high capacity for moisture transport. The streak is situated exactly upstream of the meso-scale convective system (MCS) development region. As suggested in previous studies (Krichak et al., 2012; Vries et al., 2013), this marked jet could provide significant moisture transport for the MCS from the Red Sea and Africa in the form of an atmospheric river with high values of atmospheric humidity. Atmospheric rivers are narrow streaks of high wind speeds which can exist over a duration of many days exporting large amounts of water vapour from the tropics (Zhu and Newell, 1998). Unfortunately, investigation of the dominant moisture transport paths is beyond the scope of this work. It is interesting to note that no convection develops above the Saudi-Arabian coastal mountains in the region of this streak.

Likely, this is due to the lack of upper atmospheric drivers in form of a short-wave trough and lack of inflow of cool air creating instability as well as the lack of near surface inflow of moist air, criteria which are only met at the foothills of the Zagros mountains. In the northern part of the large-scale trough a smaller, short-wave trough develops during 06 September over Syria.

In addition, at 300 hPa a marked subtropical jet above northern Saudi-Arabia is apparent. Above 400 hPa a smaller scale upper tropospheric trough advects cold air from the north into the MCS development region, thereby reducing atmospheric stability and creating potential for deep convection. In addition, the strong wind-shear between lower and upper levels in the Mesopotamia region produces the conditions necessary for MCSs by enabling a separation of up- and down-draft. Furthermore the divergence downstream the trough creates the dynamical preconditions for quasi-geostrophic forced uplift in the mid-troposphere. Therefore, this trough is responsible for the explosive development and organisation of the MCS, together with the forced orographic lifting above the Zagros mountain range. At a later stage on 08 September features of a weak cyclogenesis in the MCS are detectable in visible satellite images above the Caspian Sea through a cyclonic rotation of the remnant clouds from the MCS (not shown).

Summarizing, the synoptic situation discussed here shows distinct features of an active Red Sea Trough situation which enables a period of convectively active days with organized meso-scale convective systems.

5.2 Analysis of the driving atmospheric systems

In the following, a detailed analysis of the development stages and responsible atmospheric drivers which lead to the severe dust event is provided. The simulated convection and its interaction with dust emission is investigated in depth. Model results are compared to satellite observations at four characteristic points in time during the event development. An schematic depiction of the spatial extent of event stages and labels used is provided in figure 5.2, an overview of the temporal succession is given in figure 3.4. Unfortunately, the region where the MCS and the first stages of the CPOs occur are located in the Syria-Iraq border region, which is not covered by a meteorological observation network and at the time was controlled by the so-called 'Islamic state'. Therefore, no surface observations are available and the event can only be analysed using satellite data, which nevertheless yields interesting results. Due to the importance of the MODIS data and its rare availability, the times at which an in-depth analysis is conducted are chosen in accordance with MODIS overpasses.

5.2.1 First cold-pool outflow, heat low and Eastern Mediterranean sea-breeze

During the night from 05 to 06 September 2015 a convective system exists over the Turkey-Syria border region. It is fuelled by the inflow along the eastern side of the RST. The system moves towards the north-east along with the mean flow direction above 500 hPa. Due to the favourable position of the convective system in front of the mid-tropospheric trough axis, it intensifies during the course of the night. However, in contrast to subsequent systems, it lacks the

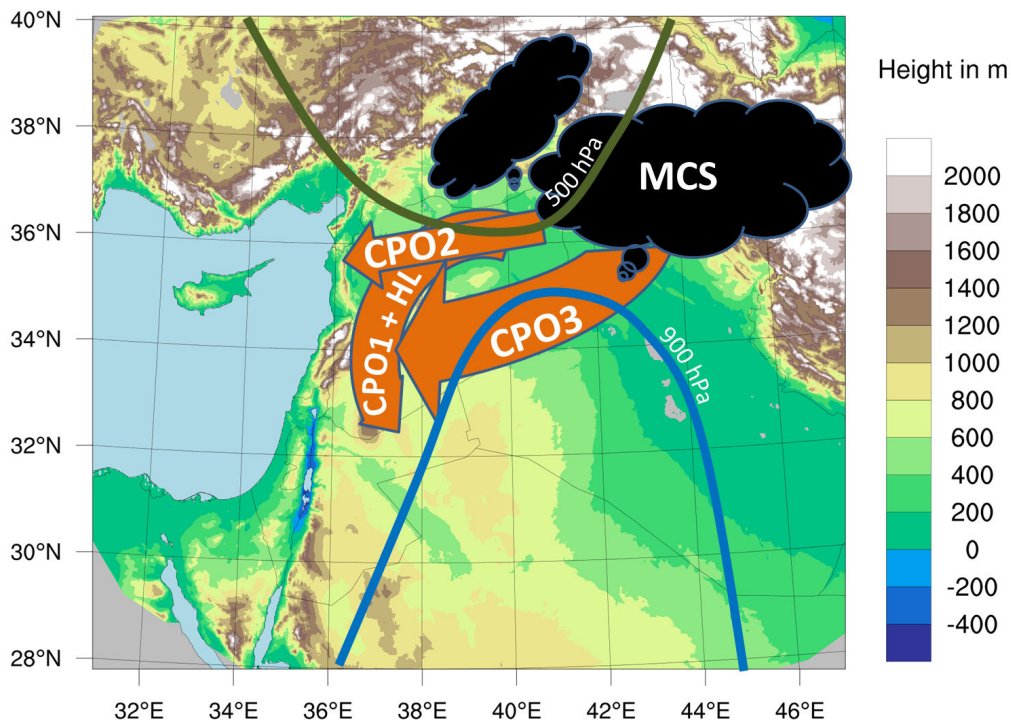


Figure 5.2: Schematic depiction the main dust event stages and atmospheric features. Coloured lines represent mean geopotential height of pressure levels. Labels refer to the description used in the text. Arrow size corresponds to event magnitude and arrowhead size to event speed. Timing of the events stages is provided in figure 3.4.

full meso-scale organization of convection, possibly due to less favourable wind-shear conditions. During the early morning hours of 06 September 2015, the convective system produces a first, weak cold-pool outflow (termed CPO1 in the following) which remains decoupled from the surface due to the stable nocturnal boundary layer. As soon as the sun rises, the downward mixing of momentum increases and dust is picked up. The high surface wind speeds are intensified and sustained during the day by a strong and shallow heat low (termed HL in the following) forming in the developing boundary layer. The HL is located in the tip of the RST and centred above Syria where temperatures during 06 September reach values above 45°C.

The first stage of the event is analysed in detail at 08 UTC 06 September. The ICON-ART simulation results displayed in figure 5.3 show the existence of a cyclonic flow around the developing HL. In addition, a marked maximum in the wind fields exists in the north-western part of Syria with a region where the wind velocity vectors do not follow the cyclonic flow but are oriented in parallel (solid black line in fig. 5.3 b)). Furthermore, the wind velocity exhibits a noticeable gradient at the edges of this structure. The increased 2m-dew point temperature (2m-DPT) inside the structure enables the identification as a weak CPO from the convection over the Taurus mountain range (fig. 5.3 d)). This is confirmed by an analysis of earlier time steps where the CPO1 is seen to originate as a single, circular shaped downburst structure in 2m-DPT in the Syria-Turkey

border region at 22 UTC 05 September (not shown). From the combined cloud cover and rainfall simulation results it is apparent that an organization of the convective cells does not occur in the model (fig. 5.3 c)), this explains the weak intensity of the CPO1. The cyclonic flow and CPO1 develop during the night already, however intensified dust pick-up and an increase in dust optical depth (DOD) is only simulated from 05 UTC onwards. The timing matches sun-rise and an increase in turbulent boundary layer mixing. The DOD at 08 UTC reaches peak values above 2 in central Syria already. Interestingly, structure and magnitude of dust pick-up are only partially correlated with the wind field distribution. This is due to the different soil types in the region, which become less emissive towards the Taurus mountain range. Over the course of the next three hours the DOD reaches values above 2 in a much larger part over Syria and in a narrow band of high wind speeds around the RST.

Another dominant flow characteristic visible in the wind field is the southerly flow around the RST over large areas of Iraq and Saudi-Arabia (dotted black line in fig. 5.3 b)). The high 2m-DPT in the region with values above 20°C illustrates the hot and humid character of the air mass which is advected from the Persian Gulf region. During the night from 00 UTC to 05 UTC the southward propagating CPO1 causes lifting of the southerly flow over Iraq, which at the time shows even higher values of 2m-DPT above 25°C (not shown). The lifting caused by the density current fuels the convection over the Taurus mountains. Another feature identifiable is the intrusion of the Mediterranean Sea breeze far inland towards the east (dashed black line in fig. 5.3). It is much better detectable during early stages of the night before humidity is distributed away from the surface by boundary layer mixing (not shown). However, the shaping of the inland flow by the orography along the Dead Sea Rift Valley is still recognizable.

A comparison of simulation results with the above discussed satellite instruments is shown in figure 5.4. From the SEVIRI dust product image it is apparent that the overall cloud cover is simulated well by ICON-ART (fig. 5.4 b)). However, two deep convective cells over the Turkey-Iraq border region are not captured by ICON-ART, these are also detectable in the MODIS-VIS satellite image (fig. 5.4 c)). The simulated DOD compares well to the optical depth measured by TERRA MODIS (fig. 5.4 d)). The overall spatial structure and magnitude of the mineral dust distribution is in good agreement, with peak DOD values reaching 2 in measurement and simulation. The upstream RST region shows values of comparable DOD magnitude between MODIS and ICON-ART as well. The high values of dust in the atmosphere have spread further south-west by approximately 1° in the observations compared to ICON-ART simulations. In addition, the northern boundary of the DOD in the HL and CPO1 region is more sharply defined in all measurements compared to ICON-ART and coincides with the southern edge of the cloud cover. Furthermore, the peak DOD structure is more oriented in a north-south direction in reality than it is the case in ICON-ART. All of the above findings are most likely related to a less well structured MCS development in ICON-ART compared to reality, resulting in a weaker CPO1. Possibly, this is due to the smoothed orography of the Taurus mountains in ICON-ART which is expected to shape the convective development and CPO1 structure.

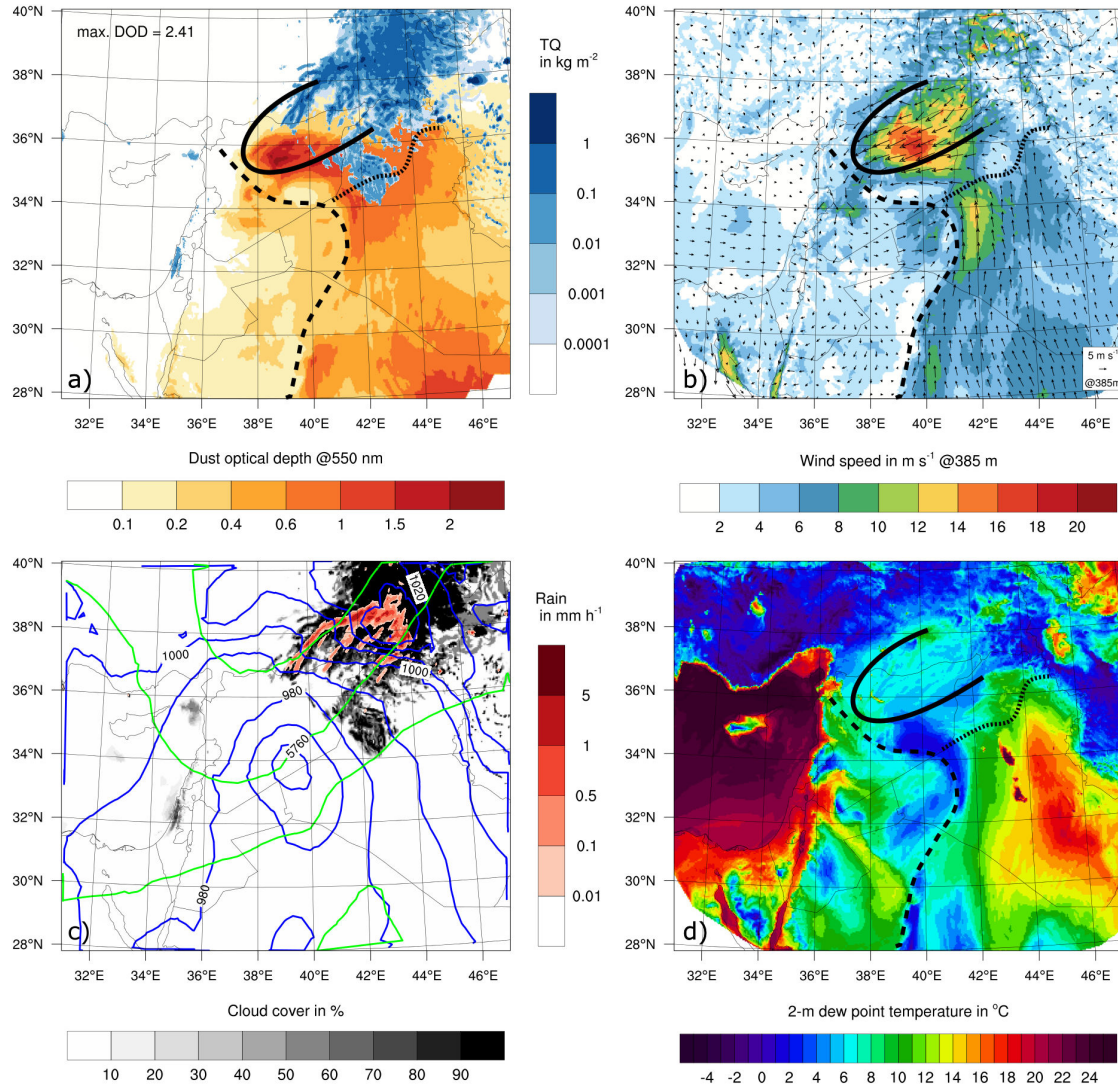


Figure 5.3: ICON-ART model results at 08 UTC 06 September. Solid black line marks CPO1, dashed black line EM Sea-breeze front from 05 September, dotted black line inflow frontal structure. Displayed are: a) Dust optical depth at 550 nm overlain with column integrated hydrometeor content TQ (cloud water, cloud ice and graupel). b) Wind speed at 385 m model height and wind velocity as vectors. c) Fractional cloud cover and surface rain rate colour coded. Blue lines show geopotential height of 900 hPa level at 10 gpm intervals, green lines show geopotential height of 500 hPa level at 20 gpm intervals. d) 2m-dew point temperature.

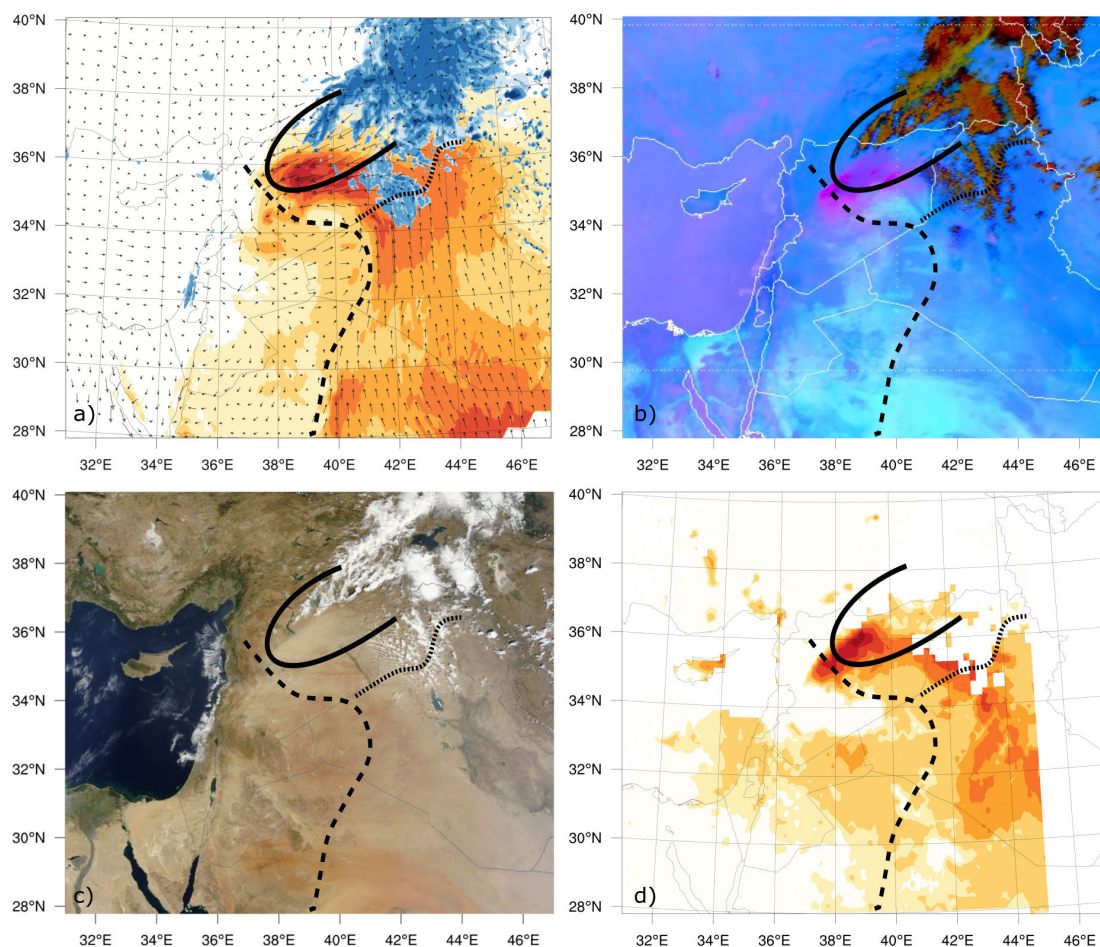


Figure 5.4: ICON-ART model results and satellite observations for 08 UTC on 06 September. Axis for dust optical depths, column integrated hydro-meteor content and event marks as in figure 5.3. Displayed are: a) ICON-ART dust optical depth, column integrated hydro-meteor content and wind velocity. b) SEVIRI RGB dust product (Kerkmann et al., 2015). c) Terra MODIS VIS satellite image, overpass at 08.15 UTC (NASA Worldview, 2016). d) Terra MODIS dust optical depth retrieval using DB2 algorithm (AOD-0.3) (Levy and Hsu, 2015), overpass at 08.15 UTC.

Further course of events - Interaction of atmospheric drivers

During the course of the day, the flow structure created by the CPO1 outflow in combination with the heat low above Syria interacts with the land inward penetrating sea breeze from the Mediterranean Sea, creating strong southward transport of dust towards Jordan (not shown). From 10 UTC onwards, the atmospheric instability created by boundary layer heating and upper level cold air advection is released and deep convection starts to develop over the Syria-Iraq border region and Zagros mountain range in the RST inflow region. From SEVIRI Meteosat satellite images a second, convective cold pool outflow which travels west from the Zagros mountain range is detectable at 12 UTC (CPO2). This CPO2 travels fast towards west in the westerly flow structure of the RST and heat low. The lifting caused by the gust front of the CPO2 triggers initiation of deep convection over the Syria-Iraq border region which organizes into a MCS around 18 UTC. By this time the CPO2 has already travelled far into Syria. The MCS starts to develop

a marked, third cold pool outflow (CPO3) from 20 UTC onwards. The CPO3 travels in the wake of CPO2, but in a more southerly direction. The CPO3 outflow towards the south counters the inflow from southerly directions along the eastern flank of the RST, thereby lifting the warm and moist air masses. Just before the further, explosive intensification of the MCS due to this lifting the next in-depth analyses is conducted.

As mentioned in section 3.2, the reinitialization of ICON-ART with IFS at 12 UTC corrupts the CPO2 development due to the termination of convective structures. However, the main flow structures are still captured as is shown in the next section.

5.2.2 Meso-scale convective system development and cold-pool outflows

The next in-depth analysis is conducted on 00 UTC 07 September due to a CALIPSO overpass which occurred at 23.35 UTC 06 September and thereby enables an analysis of the vertical dust plume structure. The meteorological analysis of the situation as simulated by ICON-ART is shown in figure 5.5.

Above the northern tip of Iraq a MCS exists which produces rainfall in its southern part. The cirrus clouds are transported towards north-east by the upper level flow (fig. 5.5 c)). The dominant feature visible in the simulated wind field is the aged CPO2 which has spread towards west over the previous 12 hours and is about to cross the 38° E meridian (central black solid line in fig. 5.5). Furthermore, the simulated wind-field shows a strong and marked gust front at the southern edge of the MCS (eastern black solid line in fig. 5.5 b)). This structure is the developing CPO3, it is driven by northerly flow behind its leading edge with peak wind speeds above 20 m s^{-1} . The gust front counters the southerly inflow connected to the RST. The counter-flow causes lifting of the hot and humid air mass flowing in from the south due to the greater density of the CPO3, thereby enabling further development of the MCS. In addition, the CPO3 is deflected towards west along the circular shaped gust front in line with the general cyclonic flow caused by the RST during the next hours.

An analysis of the 2m-DPT confirms the CPO3 structure and humid character of the inflowing air mass (5.5 d)). Above central Syria the previously discussed CPO2 is visible and in good agreement with the wind field structure. The previously discussed combination of CPO1, HL and sea breeze is recognizable by its edge located over the Syria-Jordan-Iraq border region (development not shown, western solid and dashed black line in fig. 5.5). Interestingly, the surface near 2m-DPT leading edge is not detectable in the 385 m wind speed field, this probably is the result of a strong surface near night-time inversion decoupling the flow.

Investigating the simulated DOD, a multitude of effects are apparent. The raised concentrations behind the leading edge of the aged CPO1 are visible with values of the optical depth up to 1 (fig. 5.5 a)). Furthermore, the leading edge of CPO2 is also visible in the optical depth field with values reaching 1 in the leading edge region over central Syria. Interestingly enough, the strong gust front travelling south in connection with the developing CPO3 is not yet detectable through higher DOD values. As was mentioned before, this remains the case until 05 UTC when intensive dust pick-up occurs as soon as boundary layer mixing increases after sunrise. This finding also

allows for the conclusion that the spreading CPO3 remains mostly decoupled from the surface during the early hours, thereby favouring its fast and wide spread over a large area as is shown in the next section. It also highlights the importance of modelling the night-time boundary layer structure correctly, which is strongly influenced by the mineral dust radiative effect as is shown in section 5.3.

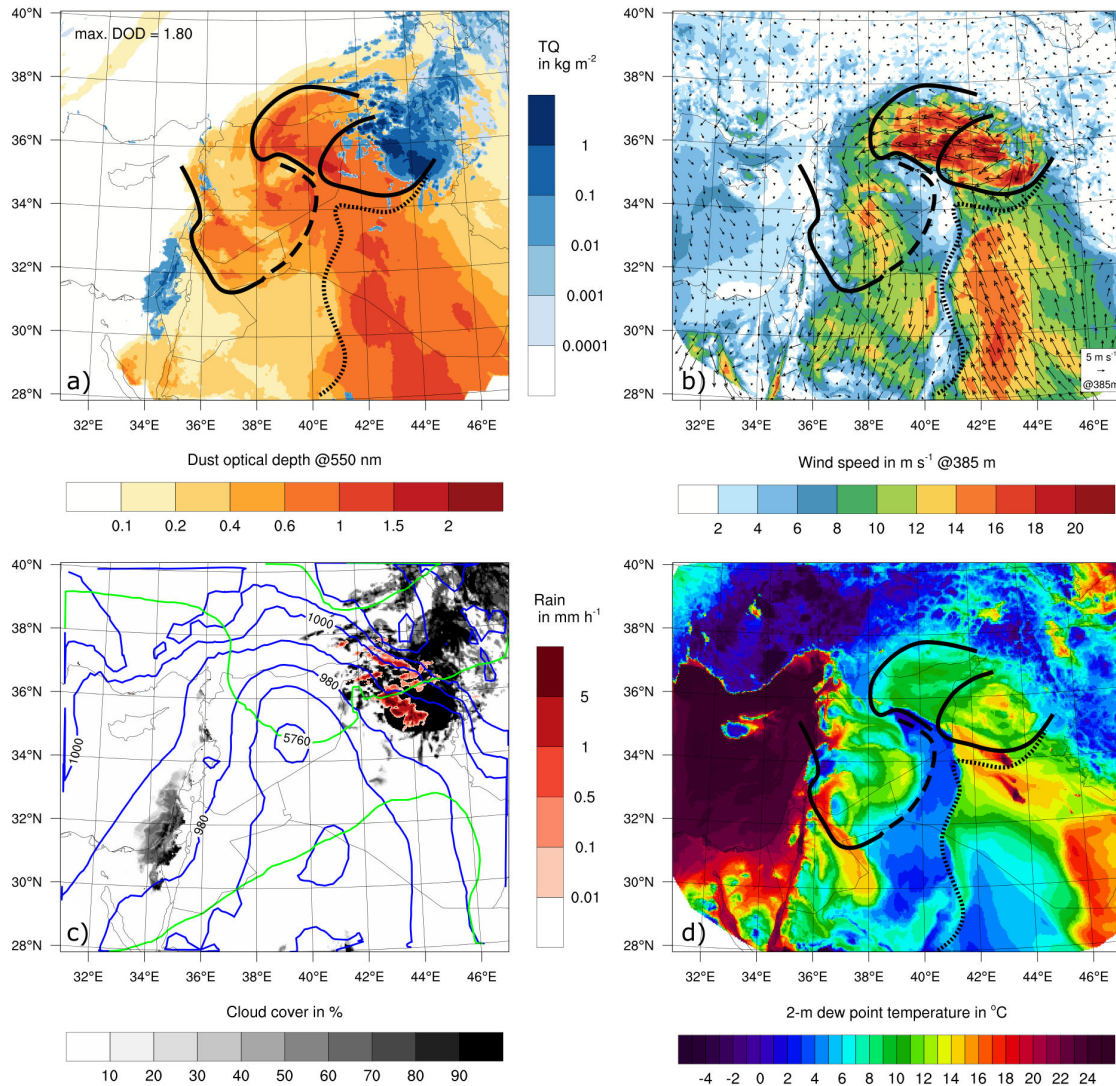


Figure 5.5: ICON-ART model results at 00 UTC 07 September, same as figure 5.3. From west to east solid black mark leading edges of CPO1, CPO2 and CPO3. Dashed line marks EM Sea-breeze front from 06 September. Dotted line marks frontal region of inflow.

Comparing the ICON-ART simulation results with SEVIRI dust product images shows that the structure and location of the MCS are well captured in the model (fig. 5.6 b)). A slightly greater extent of the deep convection towards north-east can be inferred from the satellite images due to the persistently reddish colours in this area. The almost radial cloud structure in the in- and outflow regions of the MCS can be seen in both figures, suggesting a well represented inflow

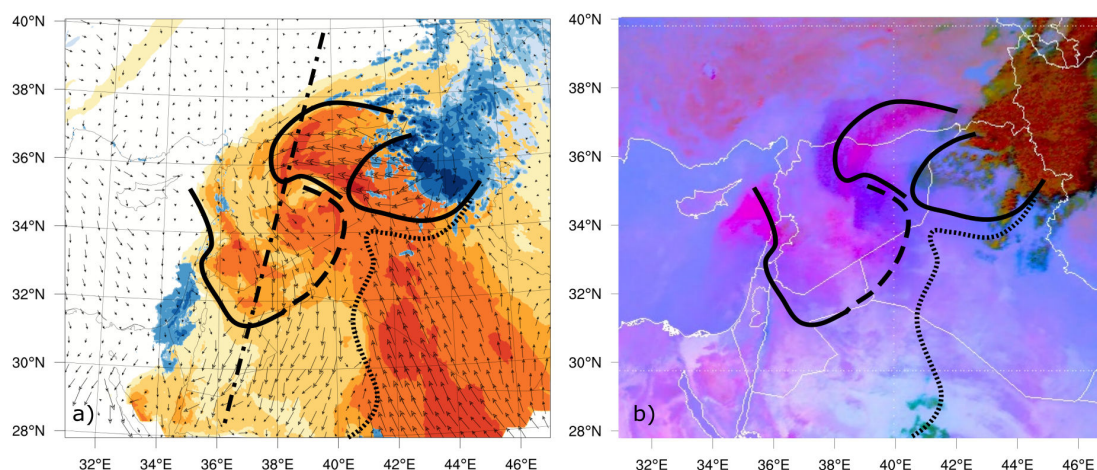


Figure 5.6: ICON-ART model results and EUMETSAT satellite observations for 00 UTC on 07 September. Axis and event marks as in figure 5.5. Chain dotted black line marks CALIPSO ground track at 23.35 UTC 06 September. Left side: ICON-ART dust optical depth, column integrated hydro-meteor content and wind velocity. Right side: SEVIRI RGB dust product.

regime in ICON-ART. The CPO2, identifiable by a dark shadow, has advanced further west in the satellite observations. Its structure is not connected to the main dust plume in the leading edge region. A very good agreement exists between the simulated leading edge of the dust plume in observations and model, with both showing the arched shaped structure in the same location. Unfortunately, quantitative comparisons of the DOD magnitude are not possible using the SEVIRI dust product.

A marked difference in DOD distribution exists in the EM west of the Lebanese coast. In the SEVIRI dust product a dust plume is already visible in the region, whereas this plume is missing in the ICON-ART results. An analysis of dust product images at high temporal resolution discloses that this plume is rapidly transported into the region by the CPO1 past noon on 06 September (not shown). Three reasons explain why ICON-ART is not able to simulate this structure. Firstly, it does not develop an as well defined CPO1 as observed in reality. Secondly the CPO1 is oriented slightly different, influencing its interaction with the complex topography in the region. Thirdly, the already discussed reinitialization of ICON-ART at 12 UTC can also be influential. The lack of this dust plume in ICON-ART continues to affect the simulations of DOD in the EM as it lacks the pre-loading of the area with dust.

The left side of figure 5.7 provides a vertical cross-section of the model results along the CALIPSO ground track (chain dotted black line in fig. 5.6). The total attenuated backscatter measured by CALIOP is displayed on the right side. From south to north the track passes through a sequence of features. At first, the background field with low concentrations of mineral dust is encountered south of 31° N. Dust concentrations in this region are low and the plume extends homogeneously throughout the boundary layer up to four kilometres altitude in both measurement and simulation. North of 31° N an increase in extinction coefficient and total attenuated backscatter is apparent. It shows the dust plume created by the aged CPO1 in combination with the HL. Both, simulations

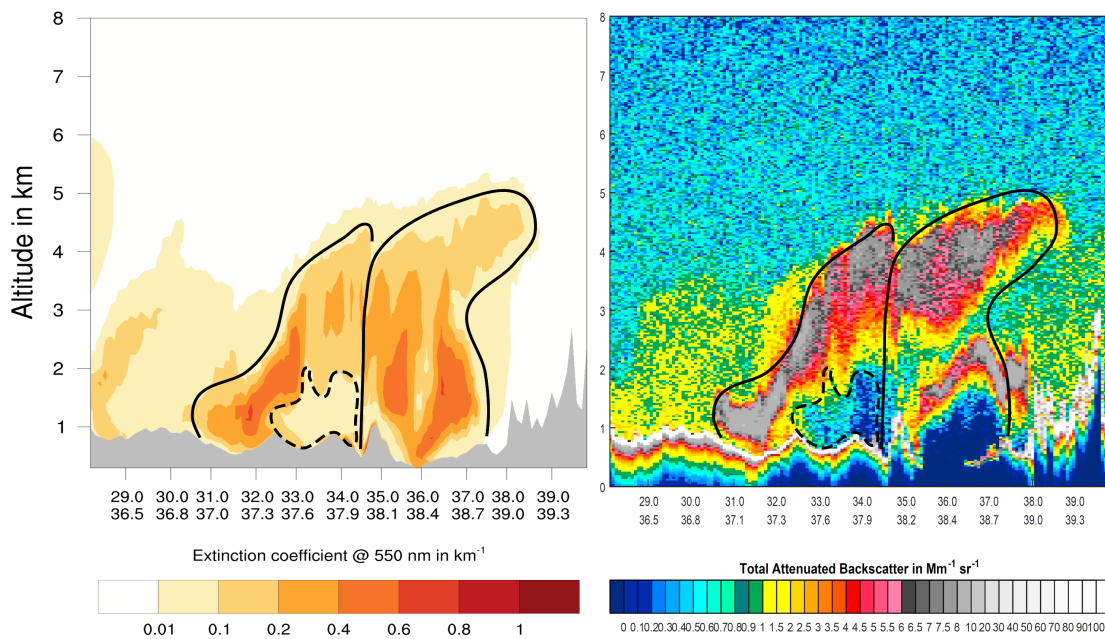


Figure 5.7: Vertical cross-section of ICON-ART model results for 00 UTC on 07 September and CALIPSO satellite observations from south to north along ground track in figure 5.6. Left side: ICON-ART mineral dust extinction coefficient. Right side: Total attenuated backscatter as measured by CALIOP. No quantitative comparison is possible as two different measures are displayed. Southern solid black line marks CPO1 and HL region. Dashed line marks penetrating EM Sea-breeze. Northern solid black line marks CPO2 region.

and measurement, show an increasing elevation of the level with highest dust concentrations from the surface layer at $31^{\circ} - 32^{\circ}$ N up to 2 – 3 km altitude at 33° . This feature can be explained with the dust plume being undisturbed in the southern part, whereas it has interacted with the penetrating Mediterranean sea breeze with low dust concentrations in the northern part. As the EM sea breeze shows cooler characteristics than the dust plume (not shown) it causes lifting of the plume (compare figure 5.5). A near surface minimum in dust concentrations due to this interaction is apparent from $33^{\circ} - 35^{\circ}$ N with similar features in both simulation and measurement. At 34.5° N, 38.0° E the leading edge of CPO2 is encountered in both simulation and measurement. The distinguishing features are a abrupt change in vertical structure of the dust plume, denoted by a sharp decrease in plume height. The change is also detectable in line shaped structures at lower levels. Northwards and inside the CPO2 a second maximum is visible near the surface with an altitude up to 2 – 3 km. This surface near maximum extends north to 37.5° N in the simulation and 38° N in the CALIOP measurements. The slightly further extend in reality is due to the further spread of the CPO2 (compare SEVIRI dust product). The high values of the extinction coefficient simulated near the surface do not show in the measurements as the lidar signal is attenuated on its way through the dust plume. Consequently, not enough signal strength which can be evaluated is left at altitudes below 2 km which is marked as 'no signal' in the vertical feature mask (not shown). A feature which shows excellent agreement between ICON-ART and CALIOP is the increasing dust plume top height up 5 km towards the north. Furthermore, the overarching structure

towards the Taurus mountains can be seen in both results.

Summarizing, the comparison of results at 00 UTC 07 September shows high agreement between simulations and measurements, both in spatial and vertical extent of the dust distribution. The results highlight the modelling capabilities of ICON-ART with respect to convection permitting simulations.

Further course of events - MCS intensification and CPO3 production

Over the course of the next two hours, and explosive intensification of the MCS takes place due to the favourable atmospheric conditions. It develops a sharply defined, curved rainfall pattern in front of which the CPO3 is formed. An intermediate time step of the meteorological analysis is shown in figure A1. It is not discussed further but used in section 5.3 to investigate the night-time radiative effect of mineral dust. In connection with the only slowly advancing upper atmospheric trough, which causes quasi-geostrophic forced ascent, and the orographic support from the Zagros mountain range, the MCS remains quasi-stationary over the next 12 hours. Due to the long duration and separation of the up- and down-draft region the MCS is able to produce an enormous amount of cool, moist air and a mighty CPO3 downstream a line shaped rainfall pattern. During the course of the night, the southerly direction of the CPO3 is deflected into a westerly flow direction by the RST flow structure and its inflowing air masses. The night-time spread of the CPO3 towards west is crucial due to its subsequent interaction with the developing boundary layer mixing during daytime. Dust pick-up in CPO2 and CPO3 is limited during the night but increases as soon as boundary layer mixing increases due to solar insolation. At 10 UTC 07 September all satellite platforms are available and the next in-depth analysis is conducted.

5.2.3 Mature stage of third cold-pool outflow

ICON-ART model results at 10 UTC 07 September are displayed in figure 5.8. The simulated MCS has passed its most intensive development stage approximately four hours earlier. The main MCS features are still visible, although it is in the stage of dissolution due to the shift of the upper atmospheric trough towards east (fig. 5.8 c)). The convection is organized along the orographic features of the Zagros mountain range, exhibiting a sharp line shaped rainfall distribution. Possibly, the convective structure is also shaped by a weak cyclogenesis taking place further east due to the favourable upper-tropospheric conditions there. The cirrus cloud anvil extends far to the north-east as it is transported away by the upper level flow. Downstream the line-shaped rainfall distribution near surface wind speeds increase strongly as the CPO3 reaches the surface (fig. 5.8 b)). Wind speeds above 15 m s^{-1} are modelled and the southern edge of the CPO3 is distinct. The edge is also easily recognizable in the 2m-dew point temperature field, the difference in 2m-DPT between the CPO3 and the surrounding air masses is approximately 10°C (fig. 5.8 b)). Due to the timing of the analysis around noon local time, dust has been picked up in large quantities over the previous hours with increasing boundary layer turbulence and DOD values above 2 are modelled in the CPO3 region (fig. 5.8 a)). The maximum DOD value is 4.15, it is reached in an area close to the leading edge of CPO3 which shows the highest values of DOD.

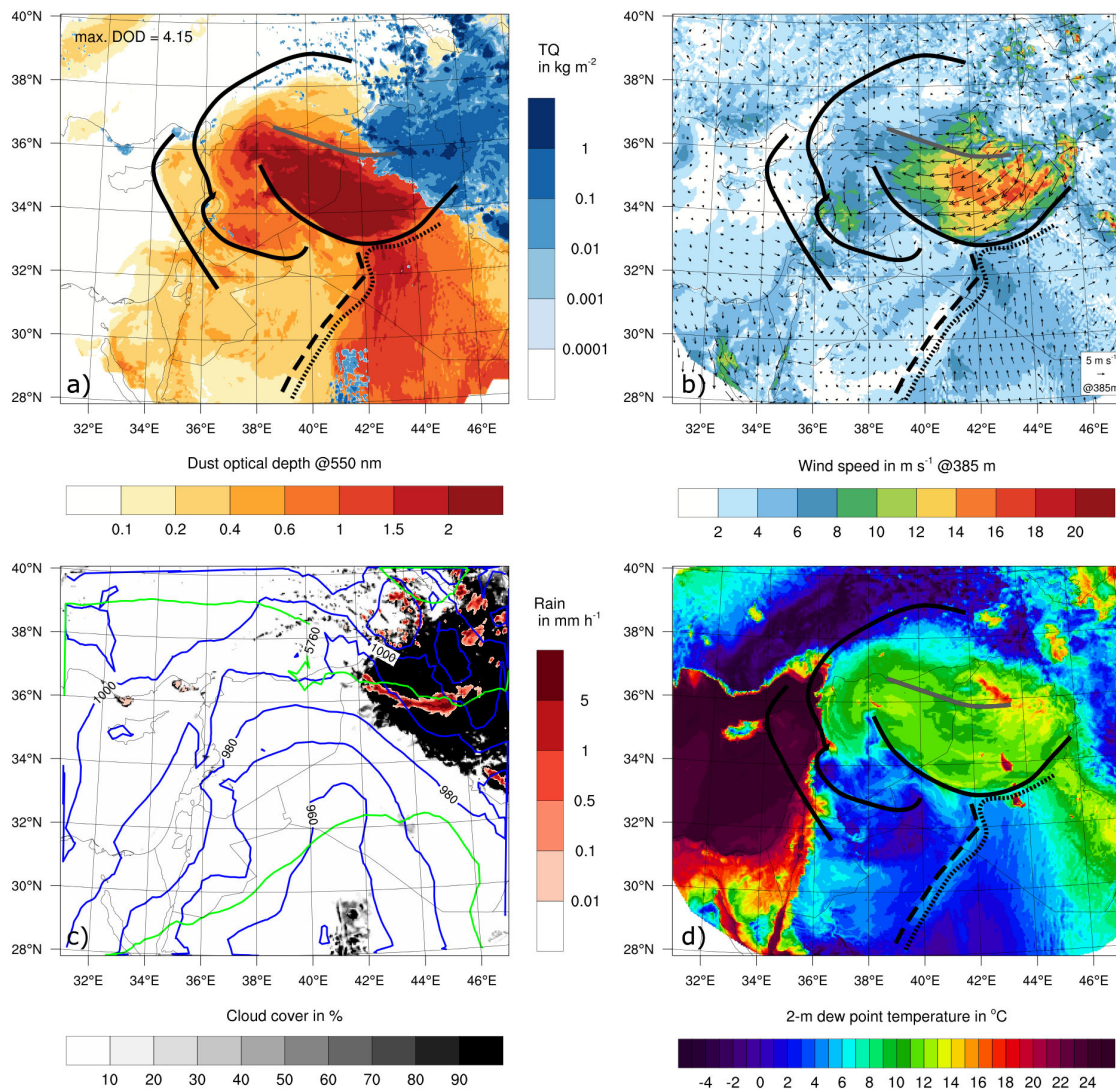


Figure 5.8: ICON-ART model results at 10 UTC 07 September, same as figure 5.3. From west to east solid black lines mark leading edges of CPO1, CPO2 and southern CPO3 boundary. Gray line marks northern dust plume boundary inside CPO3. Dashed line marks merged EM Sea-breeze front from 05 and 06 September. Dotted line marks frontal region of inflow.

Towards north, the DOD exhibits a sharp gradient (northern boundary of CPO3 dust plume in fig. 5.8). At closer inspection of the wind and dew point temperature fields it becomes apparent that the decrease in DOD is not linked to the extent of the CPO3 in north-western Syria (fig. 5.8 b) and d)). Remembering the orography and the soil-type distribution in the region (fig. 2.6, 2.10), it is clear that a change in soil type towards less-emitting light clay and the increase in elevation are responsible for a reduced DOD in this region. This is similar to the feature discussed in section 5.2.1 for CPO1. The northern edge of the aged CPO2 is marked by a line of convective clouds over the Taurus mountain range, here a second but less distinct gradient in DOD is visible (northernmost black line in fig. 5.8). In the south-western part of Syria, entering Jordan, the remains of CPO2 are also still detectable by an elevated DOD above 1 and higher wind speeds up

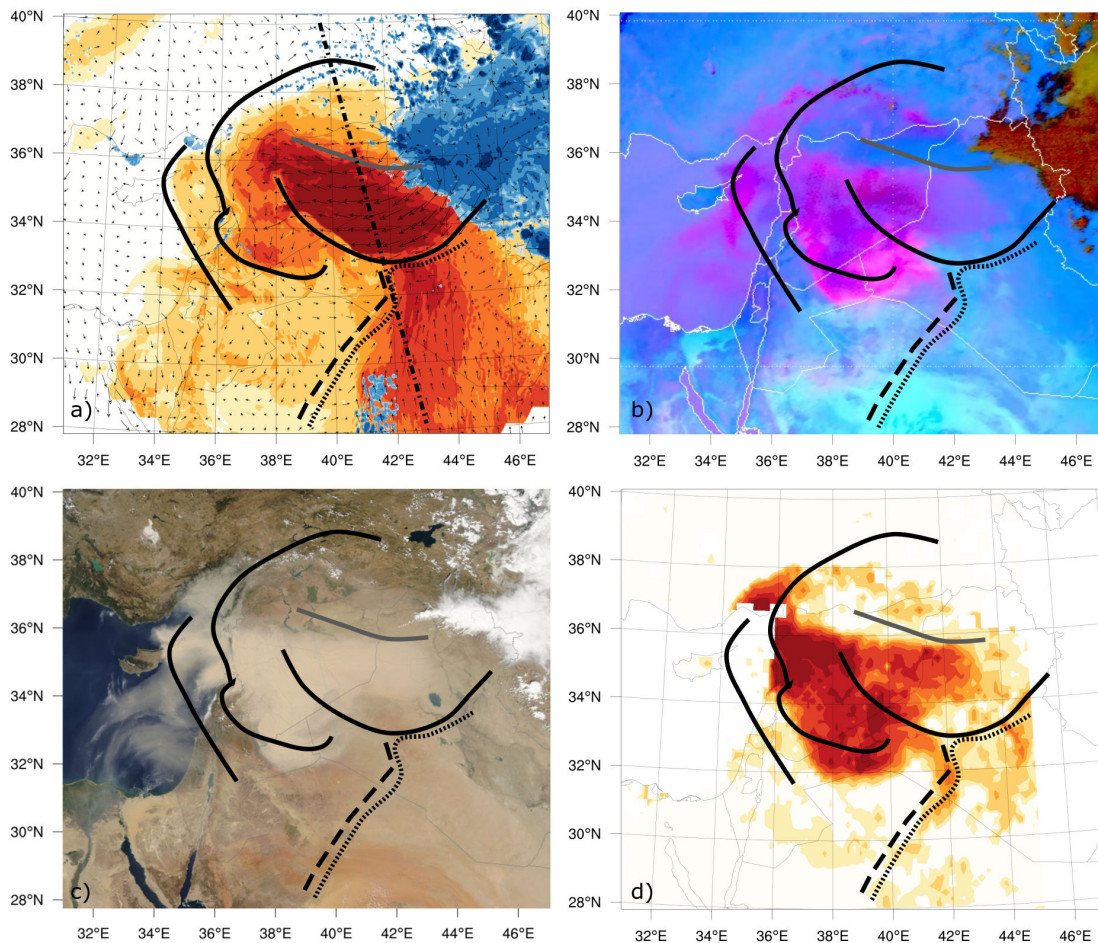


Figure 5.9: ICON-ART model results and satellite observations for 10 UTC on 07 September. Same as figure 5.4 but for Aqua MODIS instrument, overpass at 10.35 UTC. Axis and event marks as in figure 5.8. Chain dotted black line marks CALIPSO ground track at 10.35 UTC.

to 10 m s^{-1} . In addition, at a closer look the formation of small convective clouds above the nose of CPO2 can be seen in the ICON-ART model results. The aged CPO2 re-intensifies and the arc clouds develop further during the course of the day (not shown).

In figure 5.9, ICON-ART model results and the corresponding satellite observations are displayed. A comparison of the SEVIRI cloud cover with ICON-ART results shows that the cirrus anvil of the MCS has a greater lateral extension in the model, whereas it is confined around 36°N in the observations (fig. 5.9 b)). In addition, the MCS has moved further east by approximately 2° in reality. Taking the area with the brightest colour as a proxy for the most deep convective area, the MODIS visible satellite image (fig. 5.9 c)) shows good agreement with the line of highest integrated hydro-meteor content in ICON-ART (fig. 5.9 a)).

The structure of the MCS determines the shape of the outflow, therefore differences in outflow structure can be identified as well. Again, the CPO3 is more sharply confined between 34°N and 36°N in the observations, whereas it shows a bow shaped southward extension beyond 34°N in ICON-ART. The northward boundary of CPO3 is modelled accurately, with a northward deviation

at the western tip. Modelled DODs are higher in ICON-ART when compared to MODIS AOD in the eastern part of CPO3 and lower in the western part of CPO3 (fig. 5.9 d)). Over sea no measurements are available due to the bright target algorithm used. For the eastern part of CPO3 the MODIS AOD measurements seem doubtful when comparing to the MODIS visible satellite image (although it is reduced by a value of 0.3, the discrepancy is much larger than this).

The aged CPO2 spreading towards the north is detected by all satellite instruments, it is modelled with an offset towards the north-east by ICON-ART (northernmost solid black line in fig. 5.9). Noticeable are arc clouds forming above the Taurus mountains in simulation and reality. The south-western boundary of the aged CPO2 is modelled correctly in the Golan Heights region. However, towards the west and south the CPO2 has advanced further in reality than in the model, as all measurements show a southern edge of the CPO2 which is just about to cross the border into Saudi-Arabia. Aerosol optical depths retrieved by MODIS are in the range of 1.5 whereas ICON-ART simulates values in the range of 1. In this case, the MODIS measurements seem more realistic when compared to the visible satellite picture.

Summarizing, a northward deviation of the flow structure in ICON-ART can be identified both for CPO2 and CPO3 although the overall intensity and characteristics are modelled extremely well. The combination of the northern deviation towards less dust emitting soil types and the wider, less well defined main outflow region reduce the amount of DOD over western Syria due to a less intense channelling of the CPO3. Furthermore, the re-intensification of the aged CPO2 is modelled by ICON-ART, however, it was observed with greater magnitude in reality. The reduced amount of dust in the atmosphere in ICON-ART leads to a reduction in long range transport of dust towards the EM over night.

The vertical structure of the dust plume can again be investigated at this point in time with the help of a CALIPSO overpass which occurred at 10.35 UTC. Results along the flight track are shown from south to north in figure 5.10. The southern inflow region towards the MCS shows high values of the extinction coefficient in ICON-ART and attenuated backscatter in CALIOP measurements. The height of the dust plume is between 5 – 6 km, with decreasing height towards the MCS. Just south of the main CPO3 dust plume, in a region from 32 – 33°N both show a decrease in dust concentrations at upper levels. However, a difference exists in the near surface values up to 2 km, where CALIOP reports high values of total attenuated backscatter but ICON-ART shows a minimum in extinction coefficient. The reason for this difference becomes clear when looking at the CALIPSO ground track again in figure 5.9. By chance the satellite passes the region where the merged one and two day old sea-breezes from the Mediterranean penetrate the RST trough inflow in a cyclonic rotational movement. The process is not shown due to the long development time. However, the frontal structure is visible in figure 5.8 as a thin line in 2m-DPT, a gradient in DOD and a change in wind velocity along the front (as can be expected from a frontal structure). ICON-ART is able to simulate the re-intensifying sea-breezes, thereby enabling the above analysis, however no dust pick-up is connected with the frontal structure. This is due to the clay loam soil type with high residual soil moisture content in the region passed by the front. In reality however, dust was picked up by this frontal structure, this is detectable in all three satellite measurements (fig. 5.9). As a result, CALIOP reports high values of attenuated backscatter in

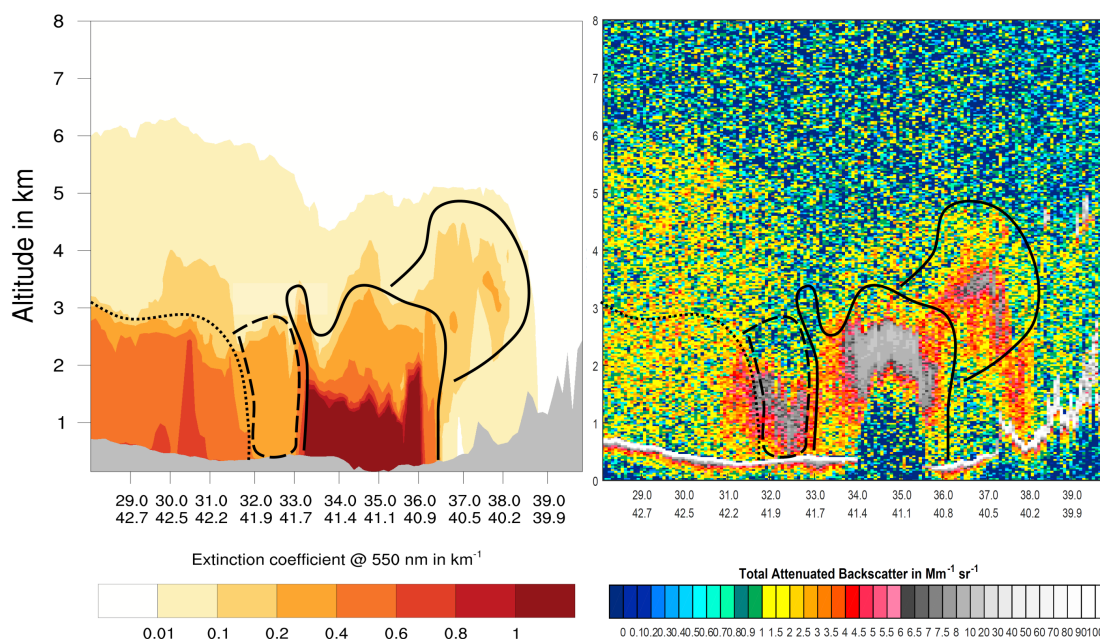


Figure 5.10: Vertical cross-section of ICON-ART model results for 10 UTC on 07 September and CALIPSO satellite observations from south to north along ground track in figure 5.9. Left side: ICON-ART mineral dust extinction coefficient. Right side: Total attenuated backscatter as measured by CALIOP. No quantitative comparison is possible as two different measures are displayed. Southern dotted black line marks inflow region. Dashed black line marks aged EM Sea-breeze penetrations region. Southern solid black line marks CPO3. Northern solid black line marks aged and lifted CPO2.

this region whereas ICON-ART simulates a minimum due to the clean air characteristics of the sea breeze.

The main CPO3 dust plume is distinct in both figures with ICON-ART simulating an elevated nose of the CPO3. The above discussed differences in CPO3 structure are identifiable again. ICON-ART simulates a wider and more shallow outflow whereas in reality it was more confined. In addition, the observations show an approximately one kilometre higher main dust plume compared to ICON-ART. As discussed above, altitudes below 2 km are marked as no signal regions in the feature mask due to the attenuation of the lidar signal (not shown). On the northern side of the plume beyond 36°N a minimum captured by both is visible, once more illustrating the well simulated northern boundary of the CPO3 in this region. Further towards the north the overarching dust plume structure consisting of dust picked up by the aged CPO2 is represented very similarly in simulation and measurement.

Further course of events - MCS dissipation stage and long-range transport

From 10 UTC onwards on 07 September, the MCS starts to dissipate and is in the course advected east along with the mean flow conditions above 500 hPa. The CPO3 air mass created during the night spreads south-west during daytime on 07 September. At all times it shows the characteristic features associated with CPOs such as an increase in surface wind speed, higher dew point tem-

peratures and an arc cloud forming above the leading edge during the afternoon hours. The high surface wind speeds and turbulent mixing inside the CPO3s result in enormous dust emissions during daytime, consequently the dust is transported within the full boundary layer height up to 5 km.

With nightfall on 07 September the CPO2 and CPO3 merge. As the merged CPO is still located in the western, downstream flank of the RST the air mass and dust contained within it are advected fast towards south-west over the course of the night. The Dead Sea Rift Valley is passed by the dust mass after midnight on 08 September, with the complex orography influencing the dust concentrations on the lee side of the mountain ranges. Section 5.4 investigates the timing and structure of the CPO arrival in Israel in reality and simulation and proves the existence of super-critical flow conditions in the region with connected hydraulic jumps. This flow phenomena and the related dust emission is responsible for extreme dust concentrations in the southern EM on 08 September.

During daytime on 08 September the dust plume is mostly stationary in the EM and influenced by the local circulation systems. In visible satellite pictures, the dust can be seen to remain in the EM at high concentrations over the course of the next four days. However, this period is not investigated as a part of this study as the scope of this work is the analysis of the generating mechanisms. Therefore, a last comparison of observed and simulated dust distribution and quantities in the region is conducted on 08 September at 11 UTC.

5.2.4 Aged dust plume in the Eastern Mediterranean

The last in-depth analysis is conducted at 11 UTC 08 September and thereby 47 hours past initialization of ICON-ART, a point in time at which none of the global dust models was able to forecast a realistic dust distribution in the EM. An overview of ICON-ART results is provided in figure 5.11. The main visible features in the DOD distribution are a peak in DOD with values above 2 offshore the Syrian coast as well as high values inland. Further south, a minimum exists in the region of the Lebanese mountain range and on their lee-side due to the blocking of the flow. Another maximum of DOD values is simulated offshore the Israeli coast. In this region the DOD is shaped by the orography of the Dead Sea Rift Valley as the main dust transport is accomplished through the Golan Heights gap (see section 5.4). In Israel and Jordan the DOD distribution is again shaped by the orography, with a maximum of DOD and values above 1 in the Dead Sea valley. Isolated non-precipitating convective clouds develop over the highest orographic features in the region in ICON-ART.

The wind field shows a weak cyclonic flow over Iraq and Syria and a stronger anti-cyclonic flow over the Sinai region. The 2m-DPT temperature field shows elevated values of dew point temperature in the remains of the CPO region. Furthermore, a land inward penetrating sea breeze is again detectable in the Dead Sea Rift Valley region as well as isolated downbursts in connection with deep convective cells over Iraq.

In figure 5.12 the simulated dust distribution can be compared to satellite measurements. The comparison with the SEVIRI dust product and MODIS VIS shows that the dust distribution in the

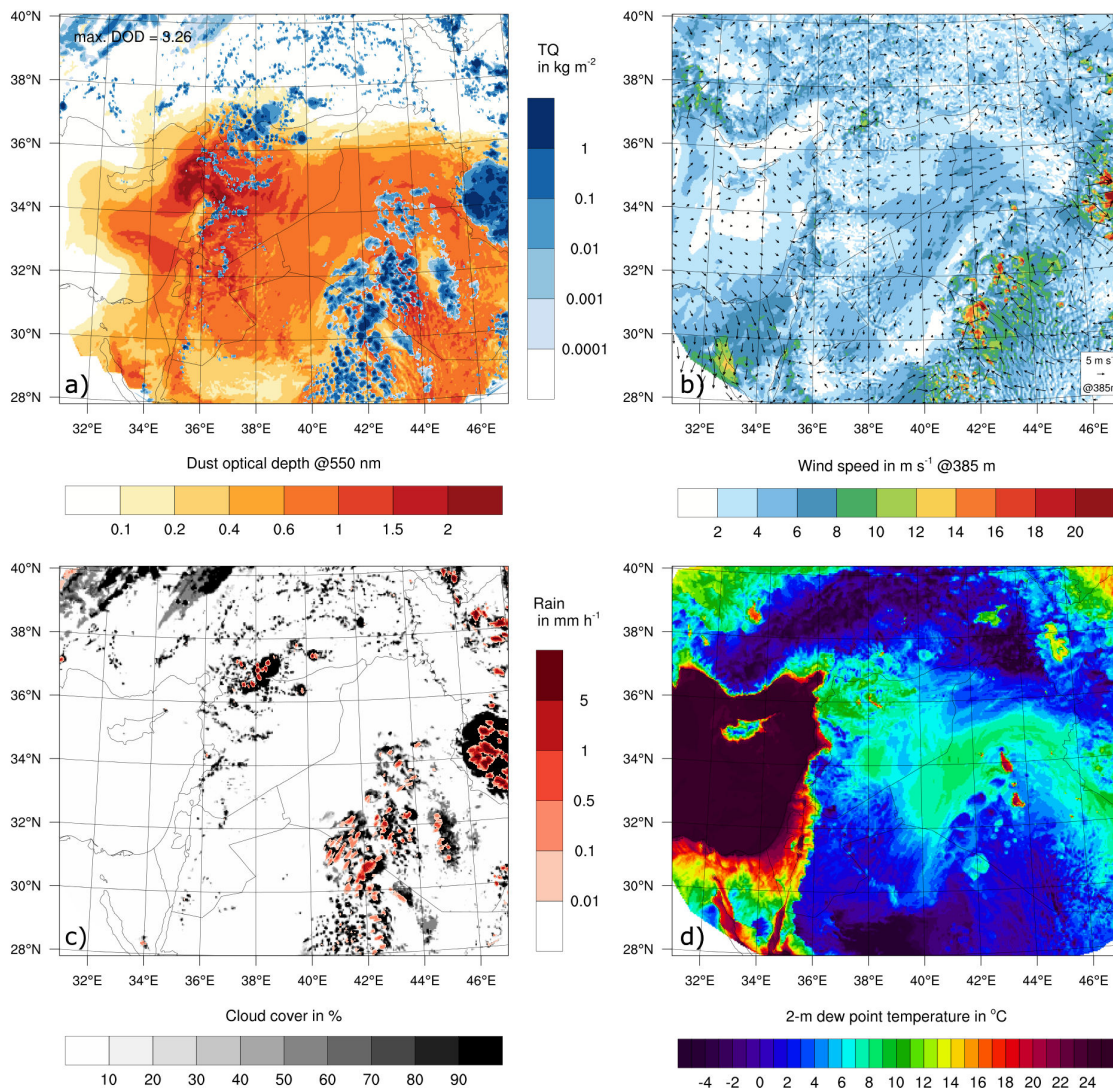


Figure 5.11: ICON-ART model results at 11 UTC 08 September, same as figure 5.3.

Syria shore region is captured well by ICON-ART. An arc shaped structure extending up to the Cyprus coastline is visible in all figures. In addition, a tip of the dust plume extending around Cyprus to the west is simulated by ICON-ART although with a too low DOD when compared to MODIS AOD and VIS. The underestimation is confirmed by assessments of the dust plume in Cyprus from which an aerosol optical thickness of 6 – 10 is estimated (Mamouri et al., 2016) (remote sensing instruments were unable to work because of the dust plume). Most likely, the too low DOD in the Cyprus region is due to the lack in pre-loading with dust from CPO1 and the slightly northward oriented CPO3. The minimum on the lee-side of the Lebanese mountain range detectable in SEVIRI and MODIS VIS is also visible in ICON-ART results, although it seems that the satellites detect higher dust concentrations above the Lebanese mountain range itself. Possibly, this is due to a too low dust plume in the model in this region which is strongly affected by complex interaction with the mountain range (see section 5.4). The convective cells which are simulated by

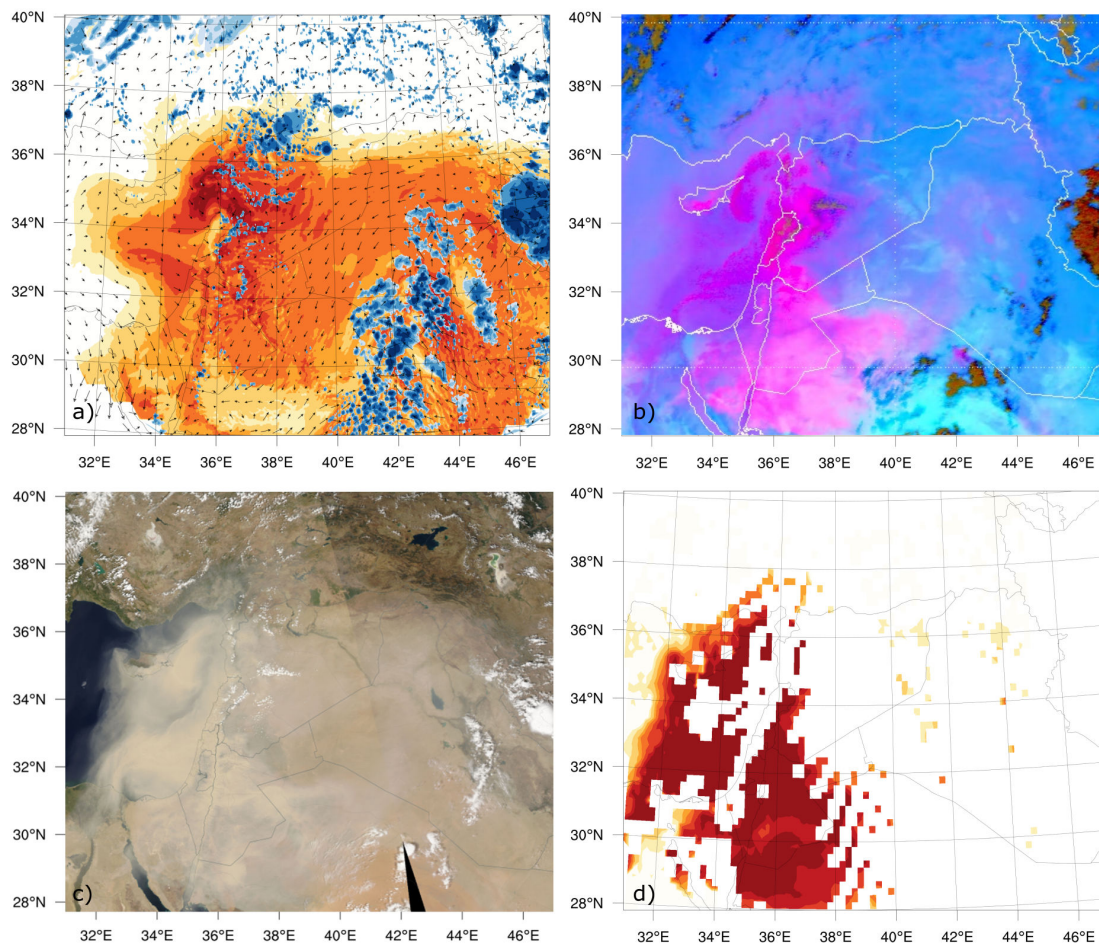


Figure 5.12: ICON-ART model results and satellite observations for 11 UTC on 08 September. Same as figure 5.4 but for Aqua MODIS instrument, overpass for the left part of the picture at 11.18 UTC. Please note that in this case the MODIS Dark Target and Deep Blue combined AOD product is displayed in order to obtain values over sea.

ICON-ART in the dust plume region are also visible in MODIS VIS. Summarizing, ICON-ART is able to simulate the characteristic synoptic scale flow and dust features in the northern part of the EM, but it underestimates the dust loading in some regions on the order of one magnitude. Keeping in mind the long simulation time at this point, and the fact that other models were off by the order of two magnitudes and unable to simulate dust transport beyond 35°E (Mamouri et al., 2016), the quality of the presented simulations becomes apparent.

Towards the southern part of the EM greater differences exist between model and measurements. The SEVIRI dust product and MODIS VIS show the main dust plume transported through the Golan Heights towards the Mediterranean in a position further towards the south-west. In opposition to this ICON-ART simulates a more westerly direction of the plume. Furthermore, the spread of the dust contained within CPO3 has advanced further south with higher concentrations in satellite measurements than in the model. In general the simulated DOD in the southern EM is below the values obtained by MODIS AOD which measures values above 2 in most regions. The MODIS AOD values seem plausible when comparing them with the SEVIRI dust product

and MODIS VIS. In discussing the differences between model results and observations one has to bear in mind the complex orography in the region and the importance of correctly timed and oriented CPOs. Because of the long simulation time and long-range dust transport small deviations in the initial conditions and generating meteorological systems can cause large differences in dust transport towards the EM. In order to investigate and validate the amount of dust transported towards Israel and its timing a comparison of model results with observations in the region is conducted in section 5.4. The detailed analysis also allows for conclusions on the reason for the failure of the model to correctly predict the dust transport towards the southern EM.

5.3 Influence of the mineral dust-radiation interaction

The validation of the mineral dust optical depth distribution and transport characteristics with satellite and station measurements show overall good agreement between ICON-ART and the observations, especially during the early stages of the event. The simulation therefore allows for investigation of the mineral dust radiative effect. This is not possible using measurements alone, as no control case exists for the real atmosphere. However, using ICON-ART the radiative effect of mineral dust can be studied in detail through the differences between the run including mineral dust radiation interaction (ARI) and without it (CTRL). An analysis of the mineral dust radiative effect on surface conditions is conducted at two characteristic points in time during the dust storm development. The first analysis is performed at 03 UTC 07 September as it shows interesting night-time features due to mineral dust. The second analysis investigates the day-time radiative effect of mineral dust and is done for 10 UTC on 07 September, this development stage is also analysed in section 5.2.3. In the third analysis, the mineral dust radiative effect on vertical atmospheric stratification is investigated. Last, the effect of the size dependent and consequently varying optical properties during transport is demonstrated.

5.3.1 Mineral dust night-time radiative effect

In figure 5.13 the differences between ARI and CTRL are depicted at 03 UTC 07 September. The point chosen is three hours later than the development stage discussed in section 5.2.2, just before sunrise in the region. The corresponding meteorological overview of the situation is provided in figure A1.

The mineral dust affected areas show the expected behaviour in terms of its influence on radiative transfer. The net global radiation at night is increased by values between $5 - 50 \text{ W m}^{-2}$, with higher values in regions with higher aerosol optical thickness (fig. 5.13 d)). The increase is caused by an increase in down-welling long-wave atmospheric radiation (not shown). The consequence is a reduction of the amount of energy radiated into space, which causes a night-time warming of the surface. The reductions in net global radiation towards the east are caused by the daytime effect of mineral dust, as the sun is rising in this region already. The 2m-temperature field outside the CPO3 and MCS region (which themselves are discussed further below) shows the expected behaviour for mineral dust at night with an increase in surface temperature for ARI (fig. 5.13 c)).

Also visible are smaller scale irregularities showing local temperature differences located outside the region affected by mineral dust. These are introduced due to the slightly different location and timing of convection in both runs. As values are mostly positive towards the north-west and negative towards the north-east there seems to be a systematic signal contained, possibly due to the feedback of MCS and CPO structure changes on large scale dynamics.

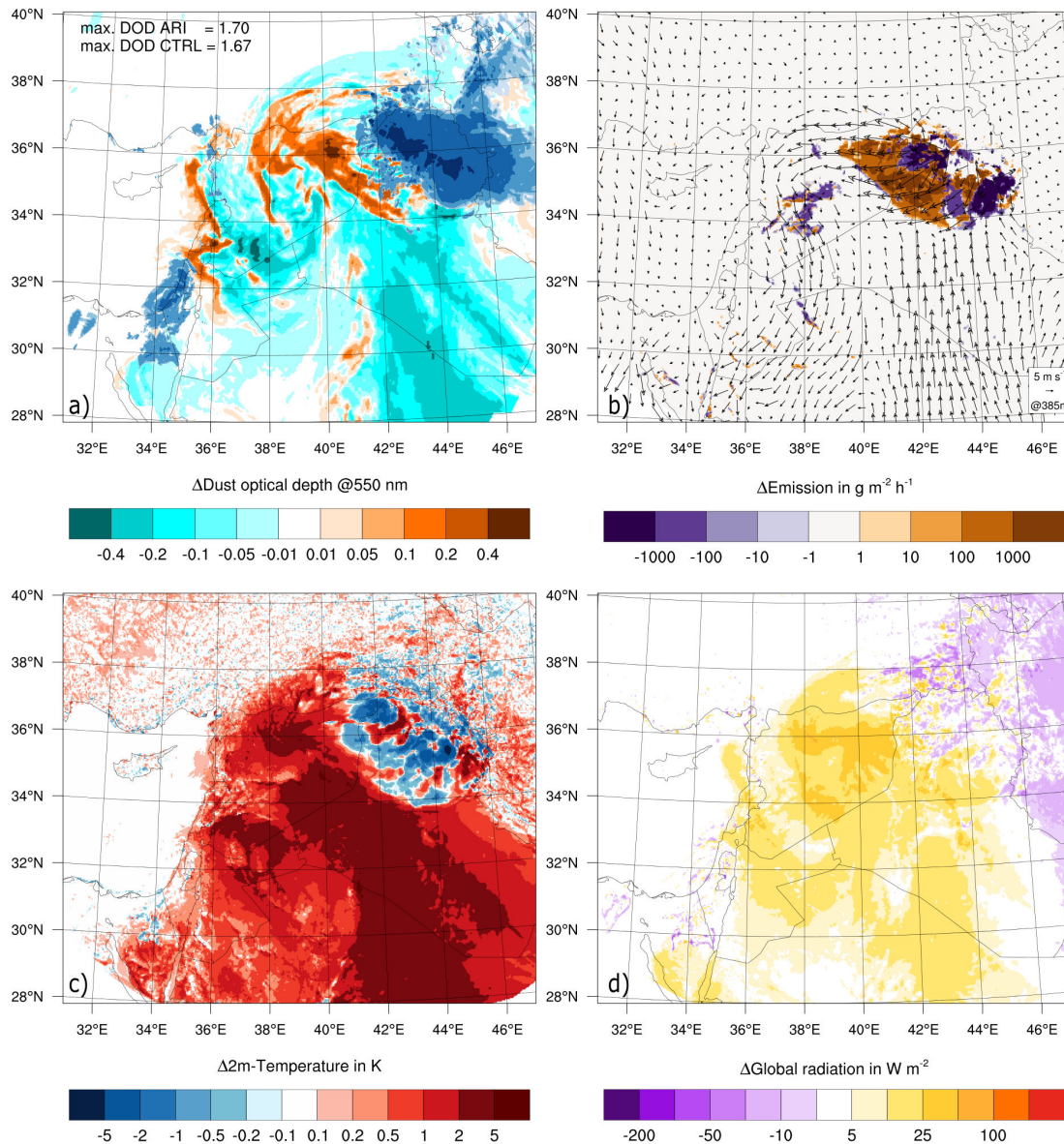


Figure 5.13: ICON-ART model results at 03 UTC 07 September, all results show ARI-CTRL. Displayed are: a) Column integrated hydro-meteor content as in fig. 5.3 and difference in dust optical depth. b) Wind velocity and difference in hourly mineral dust emission. c) Difference in 2m-temperature. d) Difference in net global radiation at the surface.

The magnitude of the temperature response to mineral dust radiative forcing is large when compared to other studies with values up to 5 K (see 2.2.2). A possible explanation are the high

values used for the imaginary part of the mineral dust refractive index in the near infra-red spectral region (see section 4.3.2), making the dust more absorptive. Interestingly, no homogeneously increased emissions are observed despite the decreased vertical stability outside the CPO3 area (fig. 5.13 b)). Consequently, the DOD is lower by more than 0.1 for most regions in the ARI run, although the maxima between runs are similar. This results from the decreased emission during the previous day with a more stable boundary layer during daytime (not shown).

The DOD difference shows regions with an increased DOD at the leading edges of the CPOs in ARI (fig. 5.13 a)). As the overall maxima of DOD are of comparable magnitude between ARI and CTRL, this can be attributed to a different propagation speed of the CPOs between runs. The CPOs in the ARI run show a higher propagation speed, which is not only detectable in the DOD but also wind speed and 2m-DPT signal, especially at later stages (not shown). In ARI, the CPO with its steep DOD gradient arrives earlier compared to CTRL, therefore a higher DOD is shown for in the leading edge region at the same point in time. Furthermore, the leading edge shows a more clearly marked DOD signal for the leading edge in the ARI simulation in general (not shown). The difference in DOD goes hand in hand with differences in dust emission which are also apparent in figure 5.13.

In order to understand the reason for this faster spread of the CPOs in runs including mineral dust radiation interaction we need to look at the 2m-temperature field again. Inside the CPO3 region a 2m-temperature cooling of more than 2 K can be observed for ARI (fig. 5.13 c)). This is the opposite of the expected mineral dust night-time effect as discussed above. However, the mineral dust radiative forcing in this region remains positive, as can be seen from the difference in global radiation. Therefore, the reason for the lower 2m-temperature must be different. A hint is provided by the difference in dust emission which increases in the ARI run despite a cooler surface, which again is not expected. All findings point towards a more intense CPO3 in the ARI run, which can explain all of the above observations.

A more intense and faster spreading CPO can have multiple reasons, the most important ones in this case are assumed to be:

1. More intense convection leading to more rainfall which can evaporate, this in turn cooling the CPO more. The intensity of the convection can be increased due to a warmer inflowing air mass because of the mineral dust radiative surface heating at night.
2. More potential for evaporation due to a warmer surface boundary layer, also creating a cooler CPO.
3. A more stable stratified and thereby less turbulent CPO, preventing the loss of energy due to turbulent friction.
4. Travel of the CPO into a less stable night-time boundary layer due to mineral dust radiative surface heating. Therefore, less potential and kinetic energy of the CPO needs to be invested in order to lift the stable night-time boundary layer in front. Due to the reduced resistance propagation speed can increase.

Unfortunately, a detailed analysis of the contribution of each responsible factors is beyond the scope of this work.

5.3.2 Mineral dust day-time radiative effect

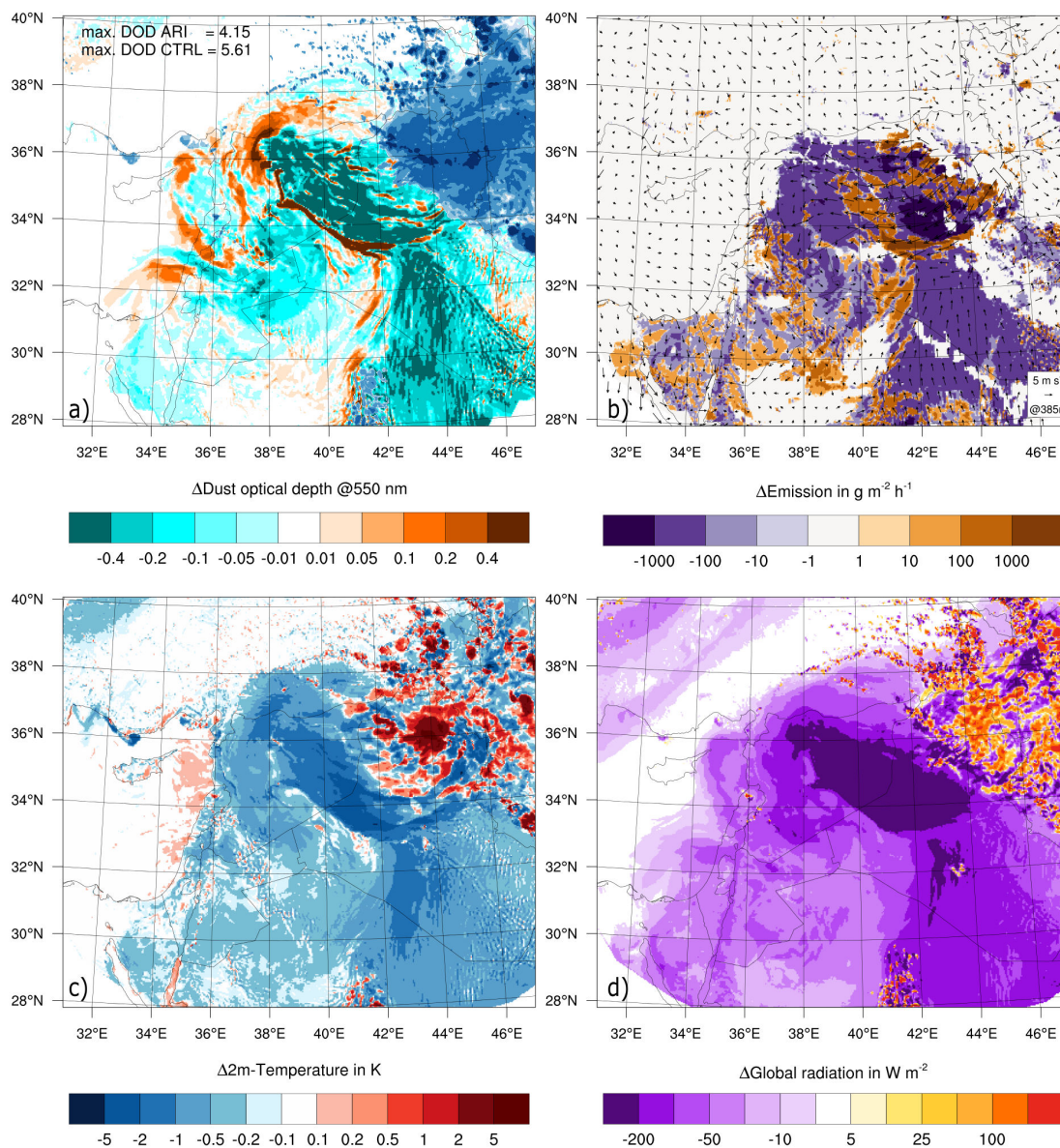


Figure 5.14: ICON-ART model results at 10 UTC 07 September, same as figure 5.13.

In figure 5.14 the daytime radiative effect of mineral dust is apparent. The dominant effect is the reduction in incoming shortwave solar radiation, while the increase in down-welling atmospheric long-wave radiation is of lesser magnitude (not shown). Resulting reductions in net global radiation are more than 200 W m^{-2} in the CPO3 region. The average value at the core of CPO3 in the region bordered by the 34° , 36°N circles of latitude and 40° , 42°E meridians is -281 W m^{-2} (fig.

5.14 d)). The reduction in incoming energy leads to a widespread reduction in 2m-temperature of more than 2 K. The average value in the aforementioned area is -1.4 K. The reduction in surface temperature is less than documented by other studies (see section 2.2.2). Possible explanations are the less absorptive character of mineral dust in ICON-ART with low values of the imaginary part of the refractive index in the short-wave region (see section 4.3.2). Consequently, the dust mostly scatters radiation compared to absorbing it, thereby converting direct radiation to diffuse radiation. As the energy reaches the surface nevertheless, reductions in surface temperature due to mineral dust are smaller than those found by other studies. A detailed analysis for the 10 UTC situation supports this hypothesis. Decreases in direct shortwave radiation are on the order of 600 W m^{-2} inside the CPO3 region. However, these are countered by increases in diffuse shortwave above 200 W m^{-2} , giving a net reduction in short-wave radiation of approximately 400 W m^{-2} (not shown). Furthermore, the high amount of water vapour contained in the CPOs possibly absorbs and scatters large quantities of solar radiation without dust already, thereby reducing the effect due to mineral dust. An observation which supports this hypothesis is that the reduction in 2m-temperature does not scale linearly with the difference in DOD between inflow and outflow region of the MCS.

The reductions in surface temperature have a stabilizing effect on the boundary layer (see also section 2.2.2). As a result of the increased boundary layer stable stratification dust emissions decrease almost homogeneously throughout the dust affected region (fig. 5.14 b)). In addition, this results in a reduced maximum DOD of 4.15 in ARI compared to 5.61 in CTRL for the whole domain. During the late afternoon with maximum boundary layer development this difference increases. At 15 UTC ARI and CTRL show maximum DODs of 6.11 compared to 9.26, respectively. Another marked feature visible in figure 5.14 is the previously discussed difference in DOD at the CPO leading edges (fig. 5.14 a)). As the feature is visible over more than 20 hours and in connection with all CPOs this confirms the observation of faster spreading CPOs in simulations including the mineral dust radiative feedback as proposed earlier. The streaks detectable inside the CPO3, where ARI shows higher values of DOD, can be attributed to shallow boundary layer convection which develops earlier and more intensely in the CPO3 region in CTRL due to the lacking vertical stabilization (not shown). Consequently, due to the redistribution of dust by convection the DOD field is more inhomogeneous in the CTRL run (not shown).

5.3.3 Mineral dust radiative effect on atmospheric stratification

So far, only the horizontal 2D-effects of the mineral dust radiation interaction were analysed. However, the vertical redistribution of the radiative energy absorbed by mineral dust is also of importance due to its influence on vertical stability of the atmosphere. The comparison of modelled vertical dust distribution shows good agreement with CALIPSO satellite data, therefore vertical cross-sections can be used to investigate the mineral dust radiative effect. The analysis is done at four points in time along two cross-sections. The points in time chosen are 03 UTC and 10 UTC 07 September, as well as 03 UTC and 11 UTC 08 September.

The first cross-section runs along 35°N latitude, providing a transect of the most interesting fea-

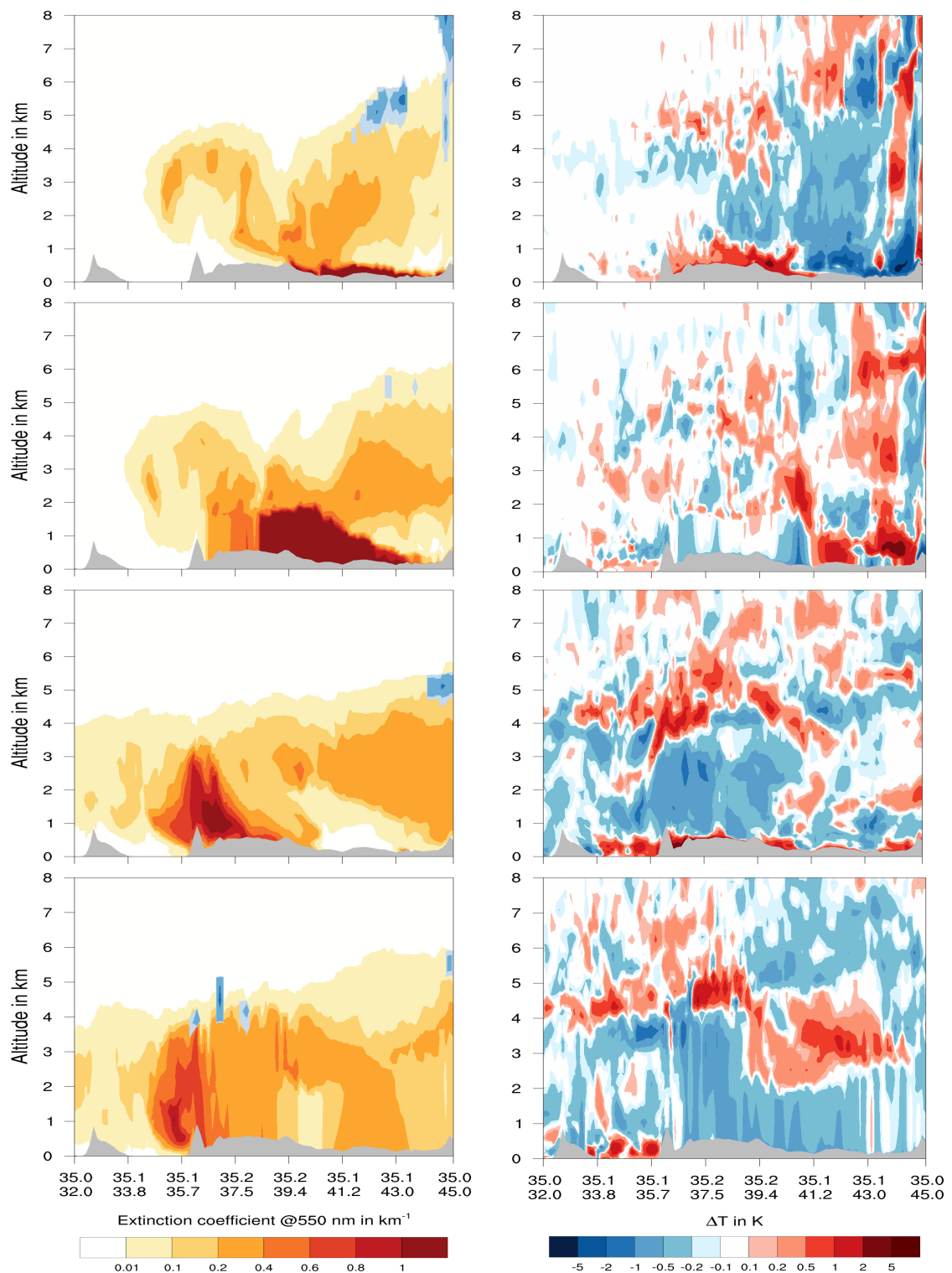


Figure 5.15: ICON-ART model results along a vertical cross-section from 35°N , 32°E to 35°N , 45°E . Shown on the left side is the extinction coefficient from the ARI run. On the right side the temperature difference from ARI-CTRL is displayed. Times shown are from top to bottom 07 September, 03 UTC, 10 UTC; and 08 September, 03 UTC, 11 UTC.

tures (fig. 5.15). At 03 UTC 07 September the CPO3 is still confined to a very shallow layer with high extinction coefficients. Its leading edge is at approximately 40.5°E but difficult to detect due to the low dust emissions before sunrise. The temperature difference between ARI and CTRL is noisy in the upper part and the MCS region. Nevertheless, the generally colder airmass of CPO3 in ARI is identifiable and reaches down to the surface, masking the normal night-time surface warming effect of mineral dust as previously discussed. Towards the west the elevated dust plume from CPO1 and the Heat Low is apparent. It is located at altitudes between 2 – 5 km due to the penetrating sea breeze which causes lifting (see also section 5.2.2). In this region the expected night-time effect of mineral dust is simulated. Due to the elevated dust plume the boundary layer warming extends to a greater height of approximately 1 km. Noticeably, the majority of the boundary layer affected by the dust plume is colder in ARI above the shallow warmed night-time layer. This is due to the previous daytime cooling of the full boundary layer, the effect of which is dragged on into the night (not shown). At 10 UTC the CPO3 has spread further towards west and its vertical depth has increased as discussed in section 5.2.3. Again the temperature signal of the mineral dust radiative effect is noisy in the MCS region towards the east. A cooling is visible in the main dust region towards west. However, it does not extend throughout the full dust layer height as usual. The reasons for the confinement to the surface could be dynamic flow differences in connection with the fast spreading CPO3 in the ARI run. At 03 UTC 08 September a shallow night-time warming of effect mineral dust is simulated by ICON-ART. The surface cooling over Cyprus is again caused by changes in large scale circulation patterns, which superpose the expected mineral dust signal. At 11 UTC 08 September the mineral dust radiative effect on vertical temperature distribution is very clear. The full boundary layer height containing mineral dust is cooled due to reduced incident solar radiation. The magnitude of cooling increases towards the surface. At the top, where a part of the solar radiation is absorbed, heating due to mineral dust is apparent. A shallow exception is noticeable over the EM sea as the thermal inertia of the sea surface is higher and local circulation systems are changed due to mineral dust in this region. The reduction of sea breeze intensity due to the reduced heating of the land surface leads to reduced ventilation of the Mediterranean Sea. Consequently, less heat is transported towards the land and the surface temperature above sea increases. The onset of this phenomena is also detectable in the temperature difference field of figure 5.14.

The second cross-section runs from 32°N , 34°E to 34°N , 38°E . It thereby crosses from the EM across the Dead Sea Rift Valley through the Golan Heights into Syria (see fig. 5.18 for a map of the location). It provides insight into the arrival of the dust front in Israel and its interaction with the topography of the Dead Sea Rift Valley (fig. 5.16).

At 03 UTC 07 September the pre-flooding with dust due to CPO1 in combination with the Heat Low is simulated by ICON-ART, creating the expected temperature increase below the dust plume. Inside the plume, again as a remainder of the day, cooler temperatures are simulated for the ARI run. At 10 UTC the advancing frontal structure connected to the CPO2 is situated at 37°E longitude. The difference in vertical structure compared to the aged dust plume with a maximum above Israel is evident. The dust plume located in the EM is located at an altitude above 1 km, whereas the CPO2 structure shows its maximum near the surface. Consequently

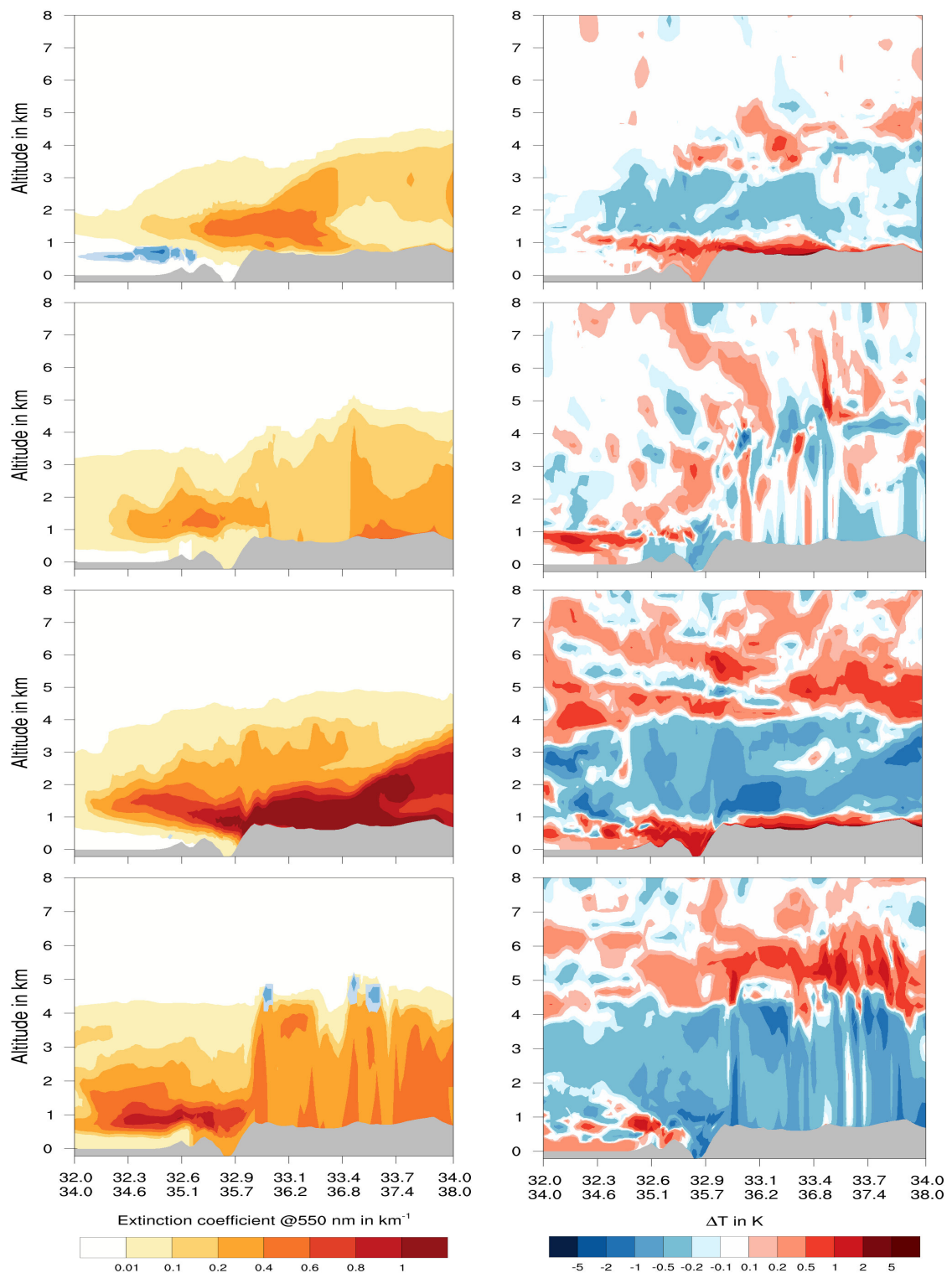


Figure 5.16: ICON-ART model results along a vertical cross-section from 32°N , 34°E to 34°N , 38°E . Shown on the left side is the extinction coefficient from the ARI run. On the right side the temperature difference from ARI-CTRL is displayed. Times shown are from top to bottom 03 and 10 UTC 07 September; 03 UTC and 11 UTC 08 September.

the radiative effects of the two different dust plume stages are also different. The former causes heating below due to the aforementioned change in Mediterranean sea breeze circulation, whereas the latter causes cooling in the boundary layer down to the ground. At 03 UTC on 08 September the arriving, dust loaded CPO3 is simulated as just crossing the Dead Sea Rift Valley. Due to the magnitude of the arriving dust concentrations a very strong near surface warming is simulated. A noticeable, interesting feature which is explained in section 5.4, is the wave-like structure in the extinction coefficient at the eastern side of the Dead Sea Rift Valley. In this region the night-time warming effect of mineral dust in a shallow surface layer is broken. At 11 UTC a difference between the region east and west of the Dead Sea Rift Valley is apparent. To the east, the dust is mixed throughout the full boundary layer, whereas towards the west the main dust plume is confined to a thinner layer with a maximum at 1 km altitude. Again, the difference in temperature signal between east and west of the Dead Sea Rift Valley is discernible. The previously discussed warmer layer at low levels above the EM due to modified circulation systems is simulated once more. Apart from this difference in temperature signal the mineral dust radiative feedback is again very clear.

5.3.4 Influence of the varying mineral dust median diameter

The new parametrization implemented in ICON-ART is able to account for changes in median diameter of the modes during transport through calculating size dependent optical properties (see section 4.3.3). The effect of this new parametrization on radiative transfer is investigated with the help of figure 5.17.

In order to understand the changes later on, we have to first know the initial state. The top row shows the overall DOD at 03 UTC 07 September for a run with varying median diameter optical properties. In a post processing step the contribution of the individual modes to the DOD was calculated. Mode A makes the biggest contribution, even though its dust column mass is smallest, as is apparent from the panels showing column integrated dust mass in the second row. Mode B and C make much smaller contributions to the DOD even though their individual dust column mass is greater. The observed contribution of the individual modes is conclusive as the extinction coefficient of mode A is much higher than for Modes B and C.

The third row shows the difference in DOD at 03 UTC 07 September between a run with varying median diameter optical properties and constant median diameter optical properties. The left panel shows a widespread increase in DOD as the overall result. Again, a post-processing calculation of the DODs for the individual modes allows for attribution of this increase in DOD to mode B and C. Mode A even shows a slight decrease in DOD. The same behaviour can be detected for the long-wave part of the spectrum (not shown). The main contribution of mode B and C goes hand in hand with the observation that the column weighted and normalized median diameter (calculated according to equation 3.15) of these two modes changes greatly during transport. As is shown in the last panel row, mode A does not show a decrease of the median diameter during transport. This explains the absence of an effect of the new parametrization for this mode.

Summarizing, the changes in optical properties with a varying median diameter are largest for

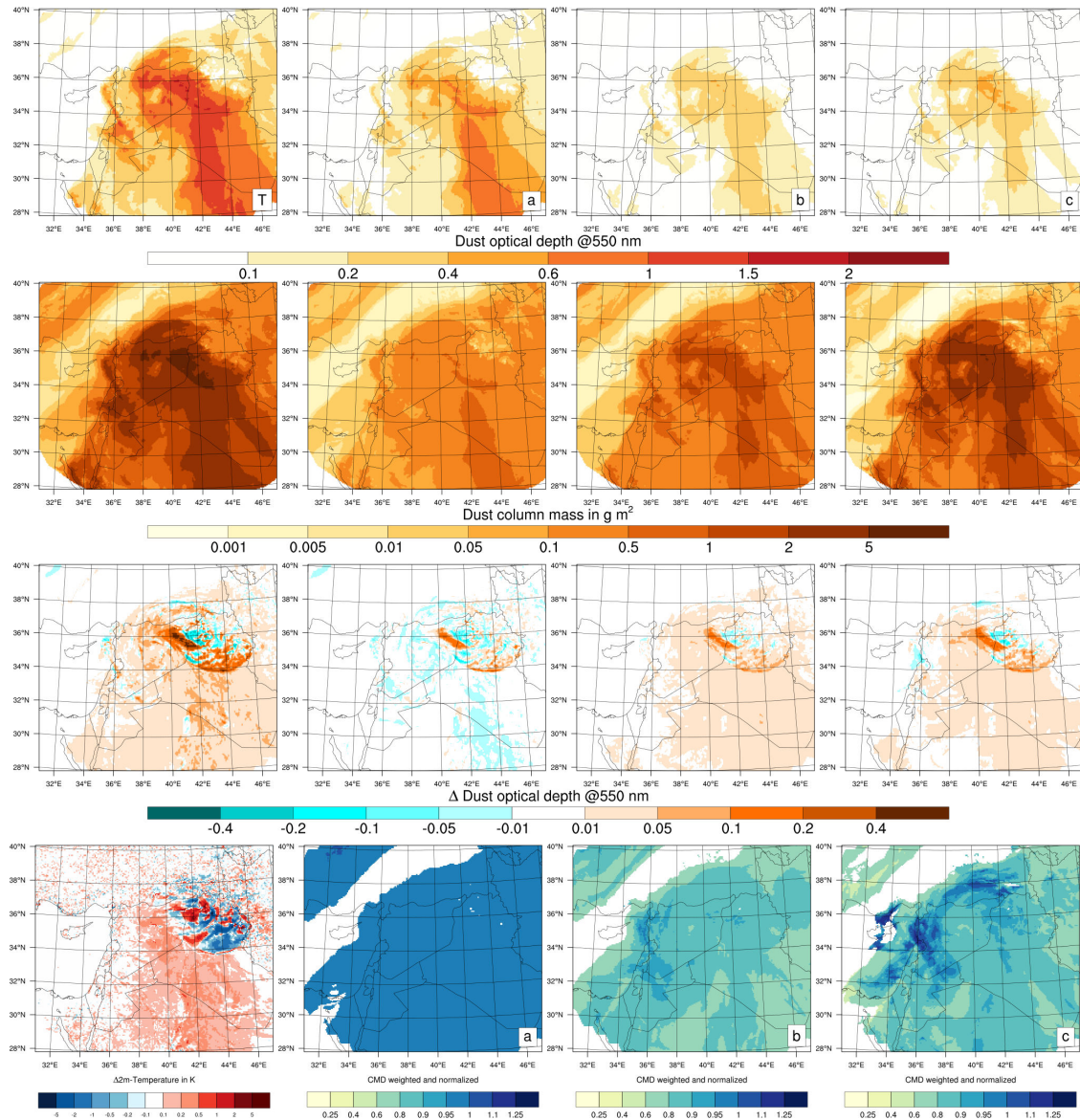


Figure 5.17: ICON-ART model results with post-processing applied for 03 UTC 07 September. Left column displays combined values for all modes. Displayed in the 2nd, 3rd and 4th column are the contributions by mode A, B and C respectively. Visible are from top to bottom: 1. Dust optical depth at 550 nm. 2. Dust column mass in g m^{-2} 3. Difference in dust optical depth due to varying median diameter at 550 nm calculated from post-processing. 4. Left: Influence of varying median diameter on 2m-surface temperature. Right: Column weighted and normalized median diameter.

mode A (see section 4.3.3). Yet, due to the constant median diameter during transport the new parametrization does not show a change in aerosol optical depth for mode A. However, for mode B and C a clear increase in optical depth is calculated due to the new parametrization. Even though the dependence of the optical properties on the median diameter is small for these modes, the great column mass of each mode combined with a big change in median diameter create a noticeable effect.

The bottom left panel shows the temperature difference at 03 UTC 07 September between a run with varying median diameter optical properties and constant median diameter optical properties. The dominant signal is a slightly warmer surface temperature on the order of 0.2 K caused by the varying median diameter. The increase in surface temperature is linked to the increase in DOD. The same signal and magnitude is found in the dust source region of a second simulated dust event which caused dust transport from the Sahara towards Europe (not shown). In both cases, a discernible signal is only observed in the dust source region during night-time. For the event simulated in this study, consideration of the change in median diameter again causes an intensification of CPO3. This further supports the previously made assumption that the surface temperature of the inflow region is of crucial importance to the intensity and structure of the MCS and thereby also its CPO.

5.4 Long-range transport to Israel

In this section, the dust transport towards the southern EM in general and towards Israel in particular is discussed. The dust transport in this region is not simulated with the correct magnitude by ICON-ART (see section 5.2.4) and the availability of surface based measurements in this region provides insight into the reasons.

5.4.1 Hydraulic jump upstream the Dead Sea Rift Valley

As is visible in figure 5.16, the arrival of the dust plume is simulated above a height of 1 km in Israel. This is in good agreement with measurements of the dust plume height in Israel which also report an arrival of the dust plume in 1 km height (Alpert et al., 2016).

The previously mentioned wave structure in the extinction coefficient on the lee side of the Golan Heights needs further investigation as it greatly influences the structure of the mineral dust transport (section 5.3.3). The dust is transported in a shallow layer with approximately 1 km thickness towards the Jordan Valley. In the region of the wave structure, after passing the Golan Heights crest, the vertical depth of the dust plume decreases significantly to a few hundred meters. The plume expands and returns to its original height again in an abrupt expansion further to the west. The reason for this behaviour is the existence of a flow phenomena termed 'hydraulic jump' in the region, more insight is provided in the following paragraphs.

In figure 5.18 the usual analysis of the flow conditions in the region as simulated by ICON-ART is provided. Clearly distinguishable is a sharp gradient in wind speed along the down-slope lee side of the Golan Heights with a maximum upstream. The line structure extends further south-east

across Jordan to the border of Saudi-Arabia (dashed line in fig. 5.18). It is always located on the down-slope, lee side of the terrain. An analysis at consecutive time steps shows that it is existent for more than 6 hours and quasi-stationary or even slightly retrograde, with a maximum intensity at 00 UTC. It is thereby clearly connected to the arrival of the aged CPO3 in the region. In figure 5.19 a cross-section of ICON-ART results along the black line in figure 5.18 is displayed. With the help of this data the wave structure in the extinction coefficient and the related sharp gradient in the wind field can be identified as being caused by a hydraulic jump.

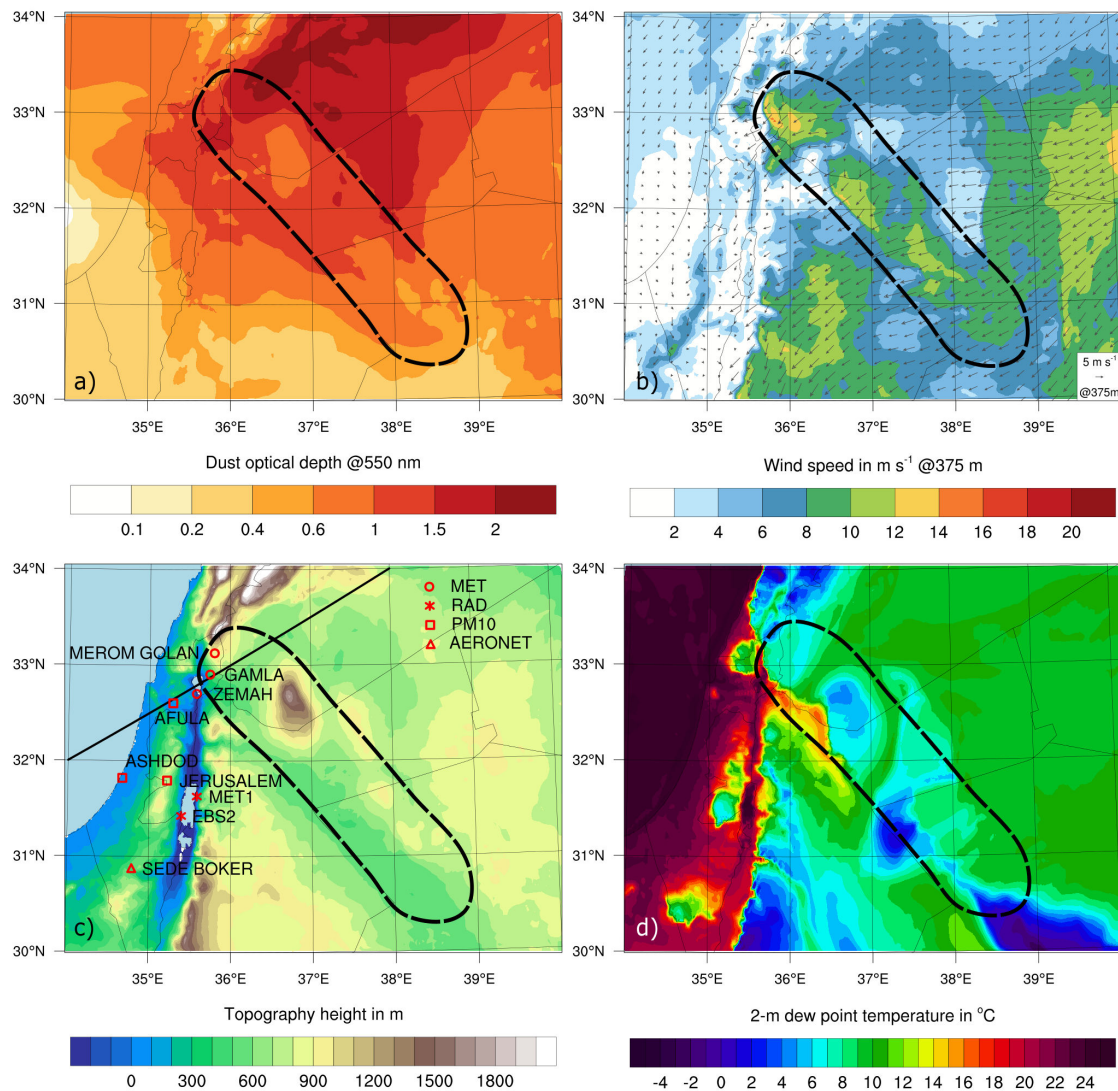


Figure 5.18: ICON-ART model results at 03 UTC 08 September, same as figure 5.3. An exception is the bottom left plot which shows the orography in the region colour-coded. Dashed black line marks region of hydraulic jump occurrence. Solid black line in c) shows location of ICON-ART vertical transect displayed in figure 5.16 and 5.19. In addition, location and names of stations used for comparison of results are displayed.

Hydraulic jumps are connected to flows going from a sub-critical flow stage with Froude numbers Fr smaller one, to a super-critical flow stage, with Froude numbers greater one. According to

Drobinski et al. (2001) the Froude number can be calculated as:

$$Fr = \frac{U}{\sqrt{gh}} \cdot \sqrt{\frac{\Theta_v}{\Delta\Theta_v}}. \quad (5.1)$$

Thereby, U denotes the wind speed and Θ_v the virtual potential temperature in the atmospheric boundary layer, chosen at a representative level and $\Delta\Theta_v$ the temperature inversion at the boundary layer top. Further, g is the gravitational acceleration and h the atmospheric boundary layer height. The formula provides insight into the generating mechanisms for super-critical flow stages with Froude numbers greater one. The emergence of the super-critical flow is connected to a sharp decrease of the mixing layer height, usually due to upper level atmospheric subsidence and/or onset of the night. A simultaneous rise of the terrain leads to a strong compression of the flow which consequently transforms into the supercritical stage. As the super-critical flow cannot exist for a long distance, the flow eventually reverts to a sub-critical stage again. At this stage the hydraulic jump occurs. Hydraulic jumps are connected to very high wind speeds at the surface due to the super-critical flow conditions upstream. In the lee of the jump great turbulence intensity is observed.

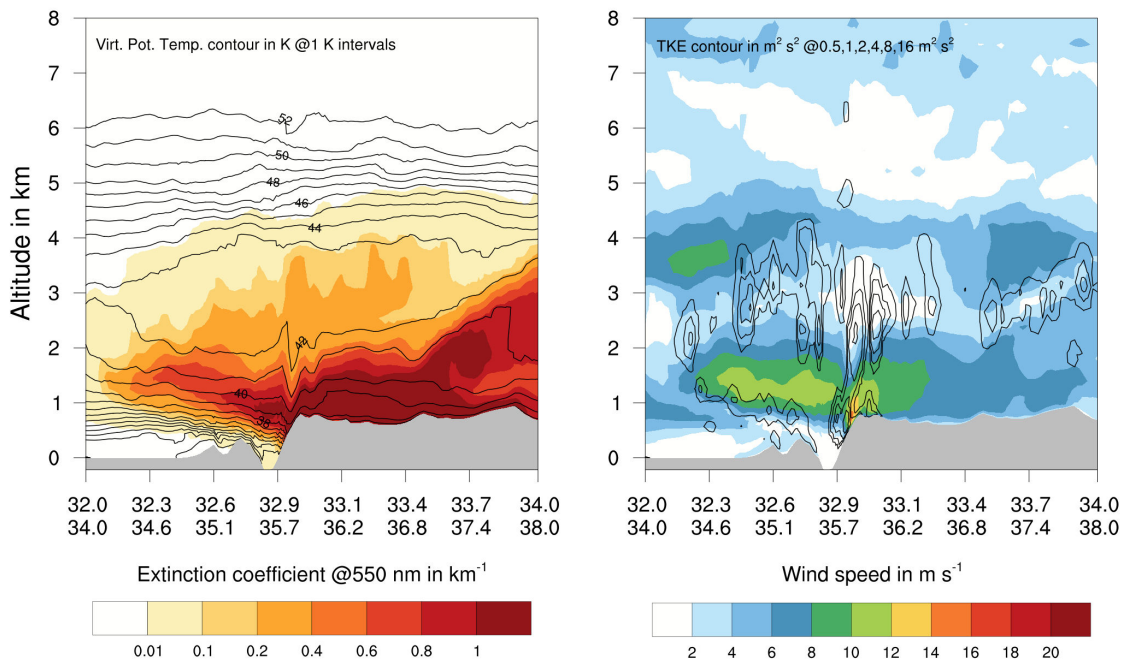


Figure 5.19: ICON-ART model results along a vertical cross-section from 32°N, 34°E to 34°N, 38°E at 03 UTC 08 September. Displayed on the left side is the colour-coded extinction coefficient overlain with virtual potential temperature contours. On the right side wind-speed is colour coded and overlain with turbulent kinetic energy contours.

Hydraulic jumps have been documented penetrating the Dead Sea Valley for flow conditions from the west (Metzger, 2016). The flow across the Golan Heights shows characteristic features of a super-critical flow with a subsequent hydraulic jump (see figure 5.19). These are:

1. A continuous decrease in mixing layer height detectable in the virtual potential temperature

- and extinction coefficient fields leading to a compressions of the sub-critical flow from east to west.
2. A sharp decrease in the vertical flow depth, connected to a rise in flow speed, after passing the orographic Golan Heights crest. This denotes the transformation of the flow state from sub- to super-critical.
 3. A subsequent sudden increase in flow depth when the flow state reverts to the sub-critical stage again inside the Dead Sea Rift Valley. This is accompanied by a sharp decrease in flow speed and connected to an increase in atmospheric turbulence.

An approximate calculation of the Froude number upstream and downstream the Golan Heights crest height with average flow conditions as simulated by ICON-ART confirms the conversion of the flow state:

$$Fr_{upstream} = \frac{8 \text{ m s}^{-1}}{\sqrt{9.81 \text{ m s}^{-2} \cdot 1200 \text{ m}}} \cdot \sqrt{\frac{312 \text{ K}}{2 \text{ K}}} = 0.92,$$

$$Fr_{downstream} = \frac{12 \text{ m s}^{-1}}{\sqrt{9.81 \text{ m s}^{-2} \cdot 800 \text{ m}}} \cdot \sqrt{\frac{313 \text{ K}}{2 \text{ K}}} = 1.70.$$

Hydraulic jumps have been investigated and suggested as dust generating mechanisms (Cuesta et al., 2009). Their existence and interaction with the orography under strong easterly flow conditions has been proven for the Sahara (Drobinski et al., 2009). As the gust front of CPO3 reaches the Dead Sea Rift Valley almost along its full length, the flow reaches supercritical stage in the vicinity of many prominent orographic features. Consequently, the widespread existence of hydraulic jumps in connection with the upstream super-critical flow is assumed to be responsible for enormous dust emissions on the eastern side of the Dead Sea Rift Valley. Dust emission in the region is assisted by the timing of the event, as in September the soil in the region is most erodible due to the preceding hot and dry summer. Summarizing the above discussion, the supercritical flow with high wind speeds in the lee of orographic obstacles can lead to widespread and strong dust emissions on the eastern side of the Dead Sea Rift Valley, which explains the exceptional amount of dust in the southern part of the EM.

Modelling of the hydraulic jump and related dust emissions is very difficult due to four reasons. First of all, the timing of the arrival of the gust front has to be correct in order to allow for the flow to convert to the supercritical stage in its interaction with boundary layer dynamics at night. Second, the orography in the model has to be detailed enough in order to represent the highest orographic features causing the conversion of the flow. Third, the near-surface conditions in the nocturnal boundary layer have to be modelled correctly in order to capture the high surface wind-speeds responsible for dust emissions. Fourth and last, in order to allow for dust emission due to the super-critical flow and hydraulic jump the soil data has to be highly resolved in order to employ the correct soil type in the region with the highest wind speeds. In addition, the state of the soil with respect to water content has to be initialized correctly. Each of the above listed problems poses a great challenge on its own, highlighting the difficulty to model the connection and interaction of all four correctly.

The existence of hydraulic jumps in ICON-ART is detectable along many cross-sections and at different times in the region. Some of them occur on the lee-side of much less pronounced orographic features such as the mountain structure visible at 32.5°N , 37.0°E in figure 5.19. Although ICON-ART simulates hydraulic jumps in the region they need to be validated in order to evaluate the simulation quality. The hydraulic jump investigated above allows for comparison with observations in the next section.

5.4.2 Comparison to surface observations

An interesting observation in the ICON-ART model results is, that the lowest circulation system in the Dead Sea remains decoupled from the dust plume, despite the super-critical flow penetrating into the valley (see figure 5.19). To what extent the simulated super-critical flow structure is confirmed by measurements in the valley is discussed in the next section. Afterwards, a validation of the simulated dust concentrations and dust transport processes over Israel is conducted with the help of three characteristic PM10 station measurements. At last, simulated values of DOD are compared to values retrieved by an AERONET station in Sede Boker.

Meteorological station measurements

The validation is done with the help of three meteorological stations approximately along the ICON-ART cross-section through the Golan Heights. The location and names of the stations used is marked in figure 5.18, for a description of the station characteristics see section 3.3. Unfortunately, no measurements are available in Jordan, where the existence of the hydraulic jumps is detectable in many places in ICON-ART and where the more erodible state of the soil is assumed to be responsible for high dust emissions.

The measurements of the meteorological stations are displayed together with the ICON-ART model results for their location in figure 5.20. The arrival of the main dust plume is simulated by ICON-ART past 18 UTC on 07 September. Subsequently, DOD values above 1.5 are reached during the night.

The development of the super-critical flow regime penetrating the Dead Sea Rift Valley is observed at two meteorological stations. It is detectable by marked, high wind speeds, a change in wind direction towards east and a sudden increase in temperature by approximately 4°C . The higher Merom station is first affected shortly before 18 UTC, whereas the lower Gamla station experiences high wind speeds only from 20 UTC onwards. Interestingly, confirming the super-critical flow theory, the highest values of wind speed are measured in Gamla around midnight. This is because the flow has more potential for gravitational acceleration down to 405 m compared to 950 m. Zemah, the station at the floor of the Dead Sea Rift Valley does neither report high wind speeds nor a change in wind direction at any point during the night. This confirms the ICON-ART simulation of the super-critical flow not reaching the valley bottom.

However, an investigation of the ICON-ART model results for wind speed and direction shows that the intensity and extent of the super-critical flow regime is not captured correctly near the surface. Although model results for Merom show an increase in wind speed and change in wind

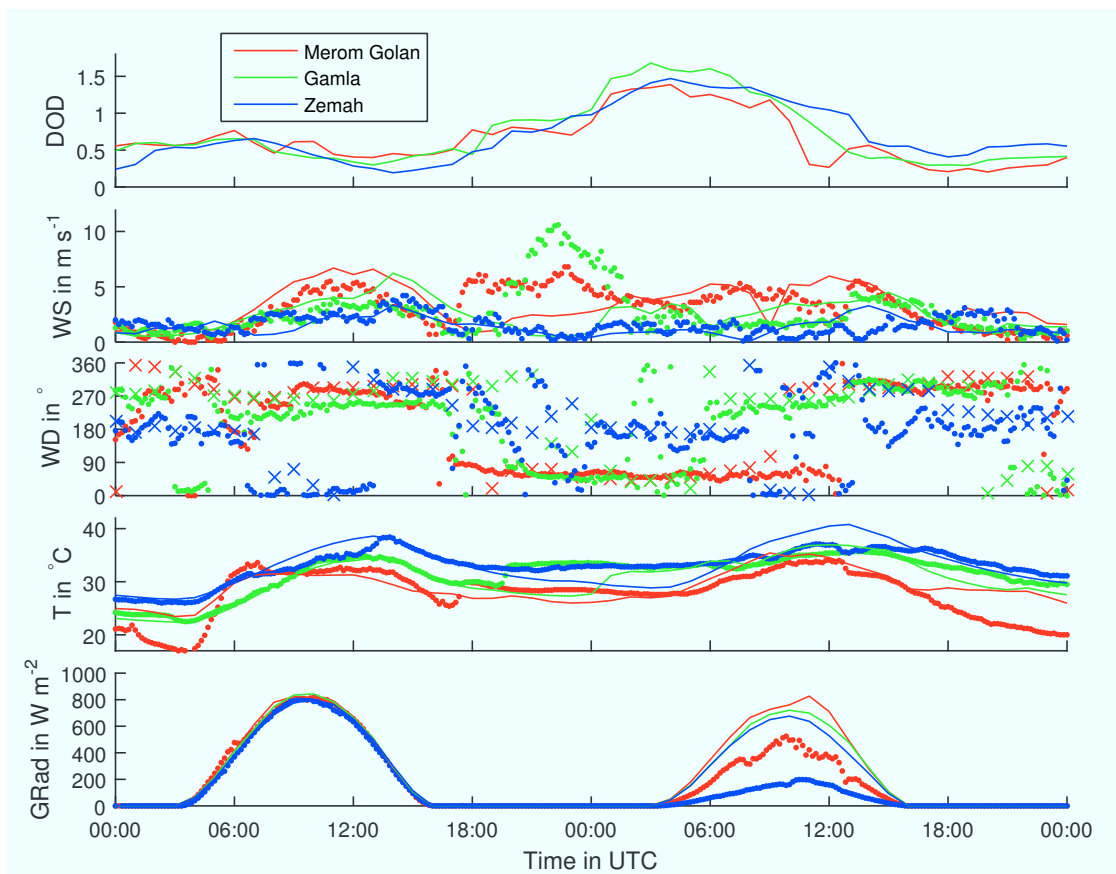


Figure 5.20: Observations and model results for three stations in the Golan Heights for 07 and 08 September. Points denote observations and solid lines/crosses model results. Shown are from top to bottom: 1. Modelled dust optical depth 2. Wind speed (WS). 3. Wind direction (WD). 4. 2m-surface temperature. 5. Global radiation (GRad).

direction the results are far from the observed intensity. For the lower Gamla station ICON-ART models the arrival of the super-critical flow with a delay of six hours and only a third of the observed intensity. As in the observations, the arrival is detectable in changes of wind speed, direction and surface temperature. The Zemah station and valley floor remains unaffected in ICON-ART as in reality. The possible reasons for the deviation of the simulation from reality include an unrealistic night-time boundary layer regime, incorrect atmospheric conditions upstream of the valley and a delayed arrival of the CPO3. As a result, possible mineral dust emissions due to the super-critical flow cannot be captured by ICON-ART. Through its destabilizing night-time boundary layer effect mineral dust itself can provide a positive feedback mechanism to higher near surface wind speeds and again higher dust emissions in the super-critical flow region. Thereby the amount of dust transported into the region is assumed to be of crucial importance.

The global radiation observations for 08 September show higher values for Merom Golan compared to Zemah. No observations of this quantity are available for Gamla. As Merom Golan is situated higher than Zemah the measurements appear realistic and the behaviour is also modelled

by ICON-ART with a reduction for lower stations due to the greater amount of dust column mass above. In addition, the measurements provide a first clue on the amount of dust contained within the lowest 1.2 km, which is the altitude difference between the stations (if a homogeneous distribution of dust is assumed in the region). ICON-ART does not model the correct magnitude of reduction in global radiation. Modelled between day reductions in maximum global radiation for Zemah are 125 W m^{-2} , whereas in reality 611 W m^{-2} were observed.

Environmental station data

In this section the simulated dust concentrations are compared to measurements from three stations in Israel. The selected stations are Afula, Jerusalem (Bar Ilan) and Ashdod (Nir Galim) as they all show individual dust concentration characteristics during the event (see figure 5.18 for a map of the station locations).

The first row in figure 5.21 shows the course of the DOD connected to the arrival of the dust plume in Israel. The dust plume reaches Afula first, this is also where the highest values of DOD up to 1.5 are achieved because of the previously discussed transport through the Golan Heights. A few hours later Jerusalem shows an increase and its peak optical depth. DOD increases even later in Ashdod due to its location in the south-west, but the DOD values reach higher levels than in Jerusalem due to the lower altitude of the station.

In the second row PM10 concentrations as measured by the environmental stations are displayed and in the third row PM10 concentrations as modelled by ICON-ART. Please note the difference in y-axis scaling by a factor of ten. The tremendous difference in absolute values of PM10 concentrations is most likely caused by the inadequately modelled interaction of the dust plume with the complex orography of the Dead Sea Rift Valley. The lack of a sufficiently developed super-critical flow and resulting high near-surface wind speeds in the model prevent dust emission in Jordan. However, as is shown in section 5.4.2, the associated processes are assumed to be the reason for the extraordinarily high dust concentrations observed in Israel and the southern EM.

Despite the large difference in absolute values, the dust transport processes can be studied by comparing the course of the measured and modelled PM10 concentrations. Although the DOD in Afula reaches highest values during the night already, peak concentrations at 57 m surface elevation are only measured after noon on 08 September. This is due to arrival of the dust plume in 1 km height. Consequently, the onset of turbulent mixing is needed to transport the high dust concentrations towards the surface (see also figure 5.16). The discussed processes are modelled sufficiently by ICON-ART, as it shows a very similar shape of the PM10 concentrations curve compared to the measurements with a peak at 12 UTC.

Highest overall PM10 concentrations are measured by the Jerusalem station. It shows the earliest and most pronounced peak of all stations at 08 UTC. This is also the case in ICON-ART, although with a shorter peak duration. The earlier and higher peak concentrations in Jerusalem are due to the elevated location of the measurement station at 770 m which is almost inside the dust plume. For this reason, PM10 concentrations are also more correlated with the shape of the DOD curve at this station. A secondary peak after sunset is visible in the measurements and model results.

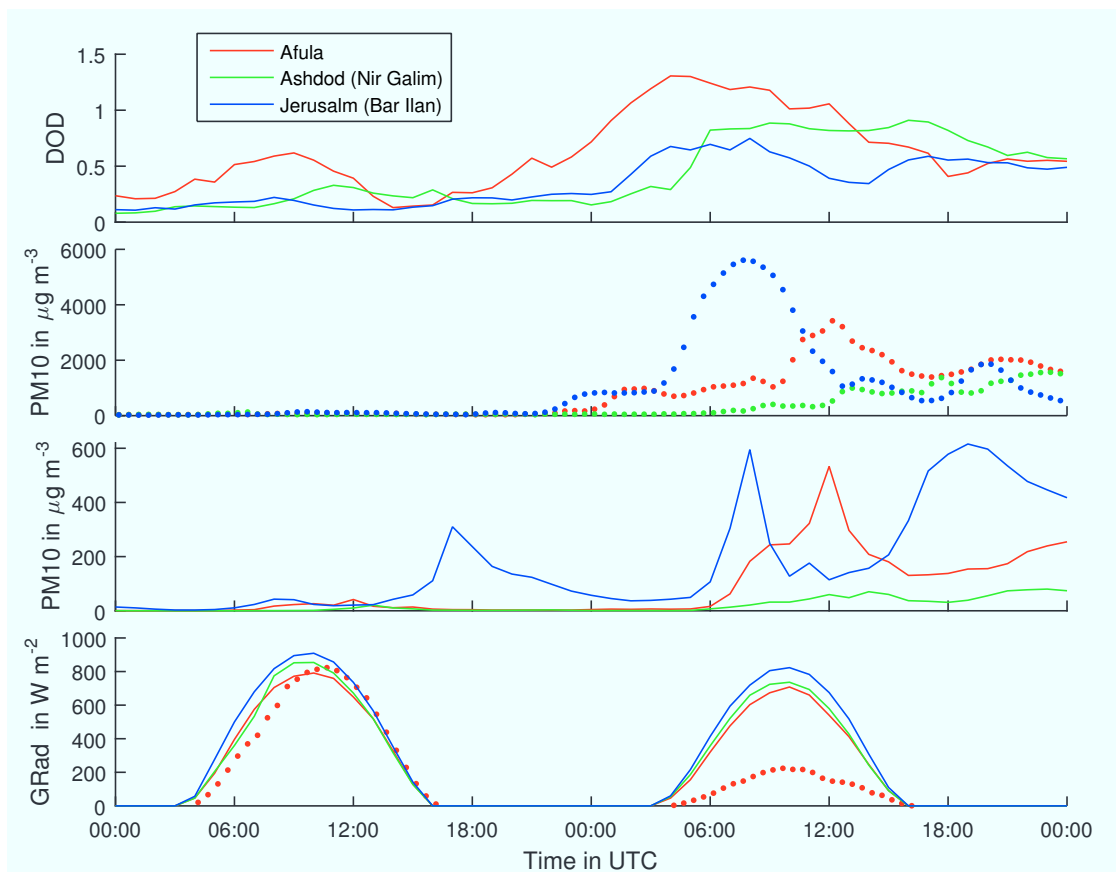


Figure 5.21: Observations and model results for three stations in Israel for 07 and 08 September. Points denote observations and solid lines model results. Please note the difference in y-axis scaling by a factor of ten between the second and third sub-plot. Shown are from top to bottom: 1. Modelled dust optical depth. 2. Measured PM10 concentrations. 3. Modelled PM10 concentrations. 4. Global radiation (GRad).

This peak can be explained by the formation of a stable nocturnal boundary layer, in which the dust from higher altitudes settles to the ground.

The station in Ashdod measures the lowest PM10 concentrations at nearly all times, despite showing the highest values of modelled DOD above past noon. This is due to the early onset of the Mediterranean Sea breeze at the shore which brings in cleaner air compared to the other stations. The reason for the cleaner nature is the less turbulent character of the marine boundary layer compared to the boundary layer over land. Consequently, it mixes less dust to the surface, a feature which is captured well by ICON-ART.

The radiation is only measured at Afula, as before ICON-ART fails to reproduce the measured low values of global radiation as for the radiative impact the absolute values of the dust concentration are of importance. The differences visible in the DOD above the stations again manifest themselves in differences between the modelled amount of global radiation at the stations.

Future improvements of the simulations should result in an increased mineral dust transport into the region in ICON-ART. Thereby, its influence on local circulation systems is expected to be

modelled more accurately. Consequently, the already well modelled individual station characteristics are expected to improve further. This should also yield improvements for the magnitude of the individual peaks in relation to each other.

Comparison to AERONET data

The AERONET data for Sede Boker is displayed in figure 5.22, together with the modelled DOD from ICON-ART. The model is not able to reproduce the absolute values of the aerosol optical depth measured by the sun photometer, which are in the order of four. As with the PM10 measurements a difference of almost a factor of ten exists between the results for 08 September. The measurements seem realistic as they are in fair agreement with MODIS AOD observations and measurements from other AERONET stations in Israel (Weizmann Institute, Eilat). The additional AERONET measurements are available only for 09 September and consistently show aerosol optical depths of the same order.

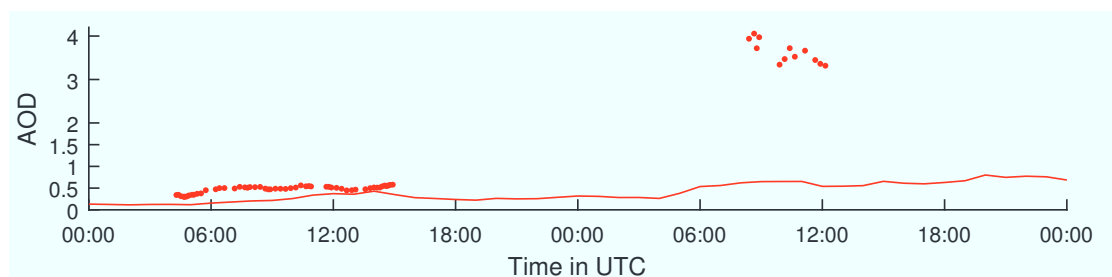


Figure 5.22: Points show Sede Boker AERONET aerosol optical depth measurements at 500 nm for 07 and 08 September. The solid lines shows the simulated ICON-ART dust optical depth at 550 nm.

Summarizing, the differences discussed here again highlight the difficulties in correctly modelling the intense dust transport towards the southern EM. The main reason for the failure of ICON-ART to capture the dust transport into this region with the correct magnitude is the interaction of the CPO flow with orographic features. The generation of super-critical flow regimes with subsequent hydraulic jumps is simulated by ICON-ART, however not with the correct magnitude and timing. Consequently, the associated dust emissions processes cannot be captured by ART, resulting in too low dust concentrations in the region. Nevertheless, the main dust transport characteristics are simulated correctly as is shown by the comparison to PM10 station data.

6. Conclusions

The aim of this work is to investigate an exceptional dust event which occurred in the Eastern Mediterranean in early September 2015, including the radiative effect of mineral dust. In order to achieve this goal, the mineral dust radiation interaction has been implemented as a new module in ICON-ART. Based on Mie scattering calculations, which are conducted off-line to calculate the mineral dust optical properties, the radiative transfer parameters used by ICON are calculated on-line in ART to account for the mineral dust radiative effect. A new, size dependent parametrization of the mineral dust optical properties is proposed. The study presents the first simulation of the severe dust event with a convection permitting resolution. In addition, it includes the radiative effect of mineral dust. A comparison of the results with MODIS VIS, MODIS AOD, EUMETSAT RGB dust product and CALIPSO satellite observations as well as meteorological, PM10-environmental and AERONET measurements in Israel reveals the quality of the ICON-ART simulations with respect to the structure and timing of the dust transport. The influence of the synoptic situation, the driving atmospheric systems and the mineral dust radiative effect on the event are analysed in-depth.

Is the forecast of the dust event improved by running convection permitting simulations?

The convection permitting simulation of the dust event with ICON-ART improves the forecast quality decisively. The results allow for an in-depth investigation of the synoptic situation and the atmospheric drivers responsible for dust emission. The convection permitting simulations enable a realistic development of organized meso-scale convection and the connected flow structures responsible for dust emission. The driving meteorological systems and resulting dust emissions are captured in their horizontal, vertical and temporal structure as is shown by the comparison with satellite observations. The simulated DOD over Syria and Iraq is of realistic magnitude with values above 2 throughout the main dust event region and maximum values above 6. The transport to the northern part of the EM and Cyprus is modelled with DOD values above 2 and in good spatial agreement with satellite observations. The DOD in this region is less than observed, but one order of magnitude better than other state-of-the-art models, at a longer forecast time and without data assimilation. For the transport to the southern EM, a hydraulic jump is demonstrated to be of crucial importance. It is captured by ICON-ART, albeit with reduced intensity compared to observations. Consequently dust transport into the region is underestimated in the order of

one magnitude, with DODs in the range of 0.5 – 1.5 over Israel and PM10 concentrations up to $600 \mu\text{g m}^{-3}$ in Jerusalem. Nevertheless, the characteristic dust transport features are captured. The arrival of the main dust plume during the night of 08 September is simulated in 1 km height and subsequent downward mixing increases surface dust concentrations. Again, ICON-ART results are one order of magnitude better than those from other models.

What is the synoptic situation enabling this extreme event and how does it relate to its exceptional character?

The event is enabled by an active RST trough situation. This study reveals the existence of a RST with easterly axis over Mesopotamia. It extends far northwards and advects moist and humid air masses from the Persian Gulf region alongside its upstream flank. The RST is connected to an upper tropospheric trough extending far southward, which advects colder air aloft and creates atmospheric instability. The active RST situation thereby enables a period of convectively active days with meso-scale organized convection and associated CPOs. Furthermore, the formation of an intense heat low above Syria is facilitated. The combination of these systems drives dust emissions. The cyclonic flow around the RST provides the basis for the transport of dust towards southern and westerly directions on its downstream flank. It is thereby responsible for the exceptional transport direction of the dust plume into the EM from east. The occurrence of the active RST situation at the beginning of September is unusually early, it thereby explains the extraordinariness of the event with respect to timing.

What are the meteorological drivers responsible for pick-up and long-range transport of mineral dust?

The dust event is created by the interaction of multiple meteorological systems which, in their combination, explain the exceptional magnitude, extent and duration. The meteorological drivers influencing the evolution of the dust plume are organized meso-scale convective systems and their connected CPOs, an intense heat low, the land inward penetrating EM sea-breeze and the widespread occurrence of super-critical flow conditions and subsequent hydraulic jumps.

During the early morning hours of 06 September, a sharply defined CPO (CPO1) from an MCS over the Taurus mountain range interacts with a shallow heat low forming in the boundary layer above Syria. Increased dust emissions occur as soon as turbulent mixing of the boundary layer sets in. Subsequently, the flow and dust plume created interact with the EM sea-breeze penetrating land inwards. Downstream of the upper tropospheric trough and with orographic support from the Zagros mountain range, a second MCS develops over the Turkey-Iraq-Iran border region from noon onwards. The MCS rapidly produces a CPO (CPO2) which travels west in the wake of CPO1 and the heat low, again producing substantial dust emission over central Syria. The lifting caused by the gust front of CPO2 triggers initiation of deep convection over the Syria-Iraq border region which organizes into an MCS around 18 UTC. The MCS is again located in a dynamically favourable position downstream the quasi-stationary upper tropospheric trough. It produces another CPO (CPO3) from 20 UTC onwards. CPO3 subsequently counters and lifts the inflow

from the Persian Gulf along the RST flank, thereby fuelling the MCS and enabling its sustained lifetime of more than 12 hours.

During night-time, the CPO3 gains momentum and spreads towards west. With sunrise and the onset of boundary layer mixing intense dust pick-up occurs in the CPO2 and CPO3 region. During daytime on 07 September, the MCS dissipates. The dust plume connected to CPO3 travels into a south-westerly direction supported by the flow on the downstream flank of the RST. The Dead Sea Rift Valley is passed by the merged dust plumes of CPO2 and CPO3 after midnight on 08 September. During the night, the flow interacts with the complex orography. As a result, widespread super-critical flow conditions, and the subsequent hydraulic jumps, occur in the lee of orographic features. This flow phenomena and the related dust emissions are responsible for extreme dust concentrations in the southern EM on 08 September. During daytime on 08 September, the dust plume is mostly stationary in the EM and influenced by the local circulation systems.

How does the mineral dust radiative effect influence the dust event in general and the evolution of the CPOs in particular?

The mineral dust radiation interaction decreases the amount of solar radiation reaching the surface during daytime and leads to a cooling of the entire dust layer. During night-time, the amount of energy radiated into space from the surface is reduced because of an increase in down-welling atmospheric longwave radiation. A shallow, near surface layer with increased temperatures is apparent in the ICON-ART results. Consequently, the stability of the boundary layer is increased during day-time and decreased during night-time. As a result, dust emissions are systematically lowered during day-time and increased during night-time, a behaviour which is in line with the findings of previous studies.

The newly developed, size dependent parametrization of mineral dust optical properties from Mie calculations shows an effect in dust source regions. It amplifies the above described radiative effects of mineral dust systematically, although with small magnitude. The reduced median diameter of the two largest modes during transport is shown to be responsible for this noticeable effect.

An unexpected and previously undocumented behaviour is found inside the CPO regions. Here, the effect of the mineral dust radiative feedback on temperature is inverted during the early stages of the CPOs development. However, the mineral dust radiative forcing shows the normal night-time effect on radiative fluxes. Nevertheless, surface temperatures are reduced and the dust emissions increase in the radiative feedback run at night. The unexpected behaviour is explained by systematically more intense CPOs and a faster propagation of the CPOs in the mineral dust radiation interaction run. Possible reasons for this behaviour include:

1. More intense convection leading to more rainfall which can evaporate, this in turn cools the CPO more. The intensity of the convection can be increased due to a warmer inflowing airmass because of the mineral dust radiative surface heating at night.

2. More potential for evaporation due to a warmer surface boundary layer, also creating a cooler CPO.
3. A more stable stratified and thereby less turbulent CPO, preventing the loss of energy due to turbulent friction.
4. Travel of the CPO into a less stable night-time boundary layer due to mineral dust radiative surface heating. Therefore, less potential and kinetic energy of the CPO needs to be invested in order to lift the stable night-time boundary layer in front. Due to the reduced resistance propagation speed can increase.

Overall, this study presents a step towards a better understanding and forecast of severe dust events created by the complex interaction of multiple atmospheric drivers. The results emphasize the need for convection-permitting resolutions, when simulating severe dust events triggered by organized meso-scale convection. In addition, new insight is provided on the mineral dust radiative effect and its interaction with convective cold-pool outflows.

In conclusion, it can be stated that through its seamless nesting capabilities ICON-ART offers the possibility to model atmospheric processes at convection permitting resolution with great accuracy. Thereby, ICON-ART can greatly improve our understanding of previously not deciphered events in the atmospheric system. Furthermore, this study highlights the capabilities of ICON-ART with respect to the modelling of dust processes in the atmosphere.

Appendix

Additional figures

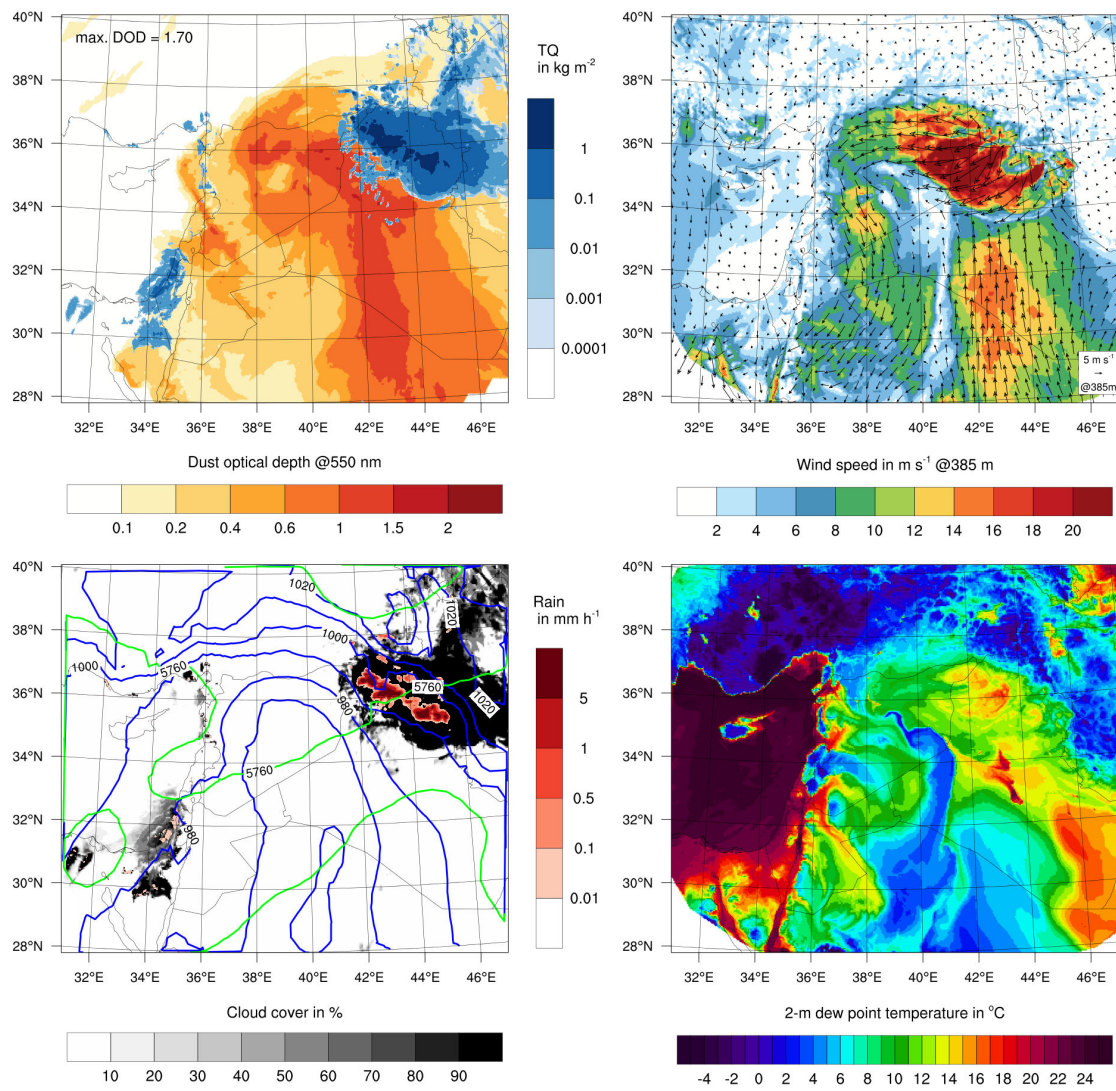


Figure A1: ICON-ART model results for 7th September 03 UTC, same as figure 5.3.

List of acronyms

AERONET	AERosol RObotic NETwork
AOD	Aerosol Optical Depth
ARI	Aerosol Radiation Interaction run
ART	Aerosols and Reactive Trace gases
ASY	ASYmmetry parameter
CALIOP	Cloud-Aerosol LIdar with Orthogonal Polarization
CALIPSO	Cloud-Aerosol Lidar and Infrared Pathfinder Satellite Observation
CCN	Cloud Condensation Nuclei
CMD	Count number distribution Median Diameter
COSMO	COnsortium for SMOll scale MOdelling
CPO	(Convective) Cold-Pool Outflow
CTRL	ConTRoL run
DESERVE	DEad SEa Research VEnue
2m-DPT	2-meter Dew Point Temperature
DOD	Dust Optical Depth
DS	Dead Sea
DWD	Deutscher WetterDienst
ECMWF	European Centre for Medium-Range Weather Forecasts
EM	Eastern Mediterranean
EUMETSAT	European Organisation for the Exploitation of Meteorological Satellites
EXT	EXTinction coefficient
Extpar	External parameter for Numerical Weather Prediction and Climate Application
GADS	Global Aerosol DataSet
HWSD	Harmonized World Soil Database
ICON	ICOsahedral Nonhydrostatic model
IFS	Integrated Forecasting System
IMS	Israeli Meteorological Service
IN	Ice Nuclei
IR	InfraRed part of the spectrum
LT	Local Time
LW	Long-wave
MCS	Meso-scale Convective System
MMD	Mass distribution Median Diameter
MODIS	Moderate Resolution Imaging Spectroradiometer
NLLJ	Nocturnal Low Level Jet
PBL	Planetary Boundary Layer
RF	Radiative Forcing
RRTM	Rapid Radiative Transfer Model
RST	Red Sea Trough
SAMUM	SAharan Mineral dUst experiMent
SEVIRI	Spinning Enhanced Visible and Infrared Imager
SSA	Single Scatter Albedo
SW	Short-wave
TOA	Top Of the Atmosphere
UTC	Coordinated Universal Time
UV	Ultra-Violet part of the spectrum
VIS	VISible part of the spectrum

Bibliography

- Albrecht, 1989: Aerosols, cloud microphysics, and fractional cloudiness. *Science*, **245** (4923), 1227–1230.
- Alfaro, S., S. Lafon, J. Rajot, P. Formenti, A. Gaudichet, and M. Maille, 2004: Iron oxides and light absorption by pure desert dust: An experimental study. *J. Geophys. Res.-Atmos.*, **109** (D8), D08208, 1–9.
- Alfaro, S. C. and L. Gomes, 2001: Modeling mineral aerosol production by wind erosion: Emission intensities and aerosol size distributions in source areas. *J. Geophys. Res.-Atmos.*, **106** (D16), 18 075–18 084.
- Alpert, P., S. Egert, and L. Uzan, 2016: The 7-13 September extreme dust downfall over the East Mediterranean A two ceilometers study. *EGU General Assembly Conference Abstracts*, Vol. 18, 3788.
- Alpert, P., I. Osetinsky, B. Ziv, and H. Shafir, 2004: A new seasons definition based on classified daily synoptic systems: an example for the eastern Mediterranean. *Int. J. Climatol.*, **24** (8), 1013–1021.
- Alpert, P., H. Shafir, and D. Issahary, 1997: Recent changes in the climate at the Dead Sea - a preliminary study. *Climatic Change*, **37** (3), 513–537.
- Arino, O., P. Bicheron, F. Achard, J. Latham, R. Witt, and J.-L. Weber, 2008: The most detailed portrait of Earth. *European Space Agency Bull.*, **136**, 25–31.
- Balkanski, Y., M. Schulz, T. Claquin, and S. Guibert, 2007: Reevaluation of Mineral aerosol radiative forcings suggests a better agreement with satellite and AERONET data. *Atmos. Chem. Phys.*, **7** (1), 81–95.
- Bangert, M., et al., 2012: Saharan dust event impacts on cloud formation and radiation over Western Europe. *Atmos. Chem. Phys.*, **12** (9), 4045–4063, doi:10.5194/acp-12-4045-2012.
- Barahona, D. and A. Nenes, 2009: Parameterizing the competition between homogeneous and heterogeneous freezing in ice cloud formation–polydisperse ice nuclei. *Atmos. Chem. Phys.*, **9** (16), 5933–5948.

- Bitan, A. and H. Sa' Aroni, 1992: The horizontal and vertical extension of the Persian Gulf pressure trough. *Int. J. Climatol.*, **12** (7), 733–747.
- Bohren, C. F. and D. R. Huffman, 1983: *Absorption and scattering of light by small particles*. Repr. 2004 ed., Wiley -VCH, Weinheim, Germany, 529 pp., doi:10.1002/9783527618156.
- Bond, T. C., G. Habib, and R. W. Bergstrom, 2006: Limitations in the enhancement of visible light absorption due to mixing state. *J. Geophys. Res.-Atmos.*, **111** (D20), D20211, 1–13.
- Boucher, O., et al., 2013: Clouds and Aerosols. *The Physical Science Basis. Contribution of Working Group I to the Fifth Assessment Report of the Intergovernmental Panel on Climate Change*, Cambridge University Press, Cambridge, United Kingdom and New York, NY, USA, 571–657.
- Brindley, H., P. Knippertz, C. Ryder, and I. Ashpole, 2012: A critical evaluation of the ability of the Spinning Enhanced Visible and Infrared Imager (SEVIRI) thermal infrared red-green-blue rendering to identify dust events: Theoretical analysis. *J. Geophys. Res.-Atmos.*, **117** (D7), D07201, 1–20.
- Choi, J.-O. and C. E. Chung, 2014: Sensitivity of aerosol direct radiative forcing to aerosol vertical profile. *Tellus*, **66**, 24376, 1–12.
- Clough, S., M. Shephard, E. Mlawer, J. Delamere, M. Iacono, K. Cady-Pereira, S. Boukabara, and P. Brown, 2005: Atmospheric radiative transfer modeling: a summary of the AER codes. *J. Quant. Spectrosc. Radiat. Transfer*, **91** (2), 233–244.
- Cuesta, J., J. H. Marsham, D. J. Parker, and C. Flamant, 2009: Dynamical mechanisms controlling the vertical redistribution of dust and the thermodynamic structure of the West Saharan atmospheric boundary layer during summer. *Atmos. Sci. Lett.*, **10** (1), 34–42.
- Cziczo, D. J., et al., 2013: Clarifying the dominant sources and mechanisms of cirrus cloud formation. *Science*, **340** (6138), 1320–1324.
- Darmenova, K. and I. N. Sokolik, 2007: Assessing uncertainties in dust emission in the Aral Sea region caused by meteorological fields predicted with a mesoscale model. *Global Planet. Change*, **56** (3), 297–310.
- Dayan, U., B. Ziv, T. Shoob, and Y. Enzel, 2008: Suspended dust over southeastern Mediterranean and its relation to atmospheric circulations. *Int. J. Climatol.*, **28** (7), 915–924.
- Dipankar, A., B. Stevens, R. Heinze, C. Moseley, G. Zängl, M. Giorgetta, and S. Brdar, 2015: Large eddy simulation using the general circulation model ICON. *J. Adv. Model. Earth Syst.*, **7** (3), 963–986.
- Drobinski, P., S. Bastin, S. Janicot, O. Bock, A. Dabas, P. Delville, O. Reitebuch, and B. Sultan, 2009: On the late northward propagation of the West African monsoon in summer 2006 in the region of Niger/Mali. *J. Geophys. Res.-Atmos.*, **114** (D9), D09108, 1–16.

- Drobinski, P., C. Flamant, J. Dusek, P. H. Flamant, and J. Pelon, 2001: Observational Evidence And Modelling Of An Internal Hydraulic Jump At The Atmospheric Boundary-Layer Top During A Tramontane Event. *Boundary Layer Meteorol.*, **3 (98)**, 497–515.
- Dubovik, O., B. Holben, T. F. Eck, A. Smirnov, Y. J. Kaufman, M. D. King, D. Tanré, and I. Slutsker, 2002: Variability of absorption and optical properties of key aerosol types observed in worldwide locations. *J. Atmos. Sci.*, **59 (3)**, 590–608.
- Dubovik, O., A. Smirnov, B. Holben, M. King, Y. Kaufman, T. Eck, and I. Slutsker, 2000: Accuracy assessments of aerosol optical properties retrieved from Aerosol Robotic Network (AERONET) Sun and sky radiance measurements. *J. Geophys. Res.-Atmos.*, **105 (D8)**, 9791–9806.
- Dunion, J. P. and C. S. Velden, 2004: The impact of the Saharan air layer on Atlantic tropical cyclone activity. *Bull. Amer. Meteor. Soc.*, **85 (3)**, 353–365.
- Evan, A. T., J. Dunion, J. A. Foley, A. K. Heidinger, and C. S. Velden, 2006: New evidence for a relationship between Atlantic tropical cyclone activity and African dust outbreaks. *Geophys. Res. Lett.*, **33 (19)**, L19813, 1–5.
- Fécan, F., B. Marticorena, and G. Bergametti, 1999: Parametrization of the increase of the aeolian erosion threshold wind friction velocity due to soil moisture for arid and semi-arid areas. *Ann. Geophys.*, **17 (1)**, 149–157, doi:10.1007/s00585-999-0149-7.
- Forster, P., et al., 2007: Changes in atmospheric constituents and in radiative forcing. *Climate Change 2007. The Physical Science Basis. Contribution of Working Group I to the Fourth Assessment Report of the Intergovernmental Panel on Climate Change*, Cambridge University Press, Cambridge, United Kingdom and New York, NY, USA, chap. 2.
- Fouquart, Y., B. Bonnel, G. Brogniez, J. Buriez, L. Smith, J. Morcrette, and A. Cerf, 1987: Observations of Saharan aerosols: Results of ECLATS field experiment. Part II: Broadband radiative characteristics of the aerosols and vertical radiative flux divergence. *Journal of Applied Meteorology and Climatology*, **26 (1)**, 38–52.
- Ganor, E., 1991: The composition of clay minerals transported to Israel as indicators of Saharan dust emission. *Atmospheric Environment. Part A. General Topics*, **25 (12)**, 2657–2664.
- Gavrieli, I., A. Bein, and A. Oren, 2005: The expected impact of the peace conduit project (the Red Sea–Dead Sea pipeline) on the Dead Sea. *Mitigation and Adaptation Strategies for Global Change*, **10 (1)**, 3–22.
- Gavrieli, I. and A. Oren, 2004: The Dead Sea as a dying lake. *Dying and Dead Seas Climatic Versus Anthropic Causes*, J. C. J. Nihoul, P. O. Zavialov, and P. P. Micklin, Eds., Springer, Dordrecht, 287–305.

- Gertman, I. and A. Hecht, 2002: The Dead Sea hydrography from 1992 to 2000. *J. Mar. Syst.*, **35** (3), 169–181.
- Ginoux, P., J. M. Prospero, T. E. Gill, N. C. Hsu, and M. Zhao, 2012: Global-scale attribution of anthropogenic and natural dust sources and their emission rates based on MODIS Deep Blue aerosol products. *Rev. Geophys.*, **50** (3), RG3005, 1–36.
- Goudie, A. S., 2014: Desert dust and human health disorders. *Environ. Int.*, **63**, 101–113.
- Heinold, B., P. Knippertz, J. Marsham, S. Fiedler, N. Dixon, K. Schepanski, B. Laurent, and I. Tegen, 2013: The role of deep convection and nocturnal low-level jets for dust emission in summertime West Africa: Estimates from convection-permitting simulations. *J. Geophys. Res.-Atmos.*, **118** (10), 4385–4400.
- Heinold, B., I. Tegen, K. Schepanski, and O. Hellmuth, 2008: Dust radiative feedback on Saharan boundary layer dynamics and dust mobilization. *Geophys. Res. Lett.*, **35** (20), L20817, 1–5.
- Heintzenberg, J., 2009: The SAMUM-1 experiment over southern Morocco: Overview and introduction. *Tellus B*, **61** (1), 2–11.
- Helmert, J., B. Heinold, I. Tegen, O. Hellmuth, and M. Wendisch, 2007: On the direct and semidirect effects of Saharan dust over Europe: A modeling study. *J. Geophys. Res.-Atmos.*, **112** (D13), D13208, 1–24.
- Highwood, E. J. and C. L. Ryder, 2014: Dust Production Mechanisms. *Mineral Dust*, P. Knippertz and J.-B. W. Stuut, Eds., Springer, Dordrecht, Netherlands, chap. 11, 267–286.
- Holben, B. N., et al., 1998: AERONET - A federated instrument network and data archive for aerosol characterization. *Remote Sens. Environ.*, **66** (1), 1–16.
- Hoose, C. and O. Möhler, 2012: Heterogeneous ice nucleation on atmospheric aerosols: a review of results from laboratory experiments. *Atmos. Chem. Phys.*, **12** (20), 9817–9854.
- Hsu, N. C., S.-C. Tsay, M. D. King, and J. R. Herman, 2004: Aerosol properties over bright-reflecting source regions. *IEEE Trans. Geosci. Remote Sens.*, **42** (3), 557–569.
- Huneus, N., et al., 2011: Global dust model intercomparison in AeroCom phase I. *Atmos. Chem. Phys.*, **11** (15), 7781–7816.
- Ilotoviz, E., H. Shafir, P. Gasch, and P. Alpert, 2015: Semi Operational Prediction of the Dead Sea Evaporation - A Synoptic Systems Approach. *J. Water Resour. Prot.*, **7** (13), 1058–1074.
- Kahnert, M., T. Nousiainen, and P. Räisänen, 2007: Mie simulations as an error source in mineral aerosol radiative forcing calculations. *Quart. J. Roy. Meteor. Soc.*, **133** (623), 299–307.
- Kalenderski, S. and G. Stenchikov, 2016: High-resolution regional modeling of summertime transport and impact of African dust over the Red Sea and Arabian Peninsula. *J. Geophys. Res.-Atmos.*, **121** (11), 6435 – 6458.

- Kerkmann, J., S. Lancaster, and H. P. Roesli, 2015: Many parts of the Middle East were shrouded in a persistent dust cloud in early September. URL http://www.eumetsat.int/website/home/Images/ImageLibrary/DAT_2773503.html, last accessed 08 Aug 2016.
- Kishcha, P., et al., 2016: Modelling of a strong dust event in the complex terrain of the Dead Sea valley during the passage of a gust front. *Tellus B*, **68**, 29751, 1–19.
- Knippertz, P., 2014: Meteorological aspects of dust storms. *Mineral Dust*, P. Knippertz and J.-B. W. Stuut, Eds., Springer, Dordrecht, Netherlands, chap. 6, 121–147.
- Knippertz, P., C. Deutscher, K. Kandler, T. Müller, O. Schulz, and L. Schütz, 2007: Dust mobilization due to density currents in the Atlas region: Observations from the Saharan Mineral Dust Experiment 2006 field campaign. *J. Geophys. Res.-Atmos.*, **112 (D21)**, D21109, 1–14.
- Knippertz, P. and J.-B. W. Stuut, 2014: *Mineral Dust: A Key Player in the Earth System*. Springer, Dordrecht, Netherlands, 509 pp., doi:10.1007/978-94-017-8978-3.
- Knippertz, P., et al., 2009: Dust mobilization and transport in the northern Sahara during SAMUM 2006—a meteorological overview. *Tellus B*, **61 (1)**, 12–31.
- Kok, J. F., 2011: Does the size distribution of mineral dust aerosols depend on the wind speed at emission? *Atmos. Chem. Phys.*, **11 (19)**, 10 149–10 156.
- Köpke, P., M. Hess, I. Schult, and E. Shettle, 1997: Global aerosol data set. Tech. rep., Max-Planck-Institut für Meteorologie, Hamburg. 44 pp.
- Kottmeier, C., et al., 2016: New perspectives on interdisciplinary earth science at the Dead Sea: The DESERVE project. *Sci. Total Environ.*, **544**, 1045–1058.
- Krichak, S. O., J. S. Breitgand, and S. B. Feldstein, 2012: A conceptual model for the identification of active Red Sea trough synoptic events over the southeastern Mediterranean. *Journal of Applied Meteorology and Climatology*, **51 (5)**, 962–971.
- Lenky, I. and D. Rosenfeld, 2008: Clouds-aerosols-precipitation satellite analysis tool (CAPSAT). *Atmos. Chem. Phys.*, **8 (22)**, 6739–6753.
- Levy, R. and C. Hsu, 2015: MODIS Atmosphere L2 Aerosol Product. Tech. rep., NASA, Goddard Space Flight Center, USA. doi:10.5067/MODIS/MOD04_L2.006.
- Linke, C., O. Möhler, A. Veres, A. Mohacsi, Z. Bozóki, G. Szabó, and M. Schnaiter, 2006: Optical properties and mineralogical composition of different Saharan mineral dust samples: a laboratory study. *Atmos. Chem. Phys. Discuss.*, **6 (2)**, 2897–2922.
- Lundgren, K., 2011: Direct radiative effects of sea salt on the regional scale. Wissenschaftliche Berichte des Instituts für Meteorologie und Klimaforschung des Karlsruher Instituts für Technologie; Band 53, Karlsruhe Institute of Technology, 242 pp., Karlsruhe, doi: 10.5445/KSP/1000024937.

- Mamouri, R.-E., A. Nisantzi, A. Ansmann, and D. G. Hadjimitsis, 2016: Extreme dust storm over the eastern Mediterranean in September 2015: Lidar vertical profiling of desert dust at Limassol, Cyprus. *Atmos. Chem. Phys. Discuss.*, **2016**, 1–12, doi:10.5194/acp-2016-354.
- Marshall, J. H., P. Knippertz, N. S. Dixon, D. J. Parker, and G. Lister, 2011: The importance of the representation of deep convection for modeled dust-generating winds over West Africa during summer. *Geophys. Res. Lett.*, **38** (16), L16803, 1–6.
- Martcorena, B., 2014: Dust Production Mechanisms. *Mineral Dust*, P. Knippertz and J.-B. W. Stuut, Eds., Springer, Dordrecht, Netherlands, chap. 6, 93–120.
- Martínez-García, A., A. Rosell-Melé, S. L. Jaccard, W. Geibert, D. M. Sigman, and G. H. Haug, 2011: Southern Ocean dust-climate coupling over the past four million years. *Nature*, **476** (7360), 312–315.
- Mätzler, C., 2002: MATLAB functions for Mie scattering and absorption, version 2. Tech. rep., Institute of Applied Physics, University of Bern. 1–26.
- McConnell, C., P. Formenti, E. Highwood, and M. Harrison, 2010: Using aircraft measurements to determine the refractive index of Saharan dust during the DODO Experiments. *Atmos. Chem. Phys.*, **10** (6), 3081–3098.
- Metzger, J., 2016: Wind Systems and Energy Balance in the Dead Sea Valley. Ph.D. thesis, Karlsruhe Institute of Technology, Karlsruhe, in preparation.
- Mie, G., 1908: Beiträge zur Optik trüber Medien, speziell kolloidaler Metallösungen. *Ann. Phys.*, **330** (3), 377–445.
- Miller, S. D., A. P. Kuciauskas, M. Liu, Q. Ji, J. S. Reid, D. W. Breed, A. L. Walker, and A. A. Mandoos, 2008: Haboob dust storms of the southern Arabian Peninsula. *J. Geophys. Res.-Atmos.*, **113** (D1), D01202, 1–26.
- Mishchenko, M., A. Lacis, B. Carlson, and L. Travis, 1995: Nonsphericity of dust-like tropospheric aerosols: Implications for aerosol remote sensing and climate modeling. *Geophys. Res. Lett.*, **22** (9), 1077–1080.
- Mishchenko, M. I., L. D. Travis, R. A. Kahn, and R. A. West, 1997: Modeling phase functions for dustlike tropospheric aerosols using a shape mixture of randomly oriented polydisperse spheroids. *J. Geophys. Res.-Atmos.*, **102** (D14), 16 831–16 847.
- Mlawer, E. J., S. J. Taubman, P. D. Brown, M. J. Iacono, and S. A. Clough, 1997: Radiative transfer for inhomogeneous atmospheres: RRTM, a validated correlated-k model for the longwave. *J. Geophys. Res.-Atmos.*, **102** (D14), 16 663–16 682.
- Morcrette, J., H. Barker, J. Cole, M. Iacono, and R. Pincus, 2008: Impact of a new radiation package, McRad, in the ECMWF integrated forecasting system. *Mon. Weather Rev.*, **136** (12), 4773–4798.

- Myhre, G. and F. Stordal, 2001: Global sensitivity experiments of the radiative forcing due to mineral aerosols. *J. Geophys. Res.-Atmos.*, **106 (D16)**, 18 193–18 204.
- Nachtergaele, F. and N. Batjes, 2012: Harmonized world soil database. Rome, 1–35, Food and Agriculture Organization of the United Nations, Rome, 1–35.
- NASA Earth Observatory, 2015: Dust Storm Sweeps Across Middle East. URL <http://earthobservatory.nasa.gov/NaturalHazards/view.php?id=86571>, last accessed 25 Aug 2016.
- NASA Worldview, 2016: URL <https://worldview.earthdata.nasa.gov/>, last accessed 08 Aug 2016.
- O’Neill, N., T. Eck, A. Smirnov, B. Holben, and S. Thulasiraman, 2003: Spectral discrimination of coarse and fine mode optical depth. *J. Geophys. Res.-Atmos.*, **108 (D17)**, 4559, 1–15.
- Osetinsky, I., 2006: Climate changes over the E. Mediterranean - A synoptic systems classification approach. Ph.D. thesis, Tel Aviv University, 153 pp., Tel Aviv.
- Otto, S., et al., 2009: Solar radiative effects of a Saharan dust plume observed during SAMUM assuming spheroidal model particles. *Tellus B*, **61 (1)**, 270–296.
- Pantillon, F., P. Knippertz, J. H. Marsham, and C. E. Birch, 2015: A parameterization of convective dust storms for models with mass-flux convection schemes. *J. Atmos. Sci.*, **72 (6)**, 2545–2561.
- Pantillon, F., P. Knippertz, J. H. Marsham, H.-J. Panitz, and I. Bischoff-Gauss, 2016: Modeling haboob dust storms in large-scale weather and climate models. *J. Geophys. Res.-Atmos.*, **121**, 2090–2109.
- Pérez, C., S. Nickovic, G. Pejanovic, J. M. Baldasano, and E. Özsoy, 2006: Interactive dust-radiation modeling: A step to improve weather forecasts. *J. Geophys. Res.-Atmos.*, **111 (D16)**, D16206, 1–17.
- Petty, G. W., 2006: *A first course in atmospheric radiation*. Sundog Pub, Madison, USA, 452 pp.
- Petzold, A., et al., 2009: Saharan dust absorption and refractive index from aircraft-based observations during SAMUM 2006. *Tellus B*, **61 (1)**, 118–130.
- Phillips, V. T., P. J. Demott, C. Andronache, K. A. Pratt, K. A. Prather, R. Subramanian, and C. Twohy, 2013: Improvements to an empirical parameterization of heterogeneous ice nucleation and its comparison with observations. *J. Atmos. Sci.*, **70 (2)**, 378–409.
- Pope III, C. A., R. T. Burnett, M. J. Thun, E. E. Calle, D. Krewski, K. Ito, and G. D. Thurston, 2002: Lung cancer, cardiopulmonary mortality, and long-term exposure to fine particulate air pollution. *JAMA*, **287 (9)**, 1132–1141.
- Raschendorfer, M., 2001: The new turbulence parameterization of LM. *COSMO newsletter*, **1**, 89–97.

- Raupach, M. et al., 1993: Dry deposition of gases and particles to vegetation. *Clean Air: Journal of the Clean Air Society of Australia and New Zealand*, **27** (4), 200–203.
- Redl, R., P. Knippertz, and A. H. Fink, 2016: Weakening and moistening of the summertime Saharan heat low through convective cold pools from the Atlas Mountains. *J. Geophys. Res.-Atmos.*, **121** (8), 3907–3928.
- Rémy, S., et al., 2015: Feedbacks of dust and boundary layer meteorology during a dust storm in the eastern Mediterranean. *Atmos. Chem. Phys.*, **15** (22), 12 909–12 933.
- Rieger, D., 2016: Der Einfluss von natürlichem Aerosol auf Wolken. Ph.D. thesis, Karlsruhe Institute of Technology, Karlsruhe, in preparation.
- Rieger, D., et al., 2015: ICON–ART 1.0—a new online-coupled model system from the global to regional scale. *Geosci. Model Dev.*, **8** (6), 1659–1676.
- Seifert, A. and K. Beheng, 2006: A two-moment cloud microphysics parameterization for mixed-phase clouds. Part 1: Model description. *Meteorol. Atmos. Phys.*, **92** (1-2), 45–66.
- Seifert, A. and K. D. Beheng, 2001: A double-moment parameterization for simulating autoconversion, accretion and selfcollection. *Atmos. Res.*, **59**, 265–281.
- Shafir, H. and P. Alpert, 2011: Regional and local climatic effects on the Dead-Sea evaporation. *Climatic Change*, **105** (3-4), 455–468.
- Shao, Y., A. H. Fink, and M. Klose, 2010: Numerical simulation of a continental-scale Saharan dust event. *J. Geophys. Res.-Atmos.*, **115** (D13), D13205, 1–19.
- Shao, Y., M. Ishizuka, M. Mikami, and J. Leys, 2011b: Parameterization of size-resolved dust emission and validation with measurements. *J. Geophys. Res.-Atmos.*, **116** (D8), D08203, 1–19.
- Shao, Y. and H. Lu, 2000: A simple expression for wind erosion threshold friction velocity. *J. Geophys. Res.-Atmos.*, **105** (D17), 22 437–22 443.
- Shao, Y., et al., 2011a: Dust cycle: An emerging core theme in Earth system science. *Aeolian Res.*, **2** (4), 181–204, doi:<http://dx.doi.org/10.1016/j.aeolia.2011.02.001>.
- Shettle, E. P. and R. W. Fenn, 1979: Models for the aerosols of the lower atmosphere and the effects of humidity variations on their optical properties. Tech. rep., Air Force Geophysics Laboratory. 1–94.
- Singer, A., S. Dultz, and E. Argaman, 2004: Properties of the non-soluble fractions of suspended dust over the Dead Sea. *Atmos. Environ.*, **38** (12), 1745–1753.
- Singer, A., E. Ganor, S. Dultz, and W. Fischer, 2003: Dust deposition over the Dead Sea. *J. Arid. Environ.*, **53** (1), 41–59.

- Sinyuk, A., O. Torres, and O. Dubovik, 2003: Combined use of satellite and surface observations to infer the imaginary part of refractive index of Saharan dust. *Geophys. Res. Lett.*, **30** (2), 1081, 1–4.
- Sokolik, I. N. and O. B. Toon, 1999: Incorporation of mineralogical composition into models of the radiative properties of mineral aerosol from UV to IR wavelengths. *J. Geophys. Res.-Atmos.*, **104** (D8), 9423–9444.
- Spyrou, C., G. Kallos, C. Mitsakou, P. Athanasiadis, C. Kalogeri, and M. Iacono, 2013: Modeling the radiative effects of desert dust on weather and regional climate. *Atmos. Chem. Phys.*, **13** (11), 5489–5504.
- Stanelle, T., 2008: Wechselwirkungen von Mineralstaubpartikeln mit thermodynamischen und dynamischen Prozessen in der Atmosphäre über Westafrika. Wissenschaftliche Berichte des Instituts für Meteorologie und Klimaforschung des Karlsruher Instituts für Technologie; Band 48, Karlsruhe Institute of Technology, 157 pp., Karlsruhe.
- Stanelle, T., B. Vogel, H. Vogel, D. Bäumer, and C. Kottmeier, 2010: Feedback between dust particles and atmospheric processes over West Africa during dust episodes in March 2006 and June 2007. *Atmos. Chem. Phys.*, **10** (22), 10771–10788.
- Stanhill, G., 1994: Changes in the rate of evaporation from the Dead Sea. *Int. J. Climatol.*, **14** (4), 465–471.
- Steinhorn, I., et al., 1979: The Dead Sea: deepening of the mixolimnion signifies the overture to overturn of the water column. *Science*, **206** (4414), 55–57.
- Tegen, I., B. Heinold, M. Todd, J. Helmert, R. Washington, and O. Dubovik, 2006: Modelling soil dust aerosol in the Bodélé depression during the BoDEx campaign. *Atmos. Chem. Phys.*, **6** (12), 4345–4359.
- Tegen, I. and A. A. Lacis, 1996: Modeling of particle size distribution and its influence on the radiative properties of mineral dust aerosol. *J. Geophys. Res.-Atmos.*, **101** (D14), 19237–19244.
- The Weather Channel, 2015: Intense Middle East Dust Storm Kills At Least 5, Sickens Hundreds. URL <https://weather.com/news/news/severe-middle-east-sandstorm-dust-storm-jordan-israel-lebanon-syria-iraq>, last accessed 08 Aug 2016.
- Times Of Israel, 2015: Heavy dust blankets country for second day as intense heat joins in. URL <http://www.timesofisrael.com/heavy-dust-to-blanket-country-for-second-day-as-intense-heat-joins-in/>, last accessed 25 Aug 2016.
- Tsvieli, Y. and A. Zangvil, 2005: Synoptic climatological analysis of wet and dry Red Sea troughs over Israel. *Int. J. Climatol.*, **25** (15), 1997–2015.
- Twomey, S., 1974: Pollution and the planetary albedo. *Atmos. Environ.*, **8** (12), 1251–1256.

- Vogel, B., C. Hoose, H. Vogel, and C. Kottmeier, 2006: A model of dust transport applied to the Dead Sea area. *Meteorol. Z.*, **15** (6), 611–624.
- Volz, F. E., 1972: Infrared refractive index of atmospheric aerosol substances. *Appl. Opt.*, **11** (4), 755–759.
- Volz, F. E., 1973: Infrared optical constants of ammonium sulfate, Sahara dust, volcanic pumice, and flyash. *Appl. Opt.*, **12** (3), 564–568.
- Vries, A., E. Tyrlis, D. Edry, S. Krichak, B. Steil, and J. Lelieveld, 2013: Extreme precipitation events in the Middle East: dynamics of the Active Red Sea Trough. *J. Geophys. Res.-Atmos.*, **118** (13), 7087–7108.
- Washington, R., M. C. Todd, S. Engelstaedter, S. Mbainayel, and F. Mitchell, 2006: Dust and the low-level circulation over the Bodélé Depression, Chad: Observations from BoDEx 2005. *J. Geophys. Res.-Atmos.*, **111** (D3), D0320, 1–15.
- White, B. R., 1979: Soil transport by winds on Mars. *J. Geophys. Res. Solid Earth*, **84** (B9), 4643–4651.
- Winker, D. M., W. H. Hunt, and M. J. McGill, 2007: Initial performance assessment of CALIOP. *Geophys. Res. Lett.*, **34** (19), doi:10.1029/2007GL030135, L19803, 1–5.
- Yu, H., et al., 2015: The fertilizing role of African dust in the Amazon rainforest: A first multiyear assessment based on data from Cloud-Aerosol Lidar and Infrared Pathfinder Satellite Observations. *Geophys. Res. Lett.*, **42** (6), 1984–1991.
- Zängl, G., D. Reinert, P. Rípodas, and M. Baldauf, 2015: The ICON (ICOsahedral Non-hydrostatic) modelling framework of DWD and MPI-M: Description of the non-hydrostatic dynamical core. *Quart. J. Roy. Meteor. Soc.*, **141** (687), 563–579.
- Zhu, Y. and R. E. Newell, 1998: A proposed algorithm for moisture fluxes from atmospheric rivers. *Mon. Weather Rev.*, **126** (3), 725–735.

Acknowledgements

Scientific acknowledgements

Firstly I am indebted to Yoav Levi and Pavel Khain from the IMS for the provision of an extensive dataset of all meteorological measurements in Israel with superb formatting and English descriptions.

Furthermore I would like to thank Tami Bond and Christoph Maetzler for making their MatLab based Mie-code publicly available.

Jochen Kerkman, Hans-Peter Roesli and Sancha Lancaster are gratefully acknowledged for granting me the right to use their EUMETSAT animations of the dust event.

I thank Arnon Karnieli for his effort in establishing and maintaining the Sede Boker AERONET site.

The MODIS Aerosol Optical Depth datasets were acquired from the Level-1 Atmosphere Archive and Distribution System (LAADS) Distributed Active Archive Center (DAAC), located in the Goddard Space Flight Center in Greenbelt, Maryland (<https://ladsweb.nascom.nasa.gov/>)

Persönliche Danksagung

Ich möchte mich bei Prof. Dr. Christoph Kottmeier für die Übernahme des Referates sowie die Ermöglichung zahlreicher interessanter Tätigkeiten am Institut bedanken. Ebenso gilt mein Dank Prof. Dr. Peter Knippertz für die Übernahme des Korreferats und die detaillierten Anmerkungen zur Verbesserung der Arbeit. Dr. Bernhard Vogel danke ich für die Aufnahme in seine Arbeitsgruppe und Betreuung der Arbeit, die Möglichkeit mich mit ICON-ART zu beschäftigen und die stets hilfreichen Rückmeldungen zu meiner Arbeit.

Mein besonderer Dank gilt Daniel Rieger, der viele Stunden in das Gelingen dieser Arbeit investiert hat. Es war extrem hilfreich, dass ich nahezu täglich und mit all meinen Fragen vorbeischaun konnte und immer eine ausführliche Antwort erhalten habe. Ebenso bedanke ich mich bei Carolin Walter, die oft genug mit zuhören musste und ebenfalls viele wertvolle Anmerkungen gemacht hat. Beiden zusammen gilt außerdem mein Dank für die intensive Zusammenarbeit bei der Implementierung der Aerosol-Strahlungswechselwirkung in ICON-ART.

Zusätzlich möchte ich mich bei der Arbeitsgruppe Vogel für die gute Arbeitsatmosphäre bedanken. Besonders zu erwähnen sind Dr. Heike Vogel für die Bereitstellung der IFS-Daten und Sven Werchner für die Hilfe bei der XML-Implementierung der optischen Eigenschaften.

Jutta Metzger danke ich für die Bereitstellung der Energiebilanzdaten, auch wenn diese schlussendlich doch nicht in diese Arbeit eingeflossen sind. Bei Dr. Ulrich Corsmeier möchte ich mich für den Gaststatus in seiner Arbeitsgruppe und das stets in mich gesetzte Vertrauen bedanken. *Furthermore I am thankful to the whole DESERVE-Team who have provided me with valuable insight and the opportunity of many visits in the region.*

Daniel Rieger und Manuela Nied danke ich zusätzlich für das ausführliche Korrekturlesen meiner Arbeit.

Mein herzlichster Dank gilt allen, die direkt oder indirekt zu dieser Arbeit beigetragen haben und hier noch nicht namentlich erwähnt wurden. Dazu zählen insbesondere meine Familie, Freunde hier *and abroad* und Mitbewohnerinnen. Danke, dass ihr stets für mich da seid.

Erklärung

Hiermit erkläre ich, dass ich die vorliegende Arbeit selbst verfasst und nur die angegebenen Hilfsmittel verwendet habe.

Ich bin damit einverstanden, dass diese Arbeit in Bibliotheken eingestellt wird und vervielfältigt werden darf.

Karlsruhe, den 8. September 2016

Philipp Gasch